NASA Technical Memorandum 84226

NASA-TM-84226

19820019346

Three-Dimensional Flows About Simple Components at Angle of Attack

David J. Peake and Murray Tobak

March 1982

NASA
National Aeronautics and
Space Administration

NASA Technical Memorandum 84226

Three-Dimensional Flows About Simple Components at Angle of Attack

David J. Peake
Murray Tobak, Ames Research Center, Moffett Field, California

National Aeronautics and
Space Administration

Ames Research Center
Moffett Field, California 94035

THREE-DIMENSIONAL FLOWS ABOUT SIMPLE COMPONENTS AT ANGLE OF ATTACK

David J. Peake and Murray Tobak
Ames Research Center, Moffett Field, California 94035

SUMMARY

The structures of three-dimensional separated flows about some chosen aerodynamic components at angle of attack are synthesized, holding strictly to the notion that streamlines in the external flow (viscous plus inviscid) and skin-friction lines on the body surface may be considered as trajectories having properties consistent with those of continuous vector fields. Singular points in the fields are of limited number and are classified as simple nodes and saddles. Analogous flow structures at high angles of attack about blunt and pointed bodies, straight and swept wings, etc., are discussed, highlighting the formation of spiral nodes (foci) in the pattern of the skin-friction lines. How local and global three-dimensional separation lines originate and form is addressed, and the characteristics of both symmetric and asymmetric leeward wakes are described.

1. INTRODUCTION

Invoking our previously introduced notions (Ref. 1) of topological structure, structural stability, and local and global lines of separation, we shall attempt to demonstrate how these assist us in deducing the complex patterns of skin-friction lines and external-flow streamlines about simple aerodynamic components at angle of attack. The components may be considered typical of those used in aeronautical applications. They include blunt and pointed bodies, and straight, swept, and slender wings. Initially, however, we shall take the case of a simple hemisphere-cylinder, immersed in a Mach 1.2 free stream at constant Reynolds number ($R_{L_\infty} = 4.9 \times 10^6$), and increase the angle of attack α in stages in the range $0° < \alpha < 32.5°$. We shall see that the types of singular points with their accompanying characteristic developments of local and global separation zones, and the progressive changes in the patterns as the angle of attack increases, will form a useful foundation for understanding the flow fields about the other flow components discussed in subsequent sections.

2. HEMISPHERE-CYLINDER

Oil-flow patterns indicative of the development of the skin-friction lines on the hemisphere-cylinder are illustrated in Figs. 1a to 1i as angle of attack is increased progressively from axisymmetric conditions ($\alpha = 0°$) to $\alpha = 32.5°$. Figure 2 portrays the conceptual patterns of singular points associated with the skin-friction lines (and streamline projections in some chosen crossflow planes) that have been synthesized from the oil-flow patterns in Fig. 1 and laser vapor-screen crossflow visualization shown in Figs. 3 and 4. To assist the reader, Fig. 3 shows the experimental setup of the expanded laser beam (see Ref. 2) that cuts the body at $x/D = 6.5$ perpendicular to its axis. Flow is from right to left, so that the photographs in both Figs. 3 and 4 display views looking toward the back of the body on the starboard side.

Figures 1a and 2a portray the axisymmetric skin-friction line pattern about the hemisphere-cylinder at $M_\infty = 1.2$. All skin-friction lines originate at the nodal singular point of attachment at the nose (the stagnation point) and stop at a singular line of separation around the body just downstream of the junction between the hemisphere and the cylinder. The stream surface departing from the separation line reattaches at the singular line of attachment situated a short distance farther downstream, to form a closed separation bubble. A parallel pattern of skin-friction lines emerges from the reattachment line in both the upstream and downstream directions. Under the present experimental conditions, the wedges in the oil-flow pattern on the cylinder (see Fig. 1a) indicate that the axisymmetric separation and reattachment are laminar, with transition to turbulence occurring downstream shortly thereafter. The downstream-directed skin-friction lines, for a sufficiently smooth and slender afterbody, will disappear into a nodal point of separation at the tail, satisfying the relevant topological rule for a closed-body surface that the sum of the nodes on the surface must always exceed the number of saddle points by two. Here, of course, we have only the nodes of attachment and separation and no saddle points. Figure 3 illustrates the axisymmetric boundary-layer growth in the vapor screen at $x/D = 6.5$, with the bounding shock wave surrounding the body cross section.

When the angle of attack is increased to a small value, say 1°, we expect to find the pattern of skin-friction lines drawn conceptually in Fig. 2b. The slightest departure from axisymmetry causes the skin-friction line pattern to pass through a structural instability: the axisymmetric singular separation and reattachment lines disappear and are replaced by saddle and nodal points of attachment on the windward ray, and nodal and saddle points of separation on the leeward ray. There is a characteristic dividing surface in the flow that is anchored on the leeward ray and that emanates from the nodal point of separation, N_S. We note that streamlines on this dividing surface in the meridian plane have all entered the fluid through the saddle point of separation, S_1, in the pattern of skin-friction lines along the leeward ray. At this small angle of attack, the dividing surface will grow very slowly with progression downstream as the adjacent boundary layers converge very slowly toward the leeward ray. The existence of this dividing surface stemming from a combination of nodal and saddle points of separation on the leeward ray will be clearly evident as a dark line in the leeward meridian plane in the vapor-screen photographs at elevated angles of attack. In fact, it is through our description of the dividing surface that we are able to explain the presence of this obvious feature of the vapor-screen photographs (see Fig. 4).

When the angle of attack is increased to 3.5° (Figs. 1b and 2c) the pattern of skin-friction lines undergoes another structural change. The lines of separation emanating from the saddle point on the windward ray terminate in spiral nodes just short of the leeward ray. The simultaneous appearance of a pair of saddle points on either side of the nodal point of separation on the leeward ray maintains the differential between nodes and saddles required by the topological rule. Figure 5b of the previous lecture illustrates the form of the dividing surfaces that typically emanate into the external flow from this combination of surface-flow topology.

Increasing the angle of attack to 5° (Figs. 1c and 2d) provides us with a topology at the front of the body that is similar to that at 3.5°, but toward the end of the body the skin-friction lines, all emanating from the nodal point of attachment on the windward ray, show indications of converging toward primary separation zones that will produce primary vortices. The enhanced thickening of the viscous flow along the leeward is shown in Fig. 4a. At 6.5° (Fig. 1d), we have, in addition, certain evidence of the phenomenon of instability in the crossflow velocity profiles just downstream of the hemispherical cap. There are fine striations in the oil-flow pattern superimposed over the regular pattern of skin-friction lines, lending credence to the proposal that the laminar boundary layer has undergone a supercritical bifurcation (such as that described in the previous lecture), resulting in the appearance of an array of small-scale vortices within the boundary layer.

Continuing to increase the angle of attack toward 10° (Figs. 1e, 2e, 4b) causes the singular points on the windward ray to come together and to eventually disappear. Meanwhile, additional singular points appear on the leeward. At the precise angle(s) of attack at which the singular points disappear and appear, we pass through new structural instabilities in the skin-friction line pattern. We also detect another particular line in the skin-friction line pattern, situated between the primary separation line and the leeward ray, toward which adjacent boundary-layer material is also converging — the so-called secondary separation line. The stream surface from this line coils up as a secondary vortex that is of opposite rotation to and is tucked beneath the primary vortex. Now with the disappearance of the windward saddle and nodal points of attachment, the entire pattern of skin-friction lines on the body surface all stem from the nodal point of attachment at the nose. Thus, referring to Fig. 2e, in our classification according to the mathematical notions of topological structure and structural stability, the primary separation lines are local ones and the secondary separation lines stemming from the leeward saddle points, S_4 and S_5, are global separations. Note now, however, that the eruptions from the spiral nodes will key the roll-up of the secondary vortices, so that the single dividing surface growing from the leeward ray appears as a thin shadow with no evidence of the "mushroom" or "T-shape" that we proposed at $\alpha = 3.5°$ (see Fig. 4b). The single dividing surface will continue to grow until the primary vortices induce a downward component of flow velocity along the leeward meridian. Thereafter, the height of this leeward dividing surface will diminish.

As angle of attack increases still further to 15° (Figs. 1f, 2e, 4c) the character of the flow remains the same, but the streaks near the nose cap caused by the crossflow instability are even more noticeable. Close to $\alpha = 19°$, however (Figs. 1g, 2f, 4d), the skin-friction line pattern entertains two additional structural instabilities, whereupon we now see evidence of two additional pairs of spiral nodes that have formed very close to the join-line between the hemispherical cap and the cylinder. Figure 2f illustrates the substantial increase in the overall number of singular points in order to incorporate these two additional pairs of spiral nodes. The intricacies in the patterns are especially interesting; they have been studied previously by Hsieh (Ref. 3) and Hsieh and Wang (Ref. 4), and more recently by Hsieh (Ref. 5) in an attempt to refine the computational scheme proposed for the flow field by Pulliam and Steger (Ref. 6). In those papers, details of how the spiral nodes combine with other singular points in the pattern of skin-friction lines on the leeward foreparts of the body have been especially elusive. The description advanced herein from our own experimental results updates that offered by Peake and Tobak (Ref. 7) and by Tobak and Peake (Ref. 8) from oil-flow pictures kindly supplied by T. Hsieh. As we have seen, recognizing the existence of a nodal point of separation on the leeward ray accounts for an essential feature of the flow structure. Nevertheless, the downward induction effect of the primary vortices along the leeward ray is particularly significant, so much so that the single dividing surface along the leeward ray has reduced substantially in extent by the time the given laser vapor-screen crossflow image is reached along the body (Fig. 4d). As we see in the range $0° < \alpha < 19°$, there is no evidence that the eruptions from the spiral nodes appear in the crossflow plane, unlike the flow fields viewed by Jorgensen (Ref. 9) about tapered blunt-nosed bodies.

The characteristic dividing surface in the external flow formed from the combination of an adjacent saddle point and a spiral node (see also Fig. 4 in the preceding paper) has been termed a "horn-type" dividing surface by Legendre (Ref. 10). The patterns in Figs. 2b to 2f are drawn on the assumption that there is no mechanism available to alter the already existent nodal and saddle singular points of separation on the leeward ray — this extends to higher angles of attack also — and that these may then be coupled to the spiral nodes via additional singular points. The summation of nodes and saddles on the surface must always differ by two; this rule is obeyed if we take the simplest conjectural case that all skin-friction lines disappear into a node of separation at the tail. Any elaboration of this one node of separation into an appropriate array of singular points to cap off the separation lines obviously can be introduced as required.

Our next pictures of the skin-friction line pattern at $\alpha = 27.5°$ (Figs. 1h and 2g) show the development of spiral nodes close to the commencement of the primary and secondary separation lines. Structural instabilities have again occurred in the skin-friction line patterns, and now we see that both primary and secondary separations are of the global type, each starting at a saddle point.

The final photographs in Fig. 1i at $\alpha = 32.5°$ evidence additional considerable complexity. It appears that relatively strong shock waves in the leeward crossflow are causing a significant predisposition of the primary separation line to split into a series of saddle points and spiral nodes along its initial length. Ripples in the skin-friction-line pattern to the leeward of the primary separation line are further indicative of shocks in the leeward crossflow. Moreover, we detect additional spiral nodes forming on the hemisphere cap itself.

Thus, in the sequence of changing α from 0° to 32.5° for the hemisphere-cylinder in transonic flow, where the shock-wave/boundary-layer interactions are evidently very complex, we have conjectured at least six separate structural instabilities in the skin-friction-line map to herald new topological structures in the surface pattern and in the external viscous/inviscid flow field. In addition, we have been able to discern on the basis of experimental evidence that these changes were accompanied by at least one asymptotic instability of the external flow, leading to a bifurcation flow. This was when the evidence suggested that the crossflow instability mechanism had led to the appearance of an array of streamwise vortices in the boundary layer (see Fig. 9 in the previous paper). We note that the concept of bifurcation — one flow replacing another flow that has become unstable — is principally a theoretical one; it is exceedingly difficult in practice to confirm that there is a flow other than the one observed that could exist in the absence of perturbations. It may be necessary to await the further development of theory based on the equations governing these flows before we can deduce the specific role played by bifurcations in determining the observed sequence of topological structures. We have also seen the particular developments of local and global lines of 3-D separation. Let us now look at some additional examples in which the formation of spiral nodes on other configurations substantially influences the flow-field structure.

3. RECTANGULAR WING: ASPECT RATIO 0.25

For the hemisphere-cylinder, the existence of a two-dimensional separation bubble at $\alpha = 0°$ allowed us to deduce easily how the singular separation and reattachment skin-friction lines were transformed into singular points as a result of the three-dimensional effects introduced by a small angle of attack. We saw that the favorable transverse pressure gradient from windward to leeward created conditions for the appearance of a nodal point of separation on the leeward ray. We can follow this approach to some extent with the rectangular wing as well by focusing our attention on the flow near the leeward centerline of the wing. In contrast with the previous flow, near the leading edge the transverse pressure gradient is favorable from leeward to windward and, as a consequence, we shall detect a saddle point of separation on the wing centerline. As an example of this behavior, Wickens' 1966 investigation of a low-aspect-ratio rectangular wing (Ref. 11) is such a case.

The oil-flow patterns taken by Wickens were on the leeward surface of a low-aspect-ratio (0.25) rectangular wing at an angle of attack of 20° (Fig. 5). This investigation was carried out in a low-speed wind tunnel, and we assume that the flow was laminar, at least on the forepart of the wing. Figure 6a is a deduction from Fig. 5 of the corresponding pattern of skin-friction lines; it represents the 3-D end-product of what had been, at very much lower angles of attack, a nominally two-dimensional separation bubble on the wing topside close to the leading edge. We see in Fig. 6a four spiral nodes, one nodal point of attachment, and five saddle points on the leeward surface, and that the windward surface must contain one nodal point of attachment (the stagnation point). Each of the five saddle points on the leeward surface separates the flows from adjacent pairs of nodes, a necessity in the buildup of the skin-friction-line topology (Ref. 12). Springing from the saddle points are dividing surfaces, the forms of which we attempt to portray in Fig. 6b. On each side of the centerline, we suppose that the primary separation consists of the dividing surface, which runs into the spiral node nearest the edge of the wing, taking the form of the "horn-type" dividing surface described previously by Legendre (Ref. 10).

Particularly noteworthy is the other spiral-node/saddle-point combination nearer the centerline of the wing. We see from Wickens' pressure measurements at $\alpha = 20°$ in Fig. 6d that there is a favorable pressure gradient from the wing centerline outboard toward the tip, supporting the argument for a saddle point on the topside wing centerline and a direction toward the tip of the local skin-friction lines. Note that in the case of the hemisphere-cylinder, the direction of the skin-friction lines around the forepart of the body was toward the leeward ray, and, that in contrast, we saw the emergence of a nodal point of separation there. Farther outboard in the present example (but inboard of the tip region) the combined effect of the spanwise and chordwise pressure gradients is to turn downstream the dividing surface originating at the centerline saddle point, and to wind it up into a spiral node. Emanating from the node into the flow is an isolated vortex filament which passes downstream, perhaps very close to the surface.

4. RECTANGULAR WING: ASPECT RATIO 3.5

We now extend the aspect ratio of the rectangular wing to 3.5 and examine the results of Winkelmann and Barlow (Ref. 13). Figure 7 shows one particular example (at $\alpha = 23°$) of many low-speed flows investigated by these authors. Figure 7a illustrates the surface oil-flow picture of the wing topside with some slight "run-down" of the oil toward the trailing edge, a result of stopping the wind tunnel. Nevertheless the essential features of the skin-friction-line pattern can be read from Fig. 7a; they are shown in Fig. 7b. The skin-friction-line trajectories that were evident in the Wickens flow in Fig. 6 appear in analogous form very close to the leading edge of the present example. Downstream of the flow reattachment at the node N_a on the centerline; however, we find another saddle point of separation, the separation line from which terminates in a pair of large spiral nodes covering an extensive area of the wing. The wing-tip line of separation shown in Fig. 6a in the Wickens flow is now situated inboard in the Winkelmann flow, and winds up into the large spiral node. By our definition, all separation lines starting from saddle points of separation are global separation lines. Notice now, however, that the separation line at the wing tip, providing the wing-tip vortex, originates from the attachment node on the underside centerline and is hence, again by definition, a local line of separation. This local line of separation terminates in another spiral node close to the trailing-edge tip.

We should comment that the external viscous/inviscid flow away from the wing surface is usually quite unsteady for angles of attack of the order of 23°, which is past the point of maximum lift coefficient. The oil pattern is essentially responsive to only very low frequencies and thus provides a time-mean of the instantaneous skin-friction-line pattern. The view of the external flow along the centerline of the wing must be construed similarly.

5. HIGH-ASPECT-RATIO SWEPT WING OF TRANSPORT AIRCRAFT

The next example we wish to comment on is a high-aspect-ratio swept wing immersed in a high subsonic speed environment close to the angle of attack at which buffet onset occurs (Fig. 8). A substantial pressure rise through a relatively strong swept shock wave on the wing topside dominates the flow-field development over almost the entire semispan, causing a swept 3-D separation line (see Fig. 8a). Toward the root, the single shock-wave structure would appear to split into the well-known lambda form, with a fairly strong forward leg and a weak aft-shock. Close to the shock-wave triple point, we detect a large spiral node in the pattern of skin-friction lines in conjunction with a saddle point of separation and a nodal point of separation.

An examination of the oil-flow picture in Fig. 8a and the conceptual skin-friction-line pattern in Fig. 8b for this swept-wing example demonstrates the close analogy with the combination of singular points (node of separation/saddle point/spiral node of separation) that exists on the top of the hemisphere in Fig. 1.

6. SLENDER DELTA WING

About the simplest of all cases of 3-D separation is the flow field about a slender delta wing at angle of attack (Figs. 9, 10). It is well known that the characteristic feature of this flow is the appearance of free-shear layers that coil tightly around dividing surfaces of separation springing from the leading edges. Figures 9 and 10 show, respectively, typical patterns of limiting streamlines and skin-friction lines on the top surface of a delta wing with a 15° semiapex angle, at $M_\infty = 0$ (Fig. 9) and 1.95 (Fig. 10). We see at $\alpha = 25°$ for this wing the existence of primary and secondary separation lines at both Mach numbers, giving rise to primary, secondary, and possibly tertiary vortices. Beneath the cores of the primary vortices, the wing experiences peak suction pressures. However, the origin of the dividing surfaces and their detailed behavior in the vicinity of the apex remains conjectural. On the theoretical side, the difficulty is associated with the presence of sharp edges which violate ideas about analyticity; on the experimental side, the difficulty is associated simply with insufficient powers of visual or instrumental resolution.

Theoreticians have attacked the problem by focusing on a small region of the apex and magnifying the scale to a degree such that the edges there appear to be rounded enough to dispose of the question of analyticity. Then it is reasonable to assume that just as for smooth round-nosed bodies, the flow in the vicinity of the apex must be describable within the framework of rules governing the behavior of singular points. The assumption is not sufficiently exclusive to enable the determination of a unique flow pattern but only a number of physically plausible ones. For example, if we restrict ourselves to the low-angle-of-attack case in which a primary separation line exists, we may have only a simple node of attachment on the apex resulting in local lines of separation on the wing. Presuming the sequential flow development around the apex to follow the case of a blunt-body flow already discussed in the previous paper, then as the angle of attack is raised at sufficiently high Reynolds number, we will expect the apex flow to bifurcate from a uniform attached flow to a flow with tiny streamwise vortices immersed within the boundary layer which will subsequently coalesce to form the primary separation. That such streamwise vortices, resulting from, in this case, instability of the crossflow velocity profiles near the leading edge, can exist on a slender wing is evident in Fig. 11, for example. At higher angles of attack, it is reasonable that the array of singular points proposed by Legendre (Ref. 16) or Lighthill (Ref. 12) (see Fig. 12) may also be candidate topologies on the apex. Note that when effects of the base become dominant as angle of attack becomes very large, substantial spiral nodes may form on the rear surface of the delta wing (see Fig. 13). Whether the leading-edge shape of the slender wing is straight, of ogival form, or of ogee form, qualitatively (i.e., from the topological standpoint) the skin-friction line patterns and the external flow streamlines are virtually identical for the three forms.

We now wish to demonstrate the benefit of combining a slender-wing type flow with that about a small-aspect-ratio swept-back wing under transonic conditions where, utilizing our topological notions, we are able to deduce the flow-field structure from some experimental results, the oil-flow picture from which is not totally definite.

7. LOW-ASPECT-RATIO SWEPT WING OF FIGHTER AIRCRAFT

The large leading-edge extension or strake offers the advantage that induced lift provided by the vortices from the sharp edges can be used to extend the combat-maneuvering capabilities of a fighter aircraft, particularly in transonic flow. Improvements in lift boundary and reductions in rolling moment unsteadiness and root-mean-square wing-root bending moments can be realized as a result of the drastic alteration of the wing-root flow caused by addition of the strake (see Figs. 14a to 14d). Küchemann (Ref. 18) has suggested that the strake vortex avoids the necessity for the formation of the usual forward branch of the wing-shock pattern by providing a "soft" boundary for the flow turning inboard over the leading edge, instead of the "stiff" boundary given by the fuselage side.

Figure 14a illustrates some experimental measurements reported by Moss (Ref. 19) of contours of constant pitot pressure and vorticity behind a straked wing at angle of attack. Figure 14b shows a sketch (Moss, Ref. 19) of the oil-flow pattern on the top wing surface at a slightly lower angle of attack than that at which the contours were taken, but, nevertheless, where the same overall qualitative flow features hold. These experimental observations, taken together, allow us to synthesize patterns of skin-friction lines (Fig. 14c) and external flow streamlines (Fig. 14d) that although still conjectural, offer a rational description of the complex separation phenomena.

Clearly, the effect of the strake is to split the wing flow field into two regions, each with a dominant vortical structure, of the same rotational sense. The strake modifies the wing-root flow to one of a slender-wing-type flow, with both primary and secondary vortices. Further outboard, the termination of the separation line beneath the strong shock wave near the leading edge is considered to be at a spiral

node N_1 on the wing surface, of counter-rotating direction to the larger spiral node N_2, shown in Moss' sketch (Fig. 14b). These spiral nodes produce a T-shaped pattern of vortical structures in the crossflow which are clearly evident in the wake traverse plane showing vorticity contours (Fig. 14a) downstream of the trailing edge. (Note the wing downwash field has moved the rotational flow from these spiral nodes below the level of the trailing edge in Fig. 14a.) At the junction of the wing trailing edge with the fuselage, we may infer the likelihood of another spiral node (see Fig. 14d of Peake and Tobak, Ref. 7). The respective topological rules for the surface skin-friction line pattern on Fig. 14c and for the crossflow plot in Fig. 14d are satisfied, as shown on the illustrations. Again we should be cognizant of the spiral-node/saddle-point formations in both the pattern of skin-friction lines and in the crossflow pattern, in direct analogy with those formations witnessed on the hemisphere-cylinder at angle of attack.

8. CIRCULAR CONE

Next to the flow about a lifting slender delta wing, the flow about a slender cone at angle of attack is the simplest 3-D flow field that may be envisaged. The cone, moreover, is a common forebody shape used in the design of supersonic flight vehicles. If viscosity is neglected, the flow field about the cone in a supersonic free stream has the unique property that no changes in flow quantities occur along rays (i.e., in direction r) emanating from the cone apex. The stream surfaces projected on to concentric spheres centered at the apex (called conical flow streamlines) are then similar. In practice, experimenters have demonstrated that many features of the viscous/inviscid interacting flow field — such as bow shock-wave locations, circumferential pressure distributions, normal force coefficients, circumferential positions of separation lines, and surface shear-stress directions — are conical or nearly so. The growth of a laminar viscous layer cannot be conical, because it develops according to $r^{0.5}$. In a fully turbulent flow, the exponent of r is nearer unity, implying a flow field very close to conical conditions.

When the Reynolds number is sufficiently high so that transition occurs in proximity to the apex, the near-conical nature of the experimentally measured flow demonstrates a virtual absence of length effects in the streamwise direction: the flow is dominated completely by the circumferential pressure field (Refs. 20-23). Thus, the characteristics of these flow fields can be determined through measurement or by computation at essentially one streamwise station. In fully turbulent and fully laminar subsonic free-stream flow, even though base and thickness effects become measurable, the circumferential pressure gradients still dominate, to the extent that virtual conicity of the separation lines and shear-stress directions is still maintained. Then, because the effects of axial pressure gradients are subsidiary to those of circumferential pressure gradients on most other slender pointed forebody shapes, we may use the cone as a suitable model to obtain a basic understanding of forebody flows.

9. SYMMETRIC THREE-DIMENSIONAL SEPARATED FLOWS ON THE LEEWARD OF CONES

About the cone, the three-dimensional separation zone may be precipitated at circumferential angles ϕ of 120° or greater (measured from the windward ray), depending on relative incidence (angle of attack α divided by cone semi-nose angle θ_c), Mach number, and Reynolds number (see Fig. 63 in Peake and Tobak, Ref. 7). Provided that the viscous flow is either all laminar or completely turbulent from the apex, the windward boundary layers separate from primary separation lines that are along conical rays, rolling up into well-organized vortex structures situated close to the leeward meridian. The new leeward boundary layers grow outboard on each side of the leeward meridian by the induced swirling motion of the primary vortices. At sufficiently high angles of attack, they also separate from additional conical separation lines to form small secondary vortices that are tucked beneath and are of opposite rotation to the primary vortices. Whether, for a sharp apex, the separation lines (which are particular skin-friction lines) emanate from either the nodal point of attachment at the apex, or from saddle points very close to the nose in the continuous pattern of skin-friction lines, has not been resolved (see Sec. 6). Nevertheless, sequences of plausible skin-friction line patterns with saddle singular points in the vicinity of the nose as angle of attack is increased may be drawn (see, e.g., Peake and Tobak, Ref. 7).

The structure of the symmetric separated flow about a slender cone at angle of attack with both primary and secondary vortices on the leeward has been well established in experiments (e.g., Rainbird, Refs. 20, 21) and computations (e.g., McRae et al., Ref. 24) and is illustrated in Fig. 15. This drawing shows a conical flow projection with the zero velocity points (i.e., singular points in this projection) that govern the pattern of the conical-flow streamlines. Note that the topology law for the conical flow projection is satisfied (see Eq. (10) in our previous paper). The shear layers departing from the surface at the three-dimensional separation lines are depicted by their dividing surfaces starting at half-saddle points, S', and coiling into vortices, the nodal foci N. The remaining half-saddle points S' denote attachments to the surface in this projection. Above the primary vortices in the plane of the leeward meridian is an enclosing saddle point S and a node N. This node is the point in the conical flow projection where most of the conical streamlines in the external flow "disappear." In the three-dimensional flow, of course, all flow at such singular points is concentrated along a conical ray.

Figure 15 presents the conceptual model of the flow field that has been investigated in flight and in the wind tunnel. The experiments (Ref. 23) proceeded under subsonic and supersonic free-stream conditions (M_∞ = 0.6, 1.5, and 1.8) and at an angle of attack of 11° (relative incidence of 2.2). The same sharp 5° semi-angle cone and instrumentation were used both in flight and in the wind tunnel (see Fig. 16). Numerical computations were run for the Mach number 1.5 and 1.8 conditions, with a code utilizing the conically symmetric Navier-Stokes equations (Ref. 24). Details of the cone surface conditions beneath the turbulent viscous flow are presented at Reynolds numbers of typically 4×10^6 for the wind-tunnel measurements and 10×10^6 for the flight measurements; they are compared with computations. These Reynolds numbers are based on free-stream conditions and on a 30-in. (76.2 cm) axial length to the first measuring station on the cone surface.

9.1 Mean Static Pressures at the Cone Surface

Figures 17 and 18 illustrate circumferential static pressure distributions on the cone surface at the test Mach numbers of 1.8 and 1.5. The pressures are shown for the station 30 in. (76.2 cm) from the cone apex, with the outputs from four orifices at 90° intervals around the surface plotted in the same figure (Fig. 17). In addition, measurements are also provided at x = 31, 33, and 35 in. (78.7, 83.8, and 88.9 cm) (Fig. 18). The pressure distributions displayed virtual symmetry about the meridian plane, so that only measurements made on one side of the cone are presented.

The respective flight and wind-tunnel Mach-1.8 results at station 30 are shown in Figs. 17a and 17b. The results are plotted as surface mean pressure coefficients versus circumferential angle ϕ, where the windward generator is recognized at $\phi = 0°$. The experimental results are plotted with symbols, and the computed results are plotted with a continuous line. The flight and wind-tunnel data are in reasonable agreement in both trend and magnitude. The high quality of the flight data is especially noteworthy: the static pressure outputs at station 30 are virtually superimposed. However, some discrepancies appear near the windward ray and toward the leeward ray in the zone where the primary and secondary separations exist ($\pm 140° < \phi \leq 180°$). Note the suction peak close to $\phi = \pm 165°$, which signifies the presence of the primary vortex core above the surface.

The computation duplicates the trends in the measurements, especially on the windward side. On the leeward, however, the numerical results provide a more positive level of pressure, although the suction peaks beneath the vortex cores are close to the experimental locations.

Figure 18 portrays the flight circumferential pressure distributions at Mach 1.5 along the cone at four axial stations, x = 30, 31, 33, and 35 in. (76.2, 78.7, 83.8 and 88.9 cm) from the apex. The pressures along the cone are virtually invariant, confirming the near absence of length effects at supersonic Mach numbers.

Thus, from Figs. 17 and 18 it may be deduced that up to the flank position on the cone, the boundary layer develops from the windward ray and undergoes acceleration in a very favorable pressure gradient. Once past $\phi = 100°$, the viscous flow encounters a stiff adverse pressure gradient, departing from the surface at the primary separation line, ϕ_{S_1}. The thin boundary layer that then develops from the leeward attachment line does so in the region of favorable pressure gradient from $\phi = 180°$ to about 165°. Subsequently, the flow separates at ϕ_{S_2}. The experimental primary and secondary separation line positions marked in Figs. 17 and 18 are given from the pressure distributions obtained with the obstacle blocks described below. These measurements of $\phi_{S_1} \approx 142°$ and $\phi_{S_2} \approx 157.5°$ are demonstrated to be in close agreement at both supersonic Mach numbers; the computations, on the other hand, predict values of ϕ_{S_1} and ϕ_{S_2} that are marginally displaced toward the windward side.

9.2 Obstacle Block Pressures and Separation Line Position

To determine separation-line positions where use of an oil indicator on the surface is inappropriate, obstacle blocks (Refs. 25-27) may be used. These are small machined cuboids that are attached to the cone surface abutting static pressure orifices, as shown in Fig. 19. The performance of the block is analogous to that of a surface pitot tube, the signature from which is sufficiently sensitive to yield either a large increase in amplitude through a transition zone (Ref. 28) or well-defined troughs at three-dimensional separation lines (Ref. 24).

Figure 19a indicates block-pressure coefficients $CPB = (p_b - p_{local})/q_\infty$ obtained at the four pressure orifices at station 30 for the Mach 1.8 flight case. These results compared very closely with the wind-tunnel results (see Fig. 19b). The pronounced troughs in the values of CPB close to $\phi = 140°$ and 160° denote the primary and secondary separation line positions where the skin friction has a minimum but finite value. (Only at the singular points at which the separation line begins and ends is the magnitude of the local skin friction equal to zero in a three-dimensional viscous flow.) Note the elevated values of CPB toward the attachment lines where the boundary layers are thin: at the windward ray, leeward ray, and between the separation lines. In the wind-tunnel tests, the block outputs at stations 30 and 30B were calibrated directly against Preston tubes at stations 30A and 30C with the cone at 0° angle of attack. The Preston-tube calibration for compressible flow developed in Bradshaw and Unsworth (Ref. 29)(with slight modifications[1]) was used to give skin-friction magnitudes. Figure 19b indicates the corresponding skin-friction levels obtained from the blocks at high and low point values of CPB at $\alpha = 11°$. Results analogous to those at Mach 1.8 were obtained at Mach 1.5 and 0.6. The measured and predicted primary and secondary separation line positions are shown in Figs. 17a and 17b.

Some details of the external mean flow field are captured in the Mach 1.8 computed pitot contours shown in Fig. 20. Here, the height above the surface H is a fraction of the local radius of the cross section. The dividing surface from the primary separation line location ϕ_{S_1} is shown as a chain-dot line; the locus of the inflexional zero velocity point in the crossflow velocity profiles (in the conical projection) is indicated as a dashed line. There is close qualitative agreement between this computed result and previously published measurements in the external flow (Rainbird, Refs. 20, 21; Peake et al., Ref. 30). It shows the extensive domain of the primary vortex close to the leeward ray, with the vortical core immediately above the circumferential angle $\phi = 166°$, exactly where the calculated suction peak appeared in the Mach 1.8 static pressure distribution in Fig. 17.

9.3 Surface Shear-Stress Directions

The computed limiting streamline angles relative to conical rays can be compared with the experimental surface shear-stress directions obtained by oil-dot surface flow visualization in the wind tunnel. To provide a complete map of the wall shear-stress directions, precisely cut tracing paper was placed on the

[1]Private communication from P. Bradshaw.

cone surface, and oil dots were applied around the circumference at given axial stations prior to a tunnel run. After the run, the paper was carefully unwrapped from the cone and photographed to give a flat projection. Figure 21 presents a section of one of these photographs taken for a Mach-1.8 run at 12.5° angle of attack in the wind tunnel. This angle is higher than the 11° test condition presented thus far; the skin-friction line map, however, is qualitatively identical at both angles of attack. The limiting flow at the base of the three-dimensional boundary layer sweeps around the cone from the windward ray, and then turns to approach asymptotically the primary separation line in the region of circumferential adverse pressure gradient (Fig. 17b). The leeward boundary layer grows outboard from the leeward meridian (a line from which the adjacent skin-friction lines diverge) to approach asymptotically the secondary separation line. As Fig. 21 shows distinctly, there is another reattachment line between the primary and secondary separation lines (see also Fig. 15).

The computed limiting streamline angles are drawn in Fig. 21 for a Navier-Stokes calculation equivalent to the experimental conditions. The computed separation lines are shown as solid lines and reattachment lines by dashed lines. The lines are repeated at the base of the cone for clarity. The agreement between the computational results and the experiment is good.

9.4 Fluctuating Pressure Measurements on the Cone Surface

Microphone and Kulite pressure signatures were obtained at $\alpha = 11°$ in flight and in the wind tunnel at the station 34 in. (86.4 cm) from the apex as the cone was rolled about its axis. All microphone and Kulite data provided the same qualitative trends in a given test, but absolute levels did vary slightly, perhaps as a result of minute differences in flushness of the installation of the sensors in the cone surface,

Measurements from one microphone obtained at Mach 1.5 in the wind tunnel are shown in Fig. 22 as root-mean-square values of the surface pressure fluctuation $\langle p \rangle$, normalized by the free-stream mean dynamic pressure q_∞. The characteristic feature of these measurements is the progressive reduction in signal amplitude as the primary separation line ϕ_{S_1} is approached, with a similarly low level at the secondary separation line ϕ_{S_2}. This feature was found at all Mach numbers and was witnessed in an earlier investigation (see Peake et al., Ref. 31). The signal amplitude climbs again toward the leeward attachment line to a level close to that on the windward ray attachment line. Not understood, however, is the reason for the changing amplitudes in the attached flow around the flank of the core. Note that the fluctuation level on the windward ray at $\alpha = 11°$ is close to that measured at $\alpha = 0°$, and to the free-stream fluctuating static pressure in the empty tunnel. The flight measurements yielded signal levels typically one order less than in the wind tunnel, with much less relative distinction between those levels at the separation and attachment lines.

Figure 23 shows sample wind-tunnel power-spectral density results indicating a reduced energy level at primary separation relative to the windward and attachment-line boundary layers. When, on the other hand, the root-mean-square pressure output is normalized by the local value of skin friction, characteristic peaks (again see Peake et al., Ref. 31) are demonstrated at the primary and secondary separation line, as we see in Fig. 24. In other words, as separation is approached, the local skin-friction decreases at a faster rate than does the root-mean-square pressure fluctuation. We see that the "roller'coaster" region around the flank in Fig. 22 does not translate into a similarly obvious region in Fig. 24; rather, there is a relatively smooth enhancement of $(\langle p \rangle / \tau_w)$ in the ϕ range $40° < \phi > 120°$. Note that there is a noticeable peak in the wind-tunnel spectral outputs in Fig. 23 at 1.6 kHz. This appears to be a harmonic of the fan rotational speed, rather than a characteristic feature of the flow-separation phenomena or a discrete tone from the slots in the tunnel working section, since the same peak was also observed on the $\alpha = 0°$ runs, with and without the slots sealed. Finally, the value of measuring the fluctuating pressure at the surface of the cone has been that it provides a qualitative guide as to how the eddy viscosity distribution should be tailored in the computation (Ref. 23). It appears that the eddy viscosity should rise and fall in sympathy with the absolute fluctuating pressure signal.

10. SEPARATED FLOW ABOUT LONG SLENDER BODIES

The body of a typical missile or rocket consists of a low-drag nose shape attached to a circular cylindrical afterbody. The afterbody is about 10 body diameters in length and has stabilizing fins or a flare mounted close to the base end. Such long bodies are very prone to flow separation once they depart from a zero angle of attack flight condition. To oversimplify the picture, we may regard the long cylinder as a cone of essentially zero included angle and so for any small angle of attack, the relative incidence is very large and separation is inevitable somewhere down the body. The typical separated flow regimes encountered on the leeward with increasing angle of attack are (1) a symmetrical vortex wake about the meridian plane; (2) a relatively steady asymmetric vortex wake; and (3) an unsteady diffuse vortex wake. These regimes are illustrated (Figs. 25a-25c) in side elevation in the water-tunnel experiments of Fiechter (Ref. 32) for a tangent-ogive cylinder up to angles of attack of about 60°.

10.1 Steady Symmetric Separations

On very long pointed or blunt-nosed slender configurations, separation first occurs symmetrically with a pair of vortices trailing back along the body. Figure 26 illustrates such body separations in side elevation on a blunted cone-cylinder-flare model at a low relative incidence in a Mach 4 airstream. The separations and vortex wake are recognizable in the photograph at about 1-2 body diameters behind the cone-cylinder junction and proceed downstream on the lee of the body in a well-ordered and structured fashion (see Fig. 25a). These symmetric vortices are virtually identical in form in the crossflow plane at corresponding relative incidences, provided the crossflow is subsonic. By way of example, Fig. 27a shows the crossflow about an ogive-cylinder at 20° angle of attack at $M_\infty \sim 0$, made visible with dye and aluminum particles in a water-tunnel study by Werlé (Ref. 33). The close analogy between this low-speed case and a Mach-2 wind-tunnel result for another ogive-cylinder at 26° angle of attack (Ref. 34) is revealed in Fig. 27b. The figure shows a composite of laser vapor-screen photographs for various crossflow planes along the body, assembled in an isometric view. Both primary and secondary vortices are observable.

Careful measurements of the crossflow velocity vectors and contours of constant pitot-pressure deficit in low-speed symmetrical flow were made by Grosche (Ref. 35), as shown in Figs. 28a and 28b. The pitot contours display evidence of both the primary and secondary separations that were seen on the cone in Fig. 20. Note in Fig. 28c that when a wing is added to the body at the same angle of attack, there is a substantial shift in the position of the body vortices as a result of the larger induced effects of the controlled flow separations at the edges of the swept wing.

Some painstaking experiments on missile configurations at angle of attack were made by Boersen (Ref. 36) to elucidate the fine details of the skin-friction line patterns. Figure 29 shows some of his results. Figure 29a displays the local primary separation line in turbulent flow along a $\theta_c = 20°$ blunted cone-cylinder (without flare or fins) at a low relative incidence of 0.6, $R_{L_\infty} \sim 10 \times 10^6$, and at Mach 2.3. The flow is symmetrical about the meridian plane but notice (on the unwrapped surface of the cylinder) in Fig. 29b, the gradual convergence of the skin-friction lines emanating from the clearly defined windward attachment line zone, followed by the very abrupt turning into the local primary separation line S_1. The induced downflow between the primary vortices (Fig. 27a) causes a rapid divergence along the leeward generator A_1, toward the apparent beginning of local secondary separation region S_2. Naturally, if we maintain our hypothesis of demanding patterns of continuous skin-friction lines associated with a limited number of singular points, the attachment and local separation lines that are very evident in these elegant flow visualization studies of Boersen (Ref. 36) must emanate from the attachment node on the surface at the nose. Only when the local circumferential pressure gradients become sufficiently adverse do we see the rapid turning of skin-friction lines to form asymptotes to the particular skin-friction lines that are the local primary and secondary separation lines.

Changing the forebody to a $\theta_c = 20°$ sharp cone (see Fig. 30a) at the same relative incidence of 0.6 (Ref. 36) produces no substantial change to either the flow symmetry or to the commencement of the 3-D separated region, but a tertiary and even a fourth separation line are now observed on the downstream part of the cylinder. (Again, we assume these to be local separation lines). Circumferential pressure distributions at the axial stations identified in Fig. 30a are plotted in Fig. 30b, where increasing Reynolds number is demonstrated to typically enhance the magnitude of the suction pressures, particularly those beneath the primary vortices. Note that the windward generator is on the right-hand side of the figure, and circumferential angle increases toward the left, the reverse notation to that used, for example, for the cone in Fig. 18. At station 1, the circumferential pressures are still dominated by the apparent attached viscous flow leaving the pointed conical forebody and no observable separation has developed just downstream of the cone-cylinder juction, even though the circumferential pressure gradient is adverse between $120° < \phi < 180°$. Except near the cone-cylinder junction, the axial pressure gradients are negligible. Beyond the minimum pressure point at stations 2 - 5, however, close to $\phi \sim 90°$, the circumferential adverse pressure gradient has steepened sufficiently to provoke primary separation near the flank. At station 3, the pressure distribution is reminiscent of the cone flow in Fig. 18, with the primary and secondary separations present (compare also the oil flows in Figs. 21 and 30c). At subsequent stations downstream along the cylindrical afterbody, further very sharp changes in the curvature of the pressure distributions are detected, consistent with possible embedded shock waves at positions c and d in Fig. 30c, and the associated development of additional local separation lines at positions e and g. A tentative sketch of the crossflow is provided in Fig. 30c, which differs in some respects from that proposed by Boersen (Ref. 36).

These body separations have an important effect on the vehicle's static and dynamic stability. At small relative incidences, where the separation is essentially steady and symmetrical with respect to the angle-of-attack plane, the ensuing body vortices produce a nonlinear contribution to the overall normal force and pitching moment. If the fin system is not symmetrically orientated with respect to the angle-of-attack plane, however, a cross-coupling side force, yawing moment, and rolling moment can arise, even at small angles of attack.

Flows such as these were studied extensively in the 1950's, particularly at NASA, by Jernell (Ref. 37) (cone cylinders and ogive cylinders, $0° < \alpha < 180°$) and by Jorgensen and Nelson (Refs. 38, 39) (cylinders with assorted nose shapes and bodies of elliptical cross section). A summary of these latter experiments and force predictions from crossflow methods is given by Jorgensen (Ref. 40). A good understanding, in an overall sense, has been obtained on the development of both forces and moments. An estimate, in incompressible flow, of the overall forces and moments acting on a slender body of revolution without fins was offered by Küchemann (Ref. 41), summarizing an analysis done 20 years earlier. Vortex sheets, as plane vertical surfaces, were assumed to exist all along the cylinder and the vorticity vector in the sheet was assumed to lie in a direction halfway between the direction of the free stream and the body axis. Results of typical calculations utilizing this very simple symmetric model are shown (Fig. 31) to be in quite reasonable agreement with experimental results.

To demonstrate the effects of nose shape, a series of tests at high Reynolds number was reported by Peake et al. (Ref. 42) who summarized the experiments of Atraghji (Refs. 43, 44) on the characteristics of a family of 16 pointed conical and tangent-ogives attached to cylindrical aterbodies (see Fig. 32). Each nose could be fitted to a cylindrical afterbody length of either 6 or 12 body diameters, but there were no stabilizing fins attached. Forces and circumferential pressures were measured, and the oil dots applied to the surface of the models yielded the patterns of skin-friction lines. At low angles of attack (typically up to $\alpha \sim 3°$) where there was attached flow, the slope of the normal force/angle-of-attack plot, C_{N_α} increased with Mach number and semi-nose angle, θ_c (see Fig. 33). The effect of overall slenderness ratio L/D was less clear, although at $M_\infty = 0.5$ the trend was established of an increasing C_{N_α} with L/D. Calculations using slender body theory (Ref. 45), the USAF "Datcom" data sheets (Ref. 46), and the method due to Öhman (Ref. 47) were also performed. As a general rule, the theories appear to underpredict C_{N_α} at a given semi-nose angle and slenderness ratio.

In the range of angle of attack (characteristically, $\alpha = 3°$ to $11°$) for the series of nose shapes tested, three-dimensional leeward flow separation is symmetric. The induced suction pressures from the rolled-up shear layers generate a large nonlinear normal force component, but no side force. With the normal force represented by a quadratic in α:

$$C_N = K + b_1\alpha + d_1\alpha^2$$

where K only removes the experimental uncertainty in the true measurement, Fig. 34 illustrates the increase in coefficients b_1 and d_1 with both Mach number and slenderness ratio, with a significant variation in d_1 at a given Mach number and slenderness ratio attributable to the semi-nose angle, θ_c. The more slender ogives listed in Fig. 32 (07, 09, and 011) would appear to generate a larger nonlinear lift throughout the Mach number range and for both afterbody lengths.

Rational calculations of the symmetrical separated flow field about long slender bodies at angle of attack are few. Development of a "Navier-Stokes" computational technique similar to that used by Pulliam and Steger (Ref. 6) to determine the separated flow about a long blunt body at moderate angle of attack (see discussion of the hemisphere-cylinder, Sec. 2) should be encouraged, to attain finer resolution of the flow-field details in the vortex wake and on the surface.

10.2 Asymmetrical Separations

At relative incidences of long slender bodies higher than those just discussed, say for values typically more than 2, separations and body vortices become asymmetric but still relatively steady in space. The result is that large side forces, yawing moments, and rolling moments are developed, especially on fin-stabilized vehicles.

The onset of asymmetry and the initial direction of the side force are responsive to small changes in geometry at the nose, Reynolds number, Mach number, and perturbation level of the free stream up to angles of attack where conditions in the leeward crossflow become transonic. In addition, the maximum overall side forces are particularly sensitive to the roll orientation of the body. As speed increases further, the significant side forces disappear (Ref. 42). The asymmetries occur in laminar, transitional, and turbulent flows. Nevertheless, the implication from recent tests by Lamont (Refs. 48, 49) with tangent-ogive cylinders at angle of attack (at Reynolds numbers encompassing laminar, transitional, and turbulent boundary-layer separation) is that the vortex wake is less structured in the transition domain, leading to reduced side and normal forces at a given subsonic Mach number. In the fully laminar or turbulent regions, on the other hand, where the organization of the flow field is well defined, the respective magnitudes of the side force are larger and are closely matched — see Fig. 35, in which the results for maximum side force versus Reynolds number are plotted for a missile with a 2-D ogival nose and a 5.5-D body (Lamont, Ref. 48).

There appear to be two candidate mechanisms that cause the development of asymmetry in the leeward vortex wake, and hence produce side force. The first, which appears to operate in both the laminar and fully turbulent separation regimes, may be related to the stability of the velocity profiles in the vicinity of the saddle singular point that exists in crossflow planes above the projections of the body vortices. The second may be a result of the occurrence of asymmetric transition leading to an effective asymmetric mean flow at given body cross sections. Although the second mechanism is operable only within the transition zone, the former mechanism plays a role in both laminar and fully turbulent flow (see Ref. 48, 49). It will be discussed further in the subsequent paper by Skow and Peake in this lecture series. Typical asymmetrical circumferential pressure distributions are shown in Figs. 36 and 37 for laminar, turbulent, and transitional body flows for the 2-D ogival nose, 5.5-D length afterbody of Lamont (Ref. 48).

In turbulent flow, certainly, it would appear that at forebody relative incidences where asymmetry of the vortex wake commences, we are always dealing not only with separation of the primary boundary layers that develop on each side from the windward generator, but with secondary separations of the leeward boundary layer in addition. The onset of asymmetry would seem to be characterized initially by a rapid, local movement circumferentially of one (or both) secondary separation lines followed, as angle of attack is increased further, by circumferential movement of the primary separation lines (Refs. 42, 50). The asymmetric skin-friction line pattern on the conical surface development shown in Fig. 38 illustrates this latter flow situation, with "wobbly" primary and secondary separation line traces existing all along the cone (Ref. 51). There, the free-stream Mach number is 2.94 and the relative incidence is 4.5. At lower free-stream Mach numbers, however, the asymmetric separation lines have been found to be conical (Ref. 30).

The asymmetric vortex wake usually develops from asymmetric separation line positions on the body, but the latter does not appear to be a necessary condition for the former to occur. An appraisal by Keener and Chapman (Ref. 52)) of some earlier, low-subsonic speed tests of Shanks (Ref. 53), in which forces and moments were measured on very slender, flat-plate, delta wings (sweep angles of 70° to 84°) at angle of attack, indicates that even though the separation lines were fixed at the sharp leading edges, asymmetry in the leading-edge vortices, as determined by the onset of significant rolling moment, occurred when the angle of attack was about 3 to 4 times the wing semi-nose angle. This angle of attack for asymmetry is splendidly illustrated on the vapor-screen pictures (Fig. 39) about another very slender delta wing immersed in a Mach 2.8 flow (Ref. 54). Nonetheless, the sharp edges have a beneficial effect in delaying the onset of asymmetry to higher relative incidences than those obtained with smooth pointed forebodies or forebody-clinder configurations (Refs. 42, 55, 56).

Because the development of the turbulent flow structures in the three-dimensional swept separation zones and in the tightly coiled free-shear layers is virtually unexplored, the modeling of the leeward flow asymmetries poses severe problems. Recourse has been made, for rough predictions of the flows about missile shapes, to inviscid flow approximations of the leeward region, utilizing arrays of line vortices (see the review by Nielsen, Ref. 57), of nonlinearities in missile behavior at high angles of attack). Alternatively, the impulsively started flow analogy proposed many years ago by Allen and Perkins (Ref. 58) has frequently been applied (Ref. 59). In this hypothesis, the development of the crossflow with distance along an inclined body of revolution is likened to the growth with time of the two-dimensional flow past the corresponding circular cylinder impulsively started from rest. Useful engineering formulae have certainly resulted utilizing the analogy. Nevertheless, given the complexities of the three-dimensional boundary-layer growth, separation, and vortex development about slender bodies at angle of attack, it is

intriguing that the impulsive-flow analogy can provide more than just qualitative details of the flow. If we restrict ourselves to invoking the impulsive-flow analogy to provide only the overall flow structure, the topologies of the 2-D unsteady and the 3-D steady cases appear virtually analogous (Ref. 60). If we demand stricter correspondence between the two, there are issues for debate. For instance, the growth of the unsteady 2-D vortex differs essentially from that of the steady 3-D vortex in space. Küchemann and Weber (Ref. 61) point out that in three dimensions, fluid entering the core of the vortex can be discharged axially, whereas in two dimensions no such escape is available. Thus, the 2-D core must expand continuously outward with time to accommodate all of the fluid entering the vortex. Küchemann and Weber show further that there is only one case in inviscid flow in which the two kinds of vortices are formally identical: where the steady three-dimensional flow is conical (so that slenderness assumptions can be invoked); and where the unsteady flow is permitted to grow linearly with time. Hence, if the development of the real viscous wake (in 2-D with time, and in 3-D with distance along the body) can be represented by these respective but special inviscid approximations to vortex growth, then the impulsive-flow analogy should be a suitable artifice under conditions of high Reynolds number.

For the missile at sufficiently high angle of attack, the asymmetric leeward flow is coupled with asymmetries in primary (and secondary) separation line positions. An example is shown in Fig. 40 where the asymmetric primary separation line positions on the port and starboard of a 5.8° cone-cylinder and a 13.9° ogive-cylinder, at Mach 0.6 and at identical angles of attack (18°), are plotted. The boundary layers are turbulent. This figure demonstrates the important influence of nose shape on the asymmetry of the flow. We detect that on the very slender conical nose, at its relative incidence of just over 3, there is substantial flow asymmetry all along the body (solid lines in Fig. 40). In contrast, because the less slender ogival nose is at a relative incidence of about only 1.3, the commencement of separation there shows only slight asymmetry, with less difference in separation line positions from side to side (dashed lines in Fig. 40).

Figure 41 illustrates the magnitude of the mean side-force coefficient C_Y with respect to the normal-force coefficient C_N, as model angle of attack is increased, for the selection of nose shapes shown in Fig. 32 with the 12-D afterbody length. Unsteady fluctuations in side-force coefficient, with peak-to-peak amplitudes as high as ± 0.3 at $\alpha = 25°$ were measured, superimposed upon the mean C_Y levels. For angles of attack up to about 27°, increasing either the semi-nose angle or the Mach number reduced the amplitude of the side force. In fact, at $M_\infty \approx 2$ when $\theta_C > 10°$, and for all configurations at $M_\infty = 3.5$, no measureable side force was obtained. Figure 42 presents the critical angle for flow asymmetry (judged by the side force exceeding, say 5% of the normal force) plotted against the semi-nose angle θ_C. As before, we confirm that the onset of flow asymmetry is delayed by increasing θ_C and Mach number. But the effect of the longer afterbody is to provoke asymmetry at a lower angle of attack.

Keener et al. (Ref. 56) attempted to draw some tentative boundaries based on angle of attack and fineness ratio between the various flow regimes that appear on the leeward of ogive-cylinder bodies in subsonic flow. Figure 43 illustrates these zones at Mach 0.6 for nominally turbulent viscous flows. We observe that three angle-of-attack boundaries are plotted as functions of overall fineness ratio, thus separating the angle of attack range of 0° to 90° into the three regions of different vortex formations that were introduced in Fig. 25. Recall that the regions are (1) regions of symmetrical steady vortices, typically up to angles of attack of about 1.5 times the semi-nose angle in subsonic flow; (2) regions of quasi-steady asymmetric vortex flows; and (3) at very high angles of attack, a "two-dimensional unsteady wake-like" flow. In Fig. 42, we detected in the high Reynolds number data of Peake et al. (Ref. 42) that the angle of attack at which the onset of asymmetric side-force development occurred was particularly sensitive to semi-nose angle, and less dependent on afterbody length. The data in Fig. 52 have been plotted again in Fig. 43. Along a given vertical bar representing fixed nose and afterbody fineness ratios, we see again the dependency of onset angle on semi-nose angle. The higher Reynolds number data of Peake et al. (Ref. 42) indicate the onset of asymmetry at lower angles of attack than the data presented by Keener et al (Ref. 56).

11. SHARP AND BLUNT CONES OF EQUILATERAL TRIANGULAR CROSS SECTION WITH ROUNDED CORNERS

There is a renewal of interest in fuselages of cross-sectional shape other than circular (see Hasel and Kouyoumjian, Ref. 64) to investigate whether flat-sided configurations (which can be more volume productive for housing avionics) may also provide improved aerodynamic performance, lateral stability characteristics, fuselage load distributions etc., at high angles of attack. A recent investigation at Ames Research Center by Clarkson et al. (Ref. 65) has concentrated on forebody shapes of rounded triangular and square cross section. From the extensive body of experimental results collected therein, we shall select for comment only a small sample dealing with the flows about sharp and blunt cones of triangular cross section at a particular angle of attack and Reynolds number. We shall see that the flow structures have many of the same topological features as those observed previously on sharp and blunt-nose bodies of circular cross section, under similar flow conditions.

Details of the sharp and blunt-nose triangular cone models are given in Fig. 44. Circumferential rings of orifices for surface pressure measurements were located at three axial stations as indicated in the figure. Tests were carried out in the Ames 12-ft wind tunnel at low speeds. The models were placed in the wind tunnel at angle of attack and at zero roll angle, the latter orientation being defined as occurring when a flat side of the model was directly windward.

Figure 45 present the results of oil-flow visualization experiments for the two models under essentially identical flow conditions (angle of attack = 45°, Reynolds number based on base height = 1.1×10^6 and 1.2×10^6 for the blunt- and sharp-nose triangular cone, respectively). Figure 46 presents the corresponding circumferential surface pressure distribution at the three axial locations indicated in Fig. 44.

Surface oil-flow patterns on the blunt-nose model (Fig. 45a) show evidence of primary and secondary lines of separation occurring on each flank of the body just after the flow has turned the corner of the blunt windward face. The primary separation is global, originating at a saddle point, and the secondary separation, occurring farther downstream, is local. There is an intricate flow on the leeward face of the

blunt nose, giving evidence of a pair of spiral nodes on either side of the plane of symmetry. Flow patterns here bear a resemblance to those over the nose of the hemisphere-cylinder at angle of attack (see in particular Figs. 1g-1i), in either case being the result of a series of abrupt local changes in both streamwise and circumferential pressure distributions. It will be noted that the surface flow pattern appears to be symmetric with respect to the angle of attack plane. This is borne out by the results of the circumferential surface pressure measurements (Fig. 46a), which are virtually identical on the port and starboard sides at all three stations.

Surface oil-flow patterns for the sharp-nose model (Fig. 45b) again show evidence of primary and secondary lines of separation. Here, however, it is probable that the primary and secondary lines of separation are local, both originating from the nodal point of attachment at the nose. Furthermore, the presence of a sharp nose eliminates the appearance of the intricate pattern of spiral nodes that was observed on the leeward face of the nose with the blunt-nose model. It is, however, the very marked asymmetry in the location of the secondary lines of separation in the oil-flow pattern for the sharp-nose model (Fig. 45b) that is the principal distinction between the patterns for the two models. This asymmetry is accompanied (see Fig. 46b) by a similarly marked asymmetry in the surface pressure distributions on the port and starboard sides at all three stations. There is reason to believe that just as for slender sharp-nose bodies of circular cross section (see discussion in connection with Fig. 37), the occurrence of this asymmetry, reflected first by the rapid circumferential movement of the secondary lines of separation, is associated with the onset of boundary-layer transition. Thus, just as for bodies of circular cross-section, it appears that for bodies of triangular cross-section, blunting the nose helps delay both the onset of flow asymmetry and boundary-layer transition.

12. SUPERSONIC INLET INTERACTING WITH FLOWS ON ADJACENT SURFACES

The half-cone or quarter-cone inlet mounted adjacent to a fuselage sidewall and wing/fuselage intersection may cause a substantial problem of swept shock wave/turbulent boundary-layer interaction, particularly at off-design conditions. The intake is usually raised from the fuselage surface to permit both bleeding and diversion of the oncoming viscous flows (Ref. 66).

Figure 47 shows an oil-flow pattern taken by Culley (Refs. 67, 68) about a $\theta_c = 25°$ half-cone intake at Mach 1.6 and at a Reynolds number of 6×10^6, based on the wetted run to the intake capture face of 2 in. (5 cm) diameter. The inlet was operating at design shock cone position and at maximum mass flow (with some spillage, as seen on the Schlieren photograph). Even though auxiliary ram (bleed) intakes were located in the plane of the cowl lip to ingest the turbulent fuselage boundary layer, there was clearly a substantial diversion of the fuselage boundary layer upstream of the bleed ducts. The fuselage flow was three-dimensionally separated by intersection with the intake pressure field, the separation line coinciding approximately with the projection of the cone shock on the fuselage wall. Thus it would appear that the most deficient portion of the fuselage boundary layer is spilled as vortices into the airplane flow field.

As an initial step in predicting this flow field, a calculation of the partial cone flow itself about the same $\theta = 25°$ half-cone at Mach 1.6 was performed (Peake et al., Ref. 69) but without a reflection plane. The pressure field that would be impressed upon the fuselage is approximately that existing between the shock wave and the half-cone, as shown in Fig. 48. The maximum overall pressure ratio between the shock and the cone is greater than 1.5, so that, as we saw earlier, 3-D separation would be expected.

Culley (Refs. 68, 70) also showed that with a quarter axisymmetric intake model, the use of a splitter plate to isolate the airframe boundary layer from the adverse influence of the intake could involve a multishock viscous compression and 3-D separation of the fuselage boundary layer upstream of the splitter plate (Fig. 49) that was not influenced by variations in the intake mass flow.

Other serious swept-shock/boundary-layer interaction problems in propulsion layouts may be encountered beneath supersonic wing planforms when designers attempt to take advantage of "favorable interference" effects (Refs. 71, 72) from compressions about engine nacelles and boundary-layer diverters.

Figure 50a shows the oil-dot flow pattern on the undersurface of a lifting 70° delta wing at $C_L = 0.08$ in a free-stream flow of $M_\infty = 2.75$ at a Reynolds number, based on the maximum wing chord, of 24×10^6 (Ref. 73). The four-nacelle arrangement is typical, in position and scale, of a supersonic transport layout. The two uppermost intakes were operating at design mass flow with cone shock on lip. One will note a small region of three-dimensional separation caused by the wedge-shaped pylons (diverters) and cowl pressure field in Fig. 50b, where the propulsion nacelles have been removed to facilitate inspection of the oil flow. The lower pair of intakes was throttled internally to about 70% design mass flow, forcing the throat normal shock outside of the cowl lip. The result of operating subcritically is to cause a massive three-dimensional separation of the starboard under-wing boundary layer and high local heat-transfer rates in the reattachment regions downstream of the separation. Figure 50c exhibits a postulated pattern of singular points and skin-friction lines in the region where the adjacent separation lines interfere with each other. The interference appears to result in the formation of a nodal point of separation interspersed between the two saddle points immediately ahead of each wedge-shaped diverter. A sketch of the streamlines in the streamwise plane of symmetry passing through the node of separation is also given in Fig. 50c. The accompanying changes in normal force are shown in Fig. 51. At a cruise lift coefficient of 0.08, occurring at an angle of attack of about 3° for this symmetrical wing, there is a 20% increase in lift from the throttling of the four intakes to 70% of the design mass flow; the corresponding increase in drag for subcritical operation is illustrated in Fig. 52. At off-design Mach numbers, the shock/boundary-layer interactions and resulting 3-D separations may be even more severe in their effects on drag.

13. CONCLUDING REMARKS

We have described the structure of 3-D separated flows about various types of aerodynamic components immersed in both low-speed and high-speed flows and encompassing the viscous flow regimes from laminar to turbulent. Typical components displayed have been slender shapes such as the cone (with circular and triangular cross sections), hemisphere-cylinder, and delta wing, a number of rectangular and swept wings of low and high aspect ratio, and supersonic inlets.

By holding strictly to the notions of continuous vector fields of skin-friction lines and external streamlines in association with a restricted number of singular points (nodes, saddles, and spiral nodes) on the surface and in particular projections of the flow (the crossflow plane, for example) we have a language to classify rationally and unambiguously the 3-D separated flow field about any useful aerodynamic configuration. Sequences of structures of ascending elaboration of nodes, saddles, and spiral nodes can be assembled which are then available to guide experiments when observation is imprecise, or to check the veracity of numerical calculations. We have shown, moreover, that in cross-sectional projections of diverse 3-D separated flows, the mechanisms become familiar, occurring repeatedly from flow to flow. As an approach to design, we may postulate sequences, starting with the simplest number of singular points on the surface and in the flow, for a vehicle at low angle of attack, and increasing in complexity as angle of attack becomes large. The philosophy of design, especially at high angles of attack when the leeward vortical flows have a tendency to become asymmetric, must be one of controlling the locations of the 3-D separations on the vehicle, such as at sharp edges, or by active control from blowing, for example. The design aims, in summary, are that we require steady boundary conditions to provide steady flows, and symmetric boundary conditions to yield symmetric flows. We further demand that as flow regimes change with increasing angle of attack there should be no discontinuous jumps to give uncontrollable forces and moments.

This collection of diverse 3-D separated flows has demonstrated that when a 3-D boundary layer detaches from the surface it will, almost without exception, leave along a swept separation line, rolling up in the process into a well-organized nominally steady vortical motion. The underlying mechanism appears to be independent of both Reynolds number and Mach number, although under laminar conditions the flow features are normally more exaggerated. Hence, the overall details of many flows of practical interest can be determined in a water-tunnel facility in which aircraft and missile designers can make changes to configurations quickly and very cheaply. Some airplane and missile companies are currently doing this.

We deem it useful to end this review by specifying the issues that have been raised, from both experiments and calculations, in the study of singular points. First, there is the question of scale effects. Many large-scale flow phenomena involve a small-scale organized substructure (e.g., arrays of longitudinal vortices on the scale of the thickness of the transitional boundary layer or vortex-shedding on the scale of a shear-layer thickness). In some cases, all or a part of this organized substructure is capable of determining the outcome of the evolution of the large-scale structure; in other cases, it is not. Is it possible, then, to formulate a principle that will distinguish between the vital and the unimportant organized substructures? Can one devise an averaging technique that will preserve the essential structures and smear out the remaining ones? A clarification of these queries should also shed light on similar problems involved in turbulence modeling. The utilization of meshes in finite difference calculations obviously provides a process of averaging, but more work is needed to understand the ramifications of altering mesh intervals, especially insofar as they affect the representation of vital organized substructures. Moreover, we need to incorporate an adequate treatment of the essential singular points in numerical calculation schemes, either by refining the mesh size about the singular points or by including some analytical representation of the flow about the singular points within the numerical scheme.

Second, the rules underlying the placement, number, and types of singular points in terms of the governing flow parameters and body geometry need elaboration. This is particularly true in the nose region where the nature of the origins of lines of separation becomes obscure.

Third, the mechanisms by which stationary flow structures change their topology from one level of complexity to the next (i.e., as they pass through structural instabilities and bifurcations) need to be exposed. For example, studies are needed to provide the links between structural instabilities and bifurcations and the large-scale structural changes in the flow that are characteristic of buffet, stall, and vortex breakdown.

Finally, although we have demonstrated a satisfactory understanding in general of the structures of 3-D separated flows, we are only able to compute them about a limited number of simple aerodynamic components. Numerical techniques invoking either inviscid approximations to model the coiling shear layers, or approximate forms of the Navier-Stokes equations, have been successful and should be encouraged further. But the physics of the turbulence in 3-D separated flow regimes has not yet been investigated to any great extent, and an appeal to well-planned experiments with nonintrusive instrumentation must be made in this regard. To restrict the avenues of possible research, and as a suitable starting point, it might be useful to concentrate on measuring the fluctuating flow quantities in the vicinity of the singular points to determine if there is any identifiable, and perhaps universal, turbulence field associated with each type of singular point.

14. REFERENCES

1. Tobak, M., and Peake, D. J., "Topology of Three-Dimensional Separated Flows." Ann. Rev. Fluid Mech. vol. 14, 1982, pp. 61-85.

2. Peake, D. J., and Owen, F. K., "Control of Forebody Three-Dimensional Flow Separations." AGARD CP-262, May 1979.

3. Hsieh, T., "An Investigation of Separated Flows About a Hemisphere-Cylinder at Incidence in the Mach Number Range from 0.6 to 1.5." AIAA Paper 77-179, Jan. 1977.

4. Hsieh, T., and Wang, K. C., "Concentrated Vortex on the Nose of an Inclined Body of Revolution." AIAA J., vol. 14, no. 5, 1976, pp. 698-700.

5. Hsieh. T., "Calculating Viscous, Sonic Flow Over Hemisphere-Cylinder at 19-Degree Incidence: The Capturing of Nose Vortices." AIAA Paper 81-0189, 1981.

6. Pulliam, T. H., and Steger, J. L., "On Implicit Finite-Difference Simulations of Three-Dimensional Flow." AIAA Paper 78-10, Jan. 1978.

7. Peake, D. J., and Tobak, M., "Three-Dimensional Interactions and Vortical Flows with Emphasis on High Speeds." AGARDograph 252, July 1980.

8. Tobak, M., and Peake, D. J., "Topological Structures of Three-Dimensional Separated Flow." AIAA Paper 81-1260, June 1981.

9. Jorgensen, L. H., "Prediction of Aerodynamic Characteristics for Slender Bodies Alone and with Lifting Surfaces to High Angles of Attack." AGARD CP-247, Oct. 1978.

10. Legendre, R., "Séparation de l'Écoulement Laminaire Tridimensionnel." La Recherche Aeronautique no. 54, Nov.-Dec. 1956, pp. 3-8.

11. Wickens, R. H., "The Vortex Wake and Aerodynamic Load Distribution of Slender Rectangular Plates (The Effects of a 20-Degree Bend at Mid-Chord)." National Research Council of Canada Aero Report LR-458, July 1966.

12. Lighthill, M. J., "Attachment and Separation in Three-Dimensional Flow." Laminar Boundary Layers, Sec. II 2.6, L. Rosenhead, ed., Oxford U. Press, 1963, pp. 72-82.

13. Winkelmann, A. E., and Barlow, J. B., "Flowfield Model for a Rectangular Planform Wing Beyond Stall." AIAA J., vol. 18, no. 8, 1980, pp. 1006-1008.

14. Monnerie, B., and Werlé, H., "Étude de l'Écoulement Supersonique et Hypersonique autour d'une Aile Élancée en Incidence." AGARD CP-30, May 1968.

15. Maltby, R. L., "Flow Visualization in Wind Tunnels Using Indicators." AGARDograph 70, Apr. 1962.

16. Legendre, R, "La Condition de Joukowski en Écoulement Tridimensionnel. Rech. Aérosp., no. 5, 1972.

17. Legendre, R., "Lignes de Courant d'un Écoulement Continu," Rech. Aérosp. no. 105, 1965, pp. 3-9.

18. Küchemann, D., "On the Possibility of Designing Wings that Combine Vortex Flows with Classical Aerofoil Flows." Unpublished RAE Tech. Memorandum, 1971.

19. Moss, G. F., "Some UK Research Studies of the Use of Wing-Body Strakes on Combat Aircraft Configurations at High Angles of Attack." AGARD CP-247, Oct. 1978.

20. Rainbird, W. J., "The External Flow Field About Yawed Circular Cones." AGARD CP-30, May 1968.

21. Rainbird, W. J., "Turbulent Boundary-Layer Growth and Separation on a Yawed 12-1/2° Cone at Mach Numbers 1.8 and 4.25." AIAA J., vol. 6, no. 12, Dec. 1968, pp. 2410-2416.

22. Nebbeling, C., and Bannink, W. J., "Experimental Investigation of the Supersonic Flow Field About a Slender Cone at High Incidences." Rept. LR-233, Delft Univ. Technology, Dept. of Aerosp. Eng., The Netherlands, Nov. 1976.

23. Peake, D. J., Fisher, D. F., McRae, D. S., "Flight Experiments with a Slender Cone at Angle of Attack." AIAA Paper 81-0337, Jan. 1981.

24. McRae, D. S., Peake, D. J., and Fisher, D. F., "A Computational and Experimental Study of High Reynolds Number Viscous/Inviscid Interaction About a Cone at High Angle of Attack." AIAA Paper 80-1422, July 1980.

25. Nituch, M. J., "The Use of Congruent Obstacle Blocks for the Indirect Measurement of Turbulent Skin Friction on Smooth Surfaces." Thesis, Carleton U., Ottawa, Aug. 1972.

26. Peake, D. J., "Three-Dimensional Swept Shock/Turbulent Boundary Layer Separations with Control by Air Injection." Ph.D. Thesis, Carleton U., Ottawa, 1975; also National Research Council of Canada Aero. Report LR-592, July 1976.

27. Elfstrom, G. M., "Indirect Measurement of Turbulent Skin-Friction. DME/NAE Quarterly Bulletin, no. 1, National Research Council of Canada, 1979, pp. 21-51.

28. Dougherty, N. S., and Fisher, D. F., "Boundary-Layer Transition on a 10-Degree Cone: Wind-Tunnel/ Flight Data Correlation." AIAA Paper 80-0154, Jan. 1980.

29. Bradshaw, P., and Unsworth, K., "A Note on Preston Tube Calibrations in Compressible Flow." IC-Aero-73-07, Imperial College of Science and Technology, London, England, Sept. 1973.

30. Peake, D. J., Owen, F. K., and Johnson, D. A., "Control of Forebody Vortex Orientation to Alleviate Side Forces," AIAA Paper 80-0183, Jan. 1980.

31. Peake, D. J., Owen, F. K., and Higuchi, H., "Symmetrical and Asymmetrical Separations About a Yawed Cone." AGARD CP-247, Oct. 1978.

32. Fiechter, M., "Uber Wirbelsysteme an schlanken Rotationskorpern und ihren Einfluss auf die aerodynamischen Beiwerte." Deutsch-Franzosisches Forschungs-Institut Saint-Louis," Report 10/66, 1966.

33. Werlé, H., "La Tunnel Hydrodynamique au Service de la Recherche Aérospatiale." ONERA Publication No. 156, 1974.

34. O'Hare, J., and Jones, J., "Flow Visualization Photography of a Yawed Tangent Ogive Cylinder at Mach 2." AEDC-TR-73-45, 1973.

35. Grosche, F. R., "Wind Tunnel Investigation of the Vortex System Near an Inclined Body of Revolution with and without Wings." AGARD CP-71, Sept. 1970.

36. Boersen, S., "Reynolds Number Effects on Pressure and Normal Force Distributions Along a Conically Pointed Circular Cylinder at Mach Number of 2.3." NLR TR 75124U, Sept. 1975.

37. Jernell, L. S., "Aerodynamic Characteristics of Bodies of Revolution at Mach Numbers from 1.50 to 2.86 and Angles of Attack to 180°." NASA TM X-1658, 1968.

38. Jorgensen, L. H., and Nelson, E. R., "Experimental Aerodynamic Characteristics for a Cylindrical Body of Revolution with Various Noses at Angles of Attack from 0° to 58° and Mach Numbers from 0.6 to 2.0." NASA TM X-3128, 1974.

39. Jorgensen, L. H., and Nelson, E. R., "Experimental Aerodynamic Characteristics for Bodies of Elliptical Cross-Section at Angles of Attack from 0° to 58° and Mach Numbers from 0.6 to 2.0." NASA TM X-3129, 1975.

40. Jorgensen, L. H., "Prediction of Static Aerodynamic Characteristics for Slender Bodies Alone and with Lifting Surfaces to Very High Angles of Attack." NASA TR R-474, 1977.

41. Küchemann, D., "The Aerodynamic Design of Aircraft — An Introduction. Part 3." RAE Tech. Memo. Aero 1535, Aug. 1973; also Pergamon Press, 1978.

42. Peake, D. J., Rainbird, W. J., and Atraghji, E. G., "Three-Dimensional Separations on Aircraft and Missiles." AIAA J., vol. 10, no. 5, May 1972, pp. 567-580.

43. Atraghji, E. G., "The Influence of Mach Number, Reynolds Number, Semi-Nose Angle and Roll Rate on the Development of the Forces and Moments Over a Series of Long Slender Bodies of Revolution at Incidence." National Research Council of Canada, NAE 5 x 5/0020, Mar. 1967.

44. Atraghji, E. G., "Pressure Distribution Over a Family of Inclined Long Slender Bodies of Revolution at M_∞ = 0.5, 2.0 and 3.5." National Research Council of Canada, NAE 4 x 5/0029, Aug. 1968.

45. Ward, G. N., "Linearised Theory of High Speed Flow," Chap. 9. Cambridge U. Press, England, 1955.

46. Hoak, D. E., "Body Lift in the Non-Linear Angle-of-Attack Range." Sec. 4.2.12, USAF Stability and Control Datcom, Flight Control Div., Air Force Flight Dynamics Lab., Wright-Patterson Air Force Base, Ohio, Oct. 1960 (revised, Nov. 1965).

47. Öhman, L. H., "A Surface Flow Solution and Stability Derivatives for Bodies of Revolution in Complex Supersonic Flow." Parts I and II, National Research Council of Canada Aero. Reports LR-419, 519, Nov. and Dec. 1964.

48. Lamont, P. J., "Pressure Measurements on an Ogive-Cylinder at High Angles of Attack with Laminar, Transition or Turbulent Separation." AIAA Paper 80-1556-CP, Aug. 1980.

49. Lamont, P. J., "The Complex Asymmetric Flow Over a 3.5D Ogive Nose and Cylindrical Afterbody at High Angles of Attack." AIAA Paper 82-0053, Jan. 1982.

50. Rainbird, W. J., Crabbe, R. S., Peake, D. J., and Meyer, R. F., "Some Examples of Separation in Three-Dimensional Flows." CASI J., vol. 12, no. 10, Dec. 1966, pp. 409-423.

51. Bannink, W. J., and Nebbeling, C., "Measurements of the Supersonic Flow Field Past a Slender Cone at High Angles of Attack." AGARD CP-247, Oct. 1978.

52. Keener, E. R., and Chapman, G. T., "Similarity in Vortex Asymmetries Over Slender Bodies and Wings." AIAA J., vol. 15, no. 9, Sept. 1977, pp. 1370-1372.

53. Shanks, R. E., "Low Subsonic Measurements of Static and Dynamic Stability Derivatives of Six Flat Plate Wings Having Leading-Edge Sweep Angles of 70° to 84°." NASA TN D-1822, 1963.

54. Fellows, K. A., and Carter, E. C., "Results and Analysis of Pressure Measurements on Two Isolated Slender Wings and Slender Wing-Body Combinations at Supersonic Speeds. Vol. 1, Analysis." ARA Report 12, Nov. 1969.

55. Keener, E. R., and Chapman, G. T., "Onset of Aerodynamic Side Forces at Zero Sideslip on Symmetric Forebodies at High Angles of Attack." AIAA Paper 74-770, Aug. 1974.

56. Keener, E. R., Chapman, G. T., and Kruse, R. L., "Effects of Mach Number and Afterbody Length on Onset of Asymmetric Forces on Bodies at Zero Sideslip and High Angles of Attack." AIAA Paper 76-66, Jan. 1976.

57. Nielsen, J. N., "Non-Linearities in Missile Aerodynamics." AIAA Paper 78-20, Jan. 1978.

58. Allen, H. J., and Perkins, E. W., "A Study of Effects of Viscosity on Flow Over Slender Inclined Bodies of Revolution." NACA Report 1048, 1951.

59. Deffenbaugh, F. D., and Koerner, W. G., "Asymmetric Vortex Wake Development on Missiles at High Angles of Attack." J. Spacecraft & Rockets, vol. 14, no. 3, Mar. 1977, pp. 155-162.

60. Tobak, M., and Peake, D. J., "Topology of Two-Dimensional and Three-Dimensional Separated Flows." AIAA Paper 79-1480, July 1979.

61. Küchemann, D., and Weber, J., "Vortex Motions." ZAMM, vol. 7, no. 8, 1965, pp. 457-474.

62. Tinling, B. E., and Allen, C. Q., "An Investigation of the Normal Force and Vortex-Wake Characteristics of an Ogive-Cylinder-Body at Subsonic Speeds." NASA TN D-1297, 1962.

63. Thomson, K. D., and Morrison, D. F., "The Spacing Position and Strength of Vortices in the Wake of Slender Cylindrical Bodies at Large Incidences." J. Fluid Mech., vol. 50, pt. 4, 1971, pp. 751-783.

64. Hasel, L. E., and Kouyoumjian, W. L., "Investigation of Static Pressures and Boundary-Layer Characteristics on the Forward Parts of Nine Fuselages of Various Cross-Sectional Shapes at M_∞ = 2.01." NACA RM-L56I13, Jan. 1957.

65. Clarkson, M. H., Malcolm, G. N., and Brittain, V. A., "Aerodynamic Characteristics of Bodies with Non-Circular Cross Sections at High Angles of Attack." To appear as AIAA Paper 82-0056, 1982.

66. Faro, I.D.V., "Supersonic Inlets." AGARDograph 102, May 1965, pp. 121-123.

67. Culley, M., "A Side-Mounted Supersonic Intake and the Problem of Three-Dimensional Boundary-Layer Separation." ARL ME 137, Australia, June 1972.

68. Culley, M., "Viscous Interaction in Integrated Supersonic Intakes." First International Symposium on Air Breathing Engines, Marseilles, France, June 1972.

69. Peake, D. J., Jones, D. J., and Rainbird, W. J., "The Half-Cone Flow and its Significance to Side-Mounted Intakes." AGARD CP-71, Sept. 1970.

70. Culley, M., "A Brief Examination of the Flow External to an F-111 Intake at Mach 1.6." ARL/ME 357, Australia, July 1975.

71. Swan, W. C., "A Discussion of Selected Aerodynamic Problems on Integration of Propulsion Systems with the Airframe of Transport Aircraft." AGARDograph 103, Pt. I, Oct. 1965, pp. 23-68.

72. Sigalla, A., and Hallstaff, T. H., "Aerodynamics of Powerplant Installation on Supersonic Aircraft." J. Aircraft, vol. 4, no. 4, July-Aug. 1967, pp. 273-277.

73. Peake, D. J., and Rainbird, W. J., "The Drag Resulting from Three-Dimensional Separations Caused by Boundary-Layer Diverters and Nacelles in Subsonic and Supersonic Flow." AGARD CP-124, Apr. 1973.

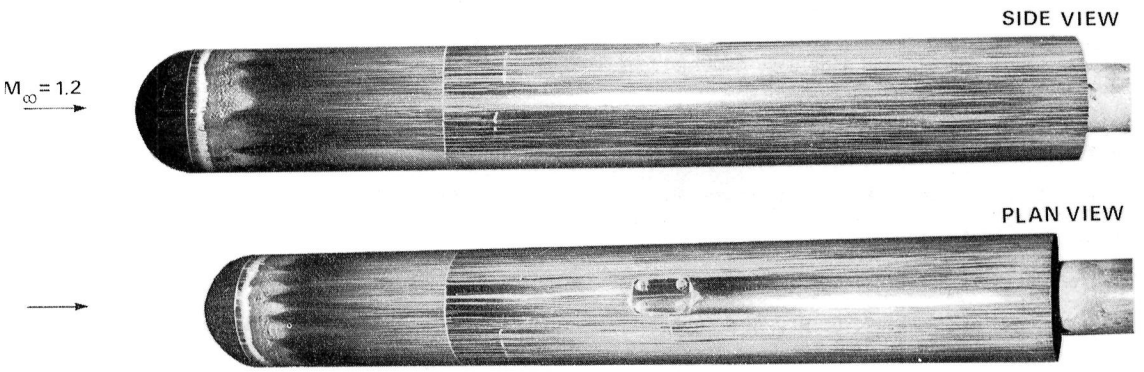

(a) $\alpha = 0°$.

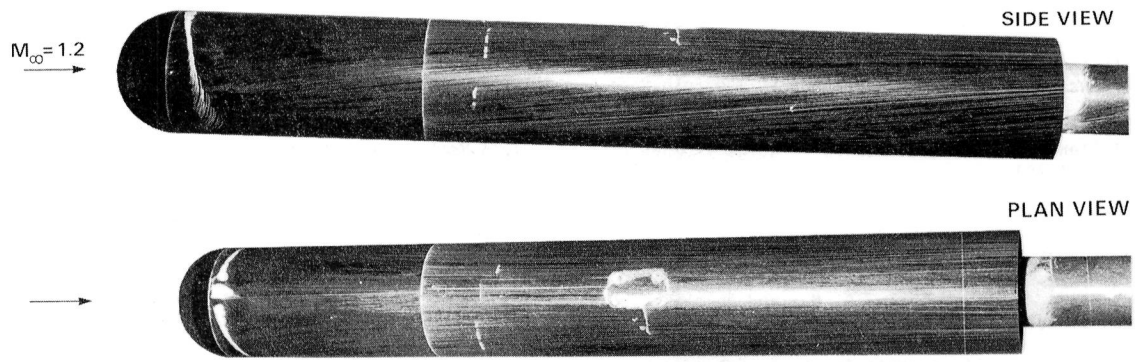

(b) $\alpha = 3.5°$.

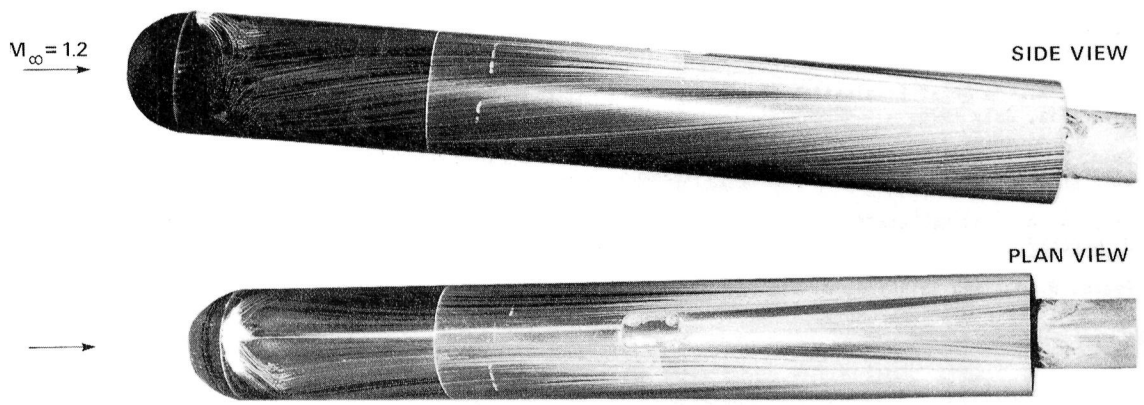

(c) $\alpha = 5.0°$.

Fig. 1. Oil-streak patterns about a hemisphere-cylinder at angle of attack at $M_\infty = 1.2$, $R_{L_\infty} = 4.9 \times 10^6$, L = 7.5D, D = 2.6 in.

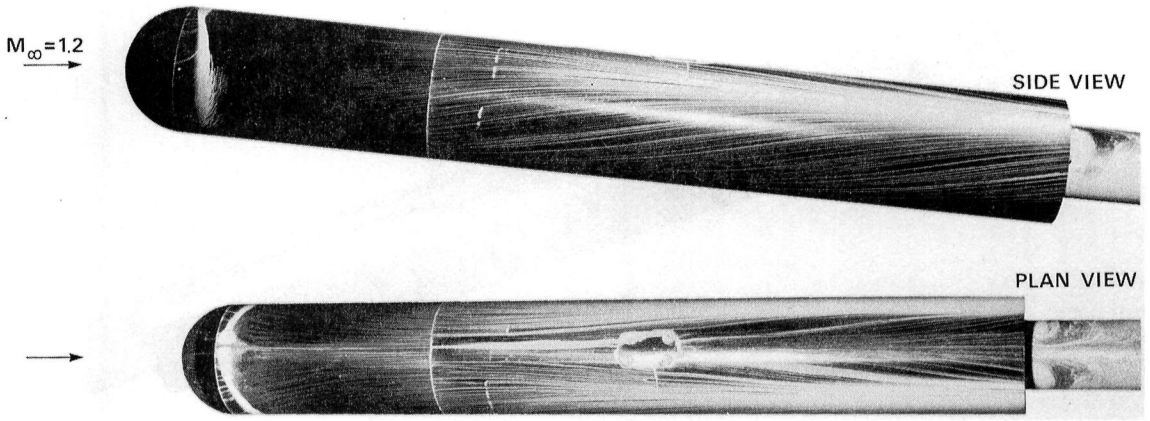

(d) α = 6.5°.

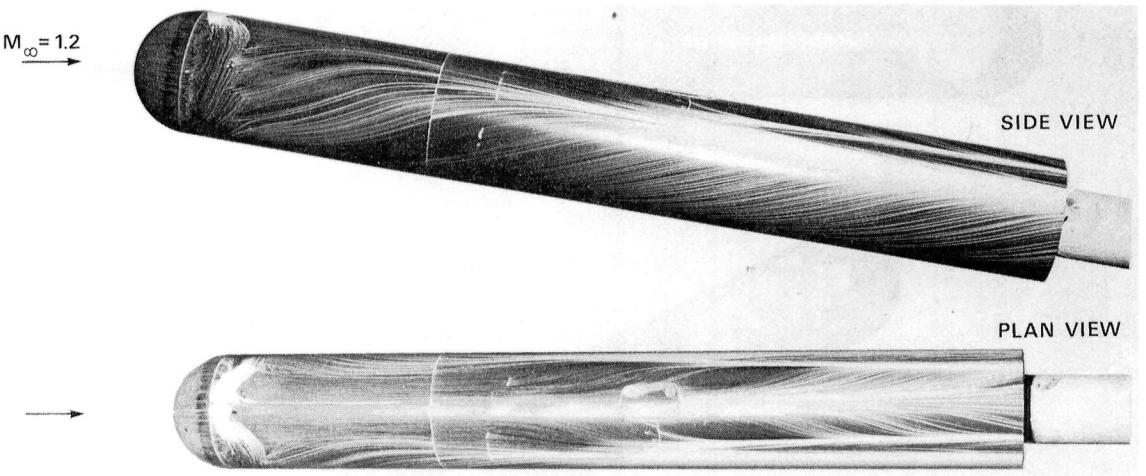

(e) α = 10.0°.

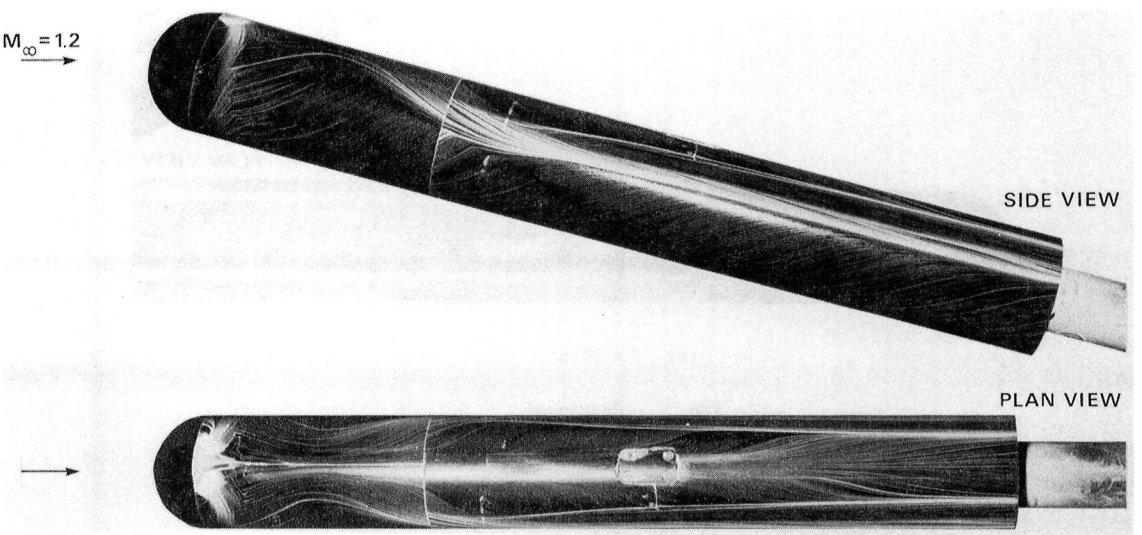

(f) α = 15°.

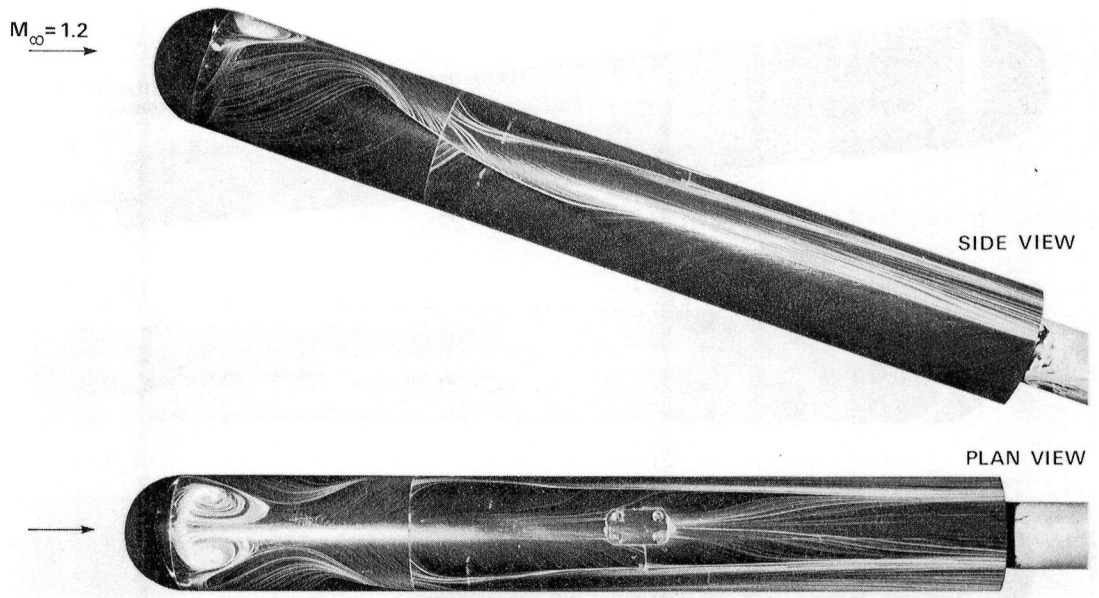

(g) α = 19.0°.

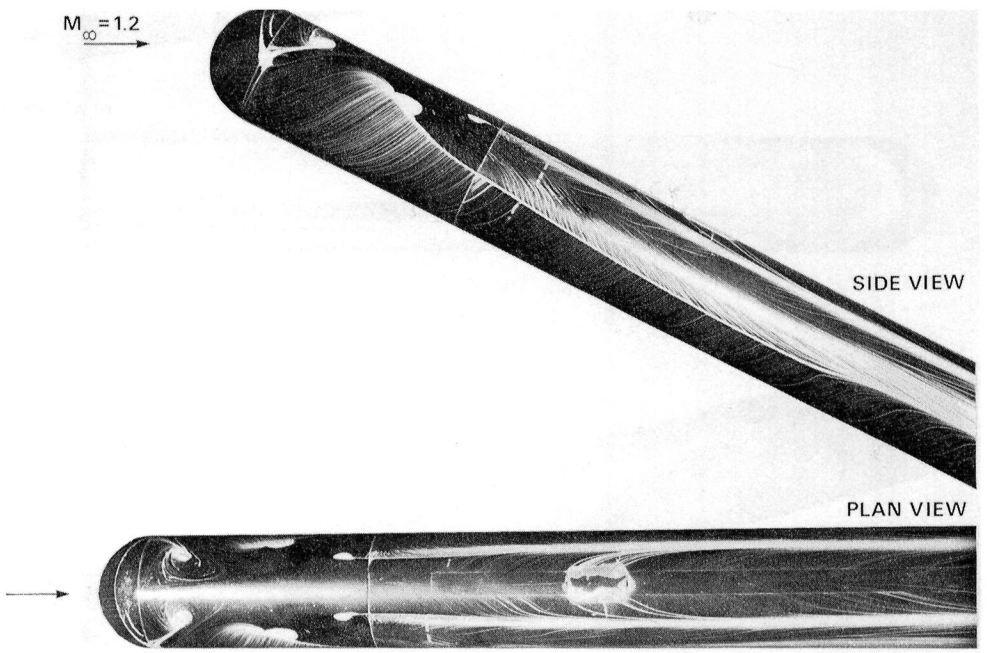

(h) α = 27.5°.

Fig. 1. Continued.

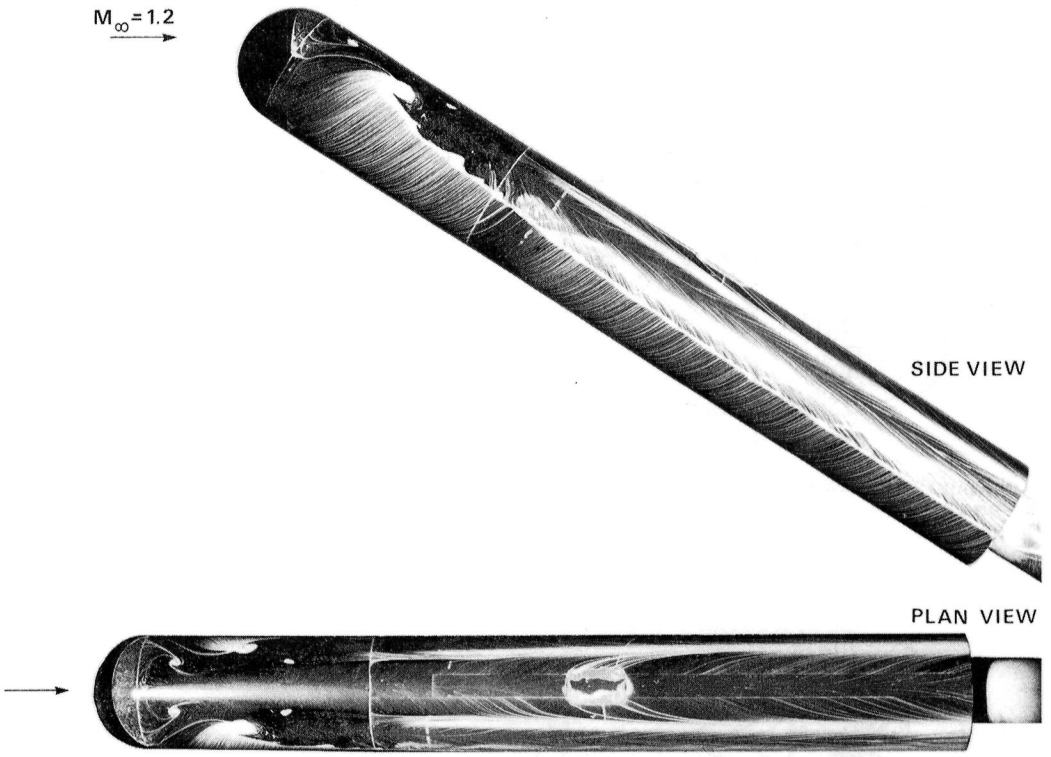

(i) $\alpha = 32.5°$.

Fig. 1. Concluded.

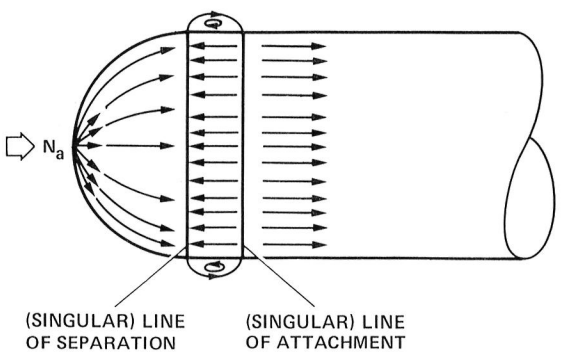

(a) $\alpha = 0°$.

Fig. 2. Conceptual sketches of skin-friction line patterns about a hemisphere-cylinder at angle of attack (drawn from Fig. 1).

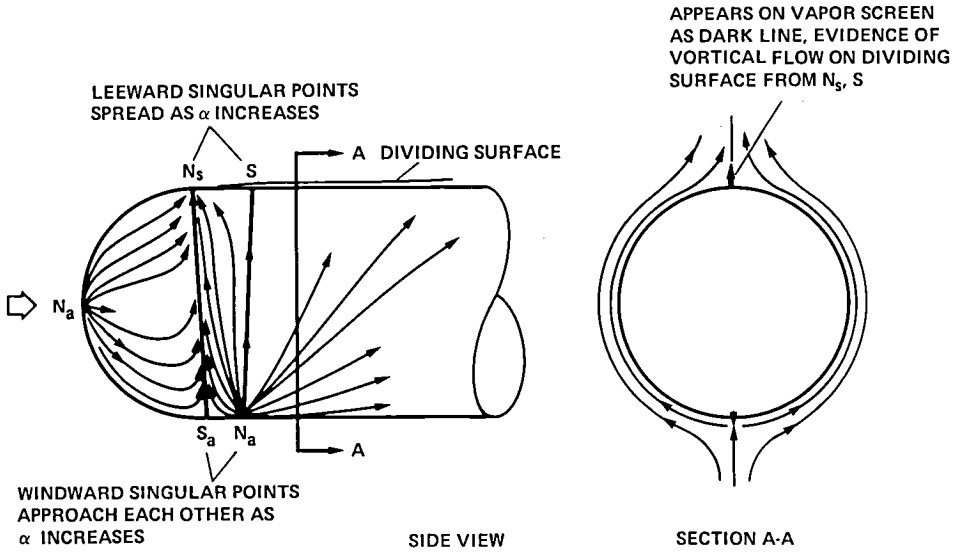

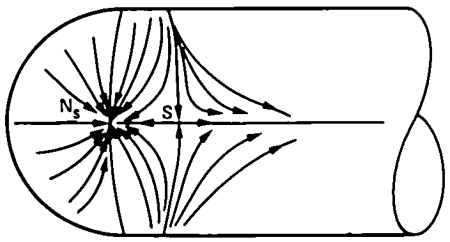

(b) $\alpha = 1°$.

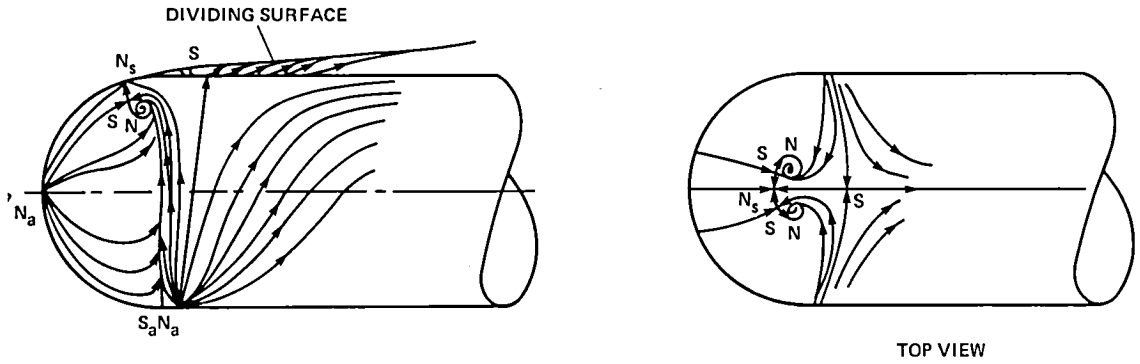

(c) $\alpha = 3.5°$.

Fig. 2. Continued.

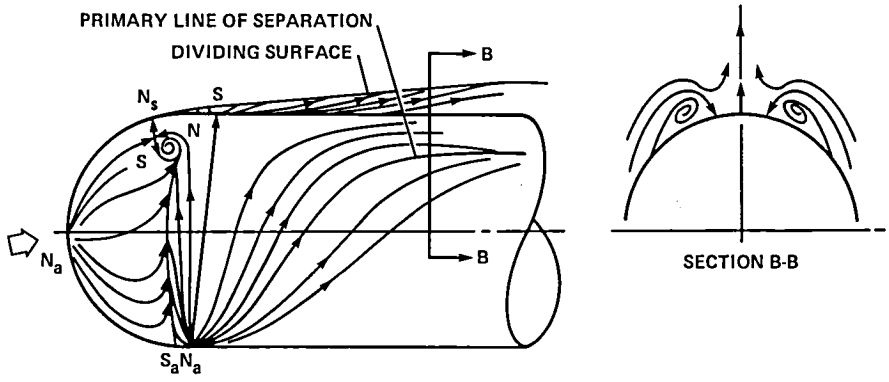

(d) α = 5.0°.

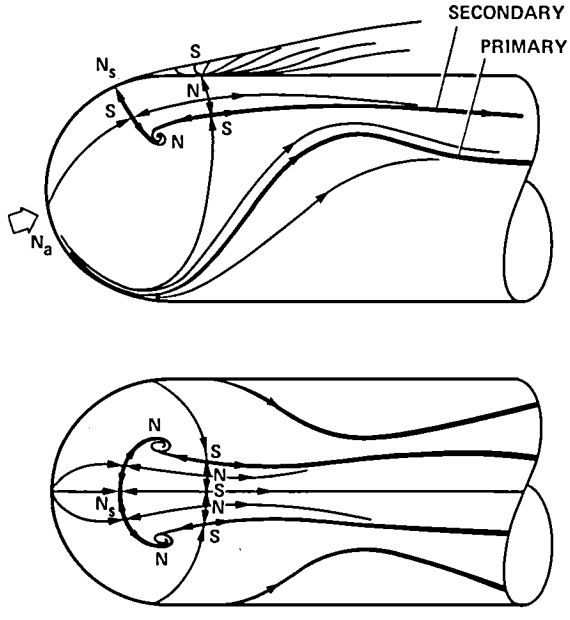

(PRIMARY OUT OF N_a, SECONDARY FROM SADDLE POINT)

(e) α = 10.0°, 15.0°.

Fig. 2. Continued.

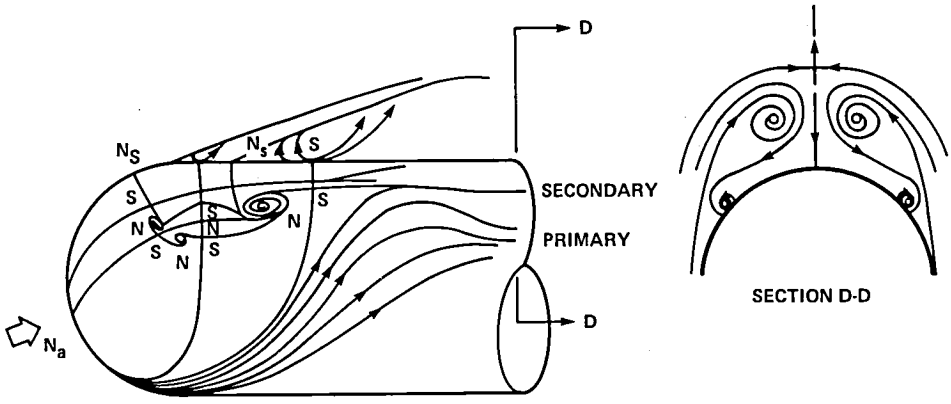

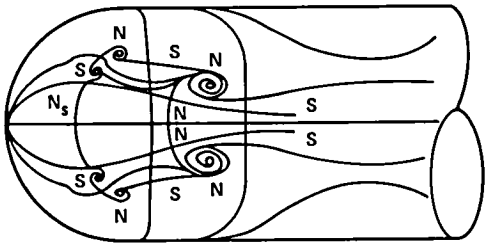

(PRIMARY OUT OF N_a, SECONDARY FROM SECOND OF A PAIR OF SPIRAL NODES)

(f) $\alpha = 19.0°$.

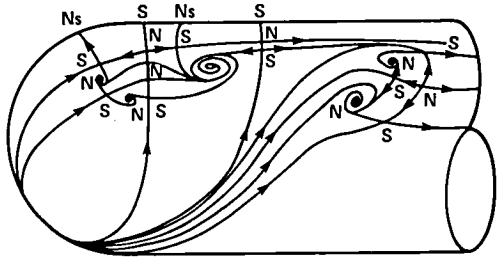

(g) $\alpha = 27.5°$.

Fig. 2. Concluded.

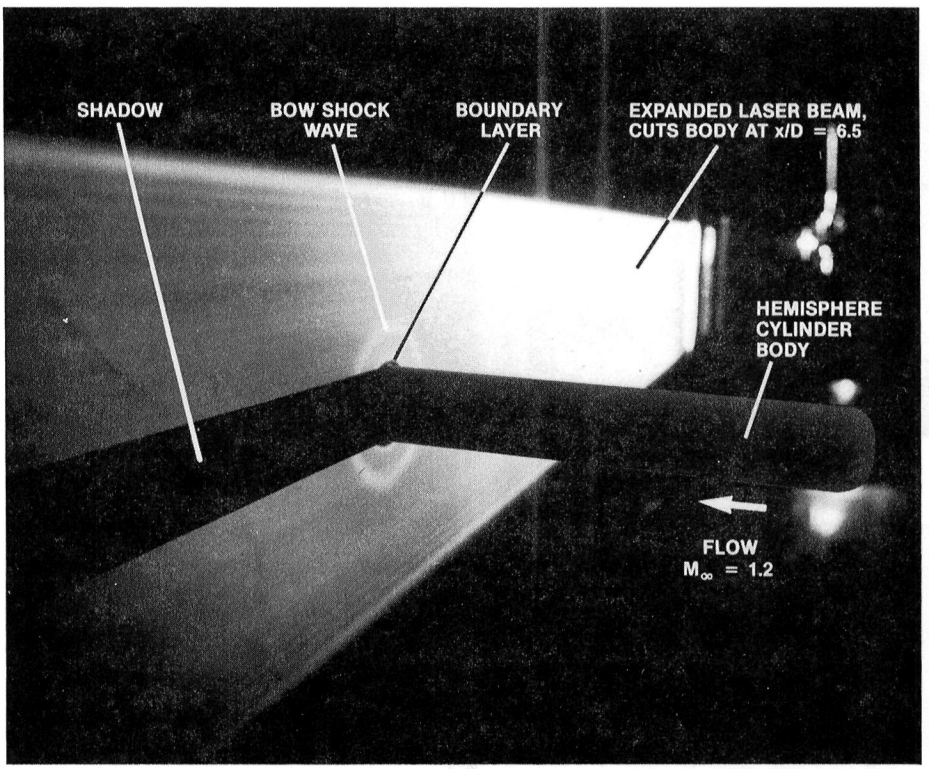

Fig. 3. Axisymmetric crossflow vapor screen at x/D = 6.5 along hemisphere-cylinder at M_∞ = 1.2, R_{L_∞} = 4.9 × 10^6, L = 7.5D, D = 2.6 in.

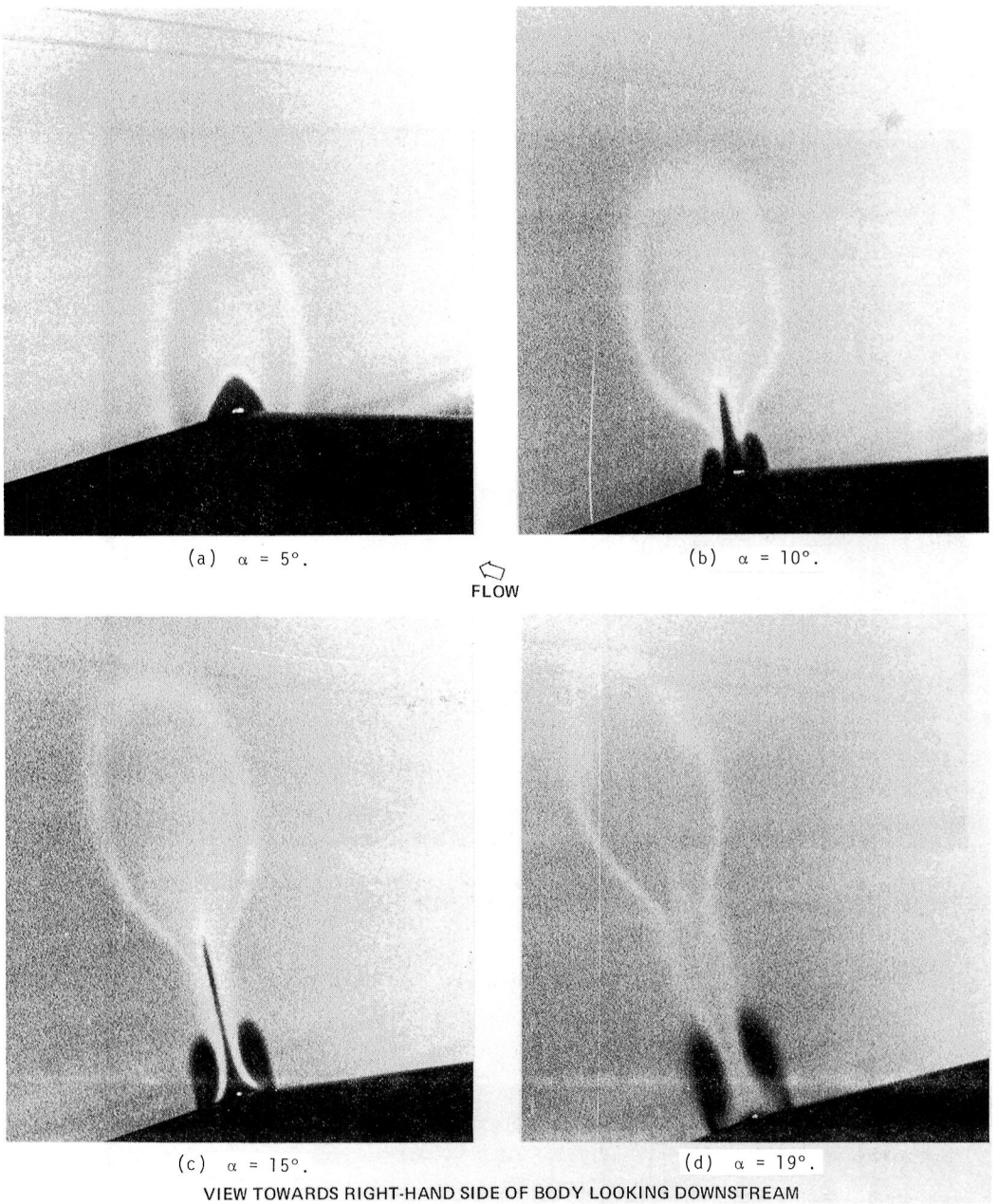

Fig. 4. Crossflow vapor screens at x/D = 6.5 along hemisphere-cylinder at $M_\infty = 1.2$, $R_{L_\infty} = 4.9 \times 10^6$, L = 7.5D, D = 2.6 in.

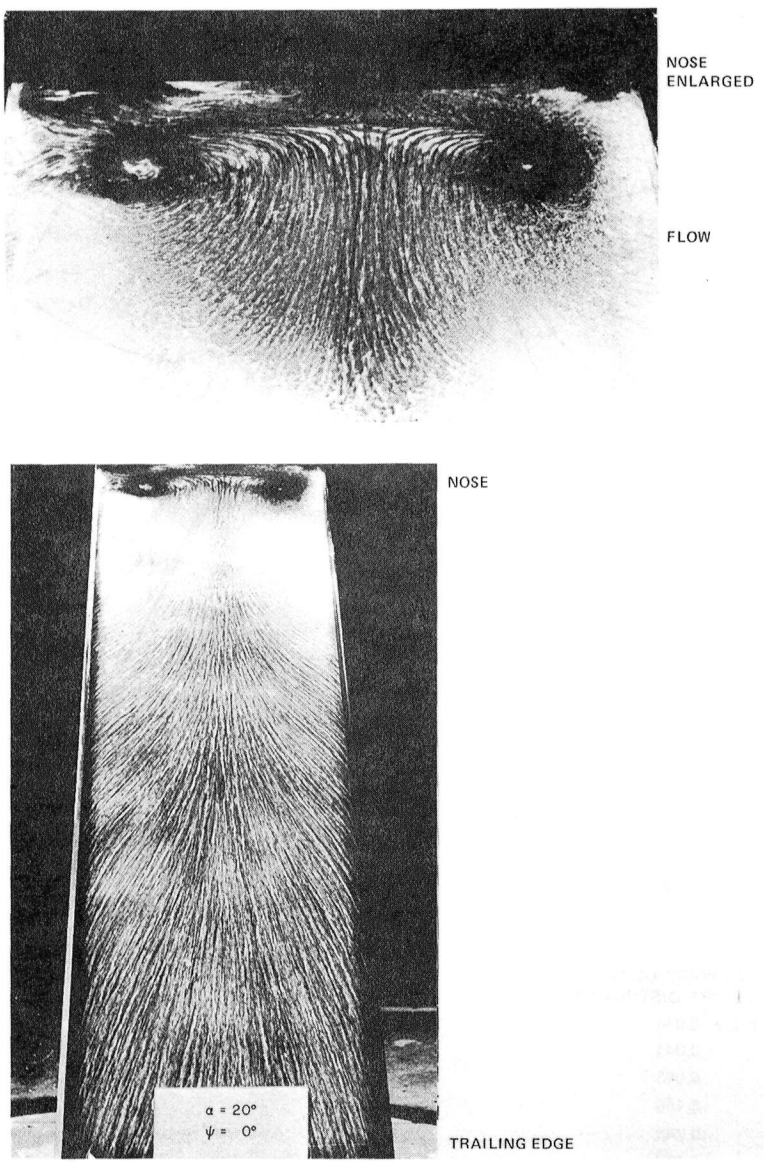

Fig. 5. Oil-flow pattern on slender, rectangular wing at $\alpha = 20°$ (Ref. 11).

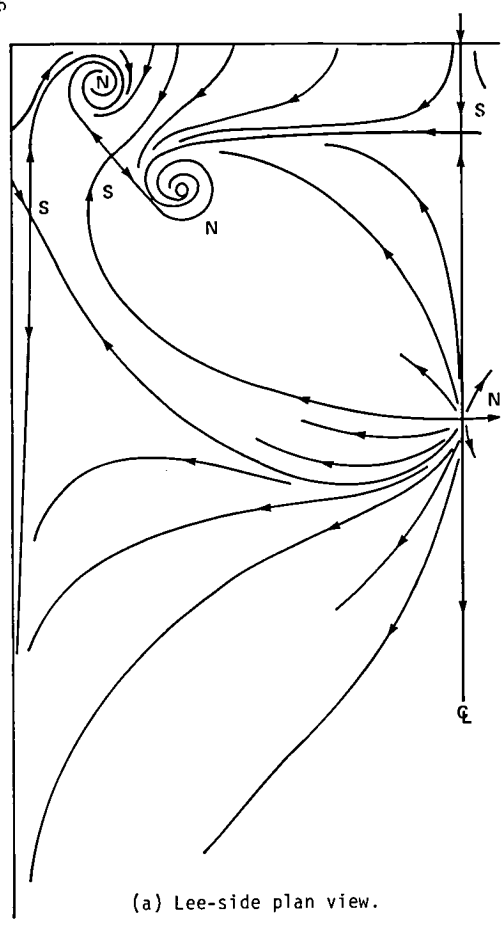

(a) Lee-side plan view.

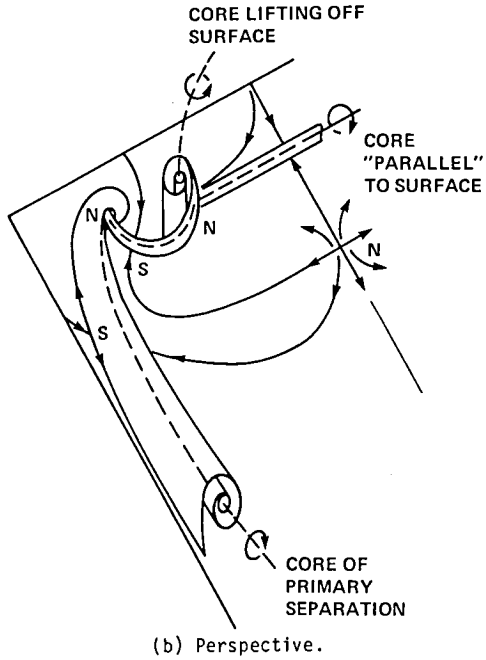

(b) Perspective.

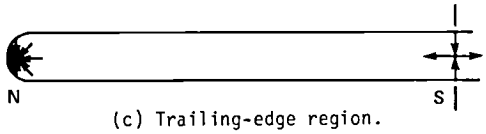

(c) Trailing-edge region.

NOTE: THERE WILL BE 1 NODE OF ATTACHMENT ON UNDERSIDE ℄

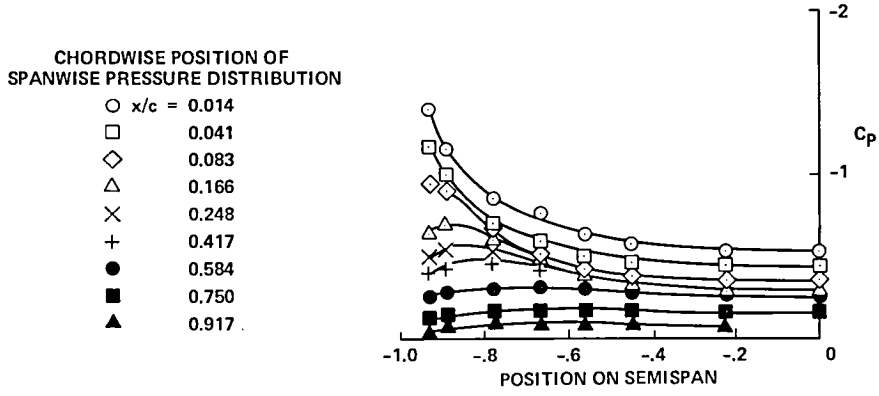

(d) Spanwise pressure distributions on topside.

Fig. 6. Interpretation of skin-friction lines and pressures on slender, rectangular wing, aspect ratio 0.25, at α = 20° in low-speed flow (Ref. 11).

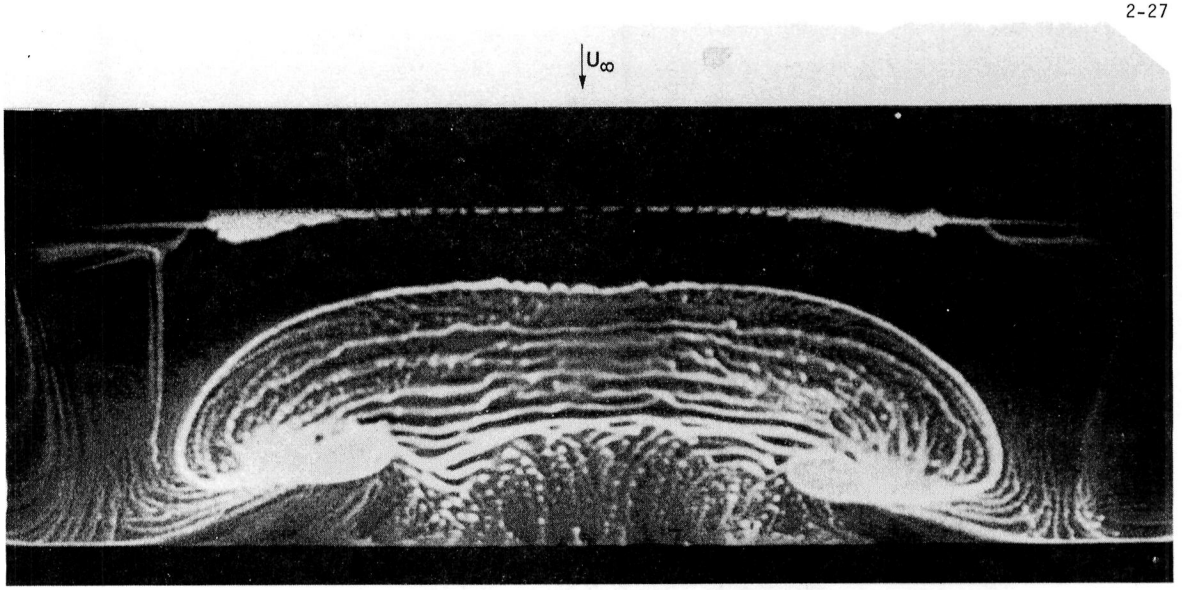

(a) Oil flow on Clark Y airfoil: c = 3.5 in., s = 12.25 in., $R_c = 2.5 \times 10^5$.

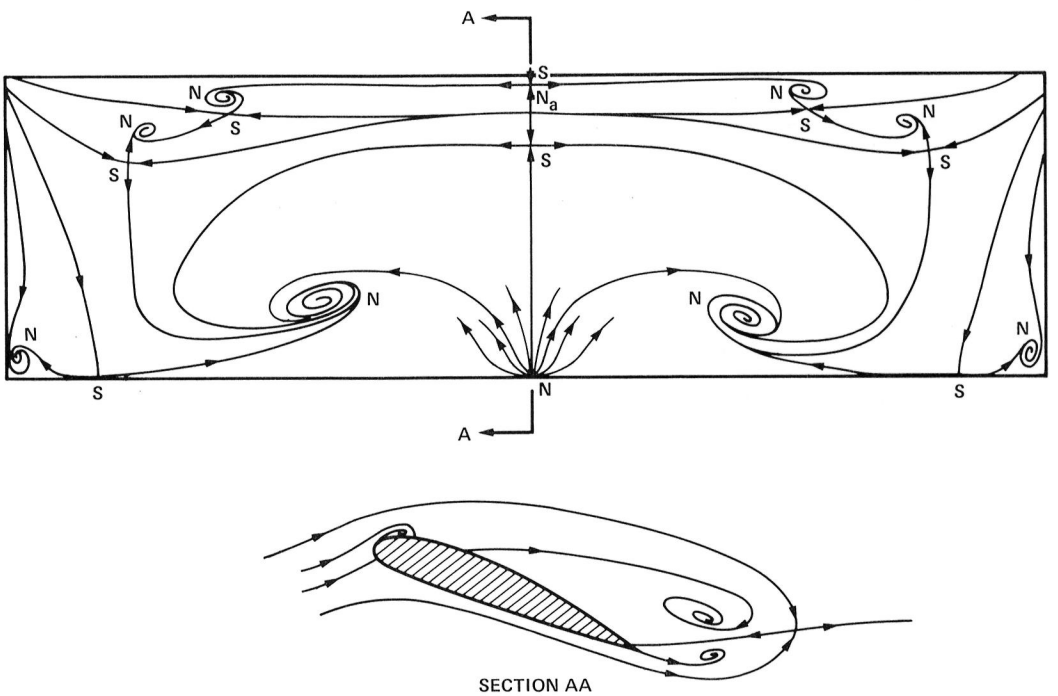

(b) Conjectured pattern of skin-friction lines.

Fig. 7. Rectangular wing, aspect ratio 3.5, at $\alpha = 20°$ in low-speed flow (Ref. 13).

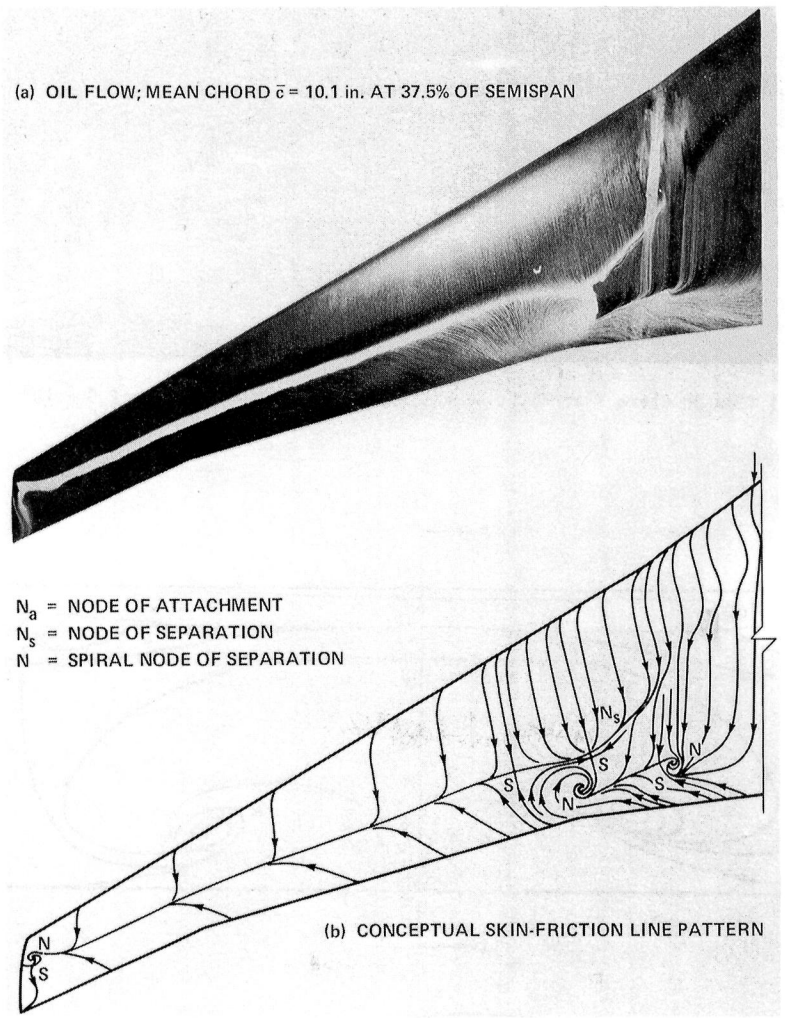

Fig. 8. Early transport swept-wing design close to buffet onset conditions: $M_\infty = 0.82$, $R_{\bar{c}} = 2.5 \times 10^6$.

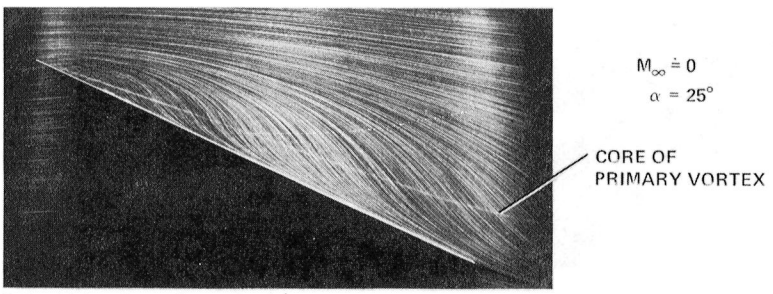

(a) Side elevation.

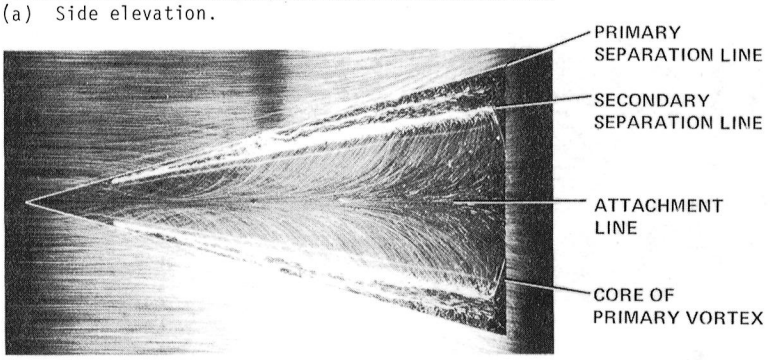

(b) Plan view.

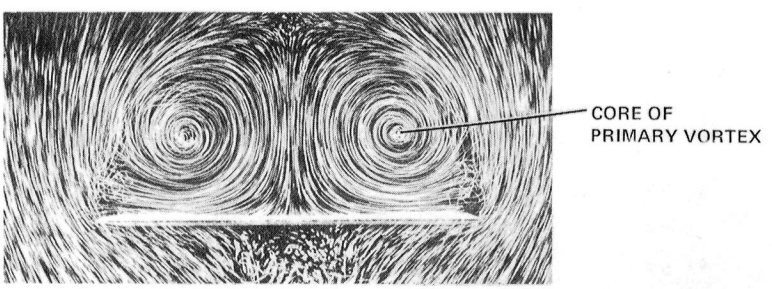

(c) Cross flow.

Fig. 9. Very low-speed 75° delta wing flow of Monnerie and Werlè (Ref. 14).

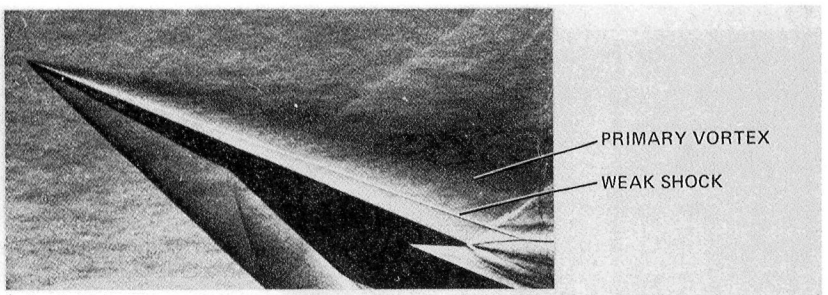

(a) Schlieren

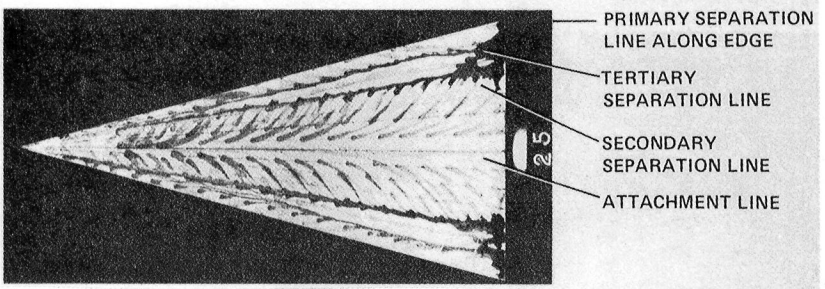

(b) Lee-side pattern of skin-friction lines.

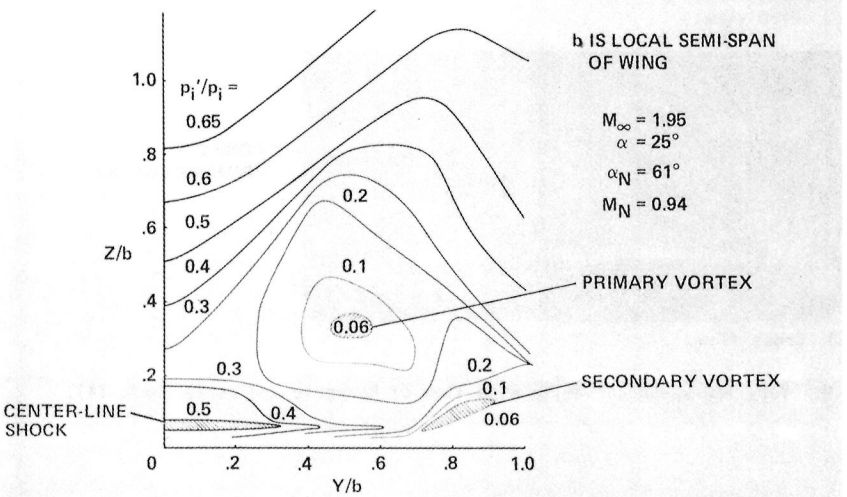

(c) Contours of constant pitot pressure.

Fig. 10. Seventy-five-degree delta wing flow of Monnerie and Werlè (Ref. 14) with subsonic leading edges.

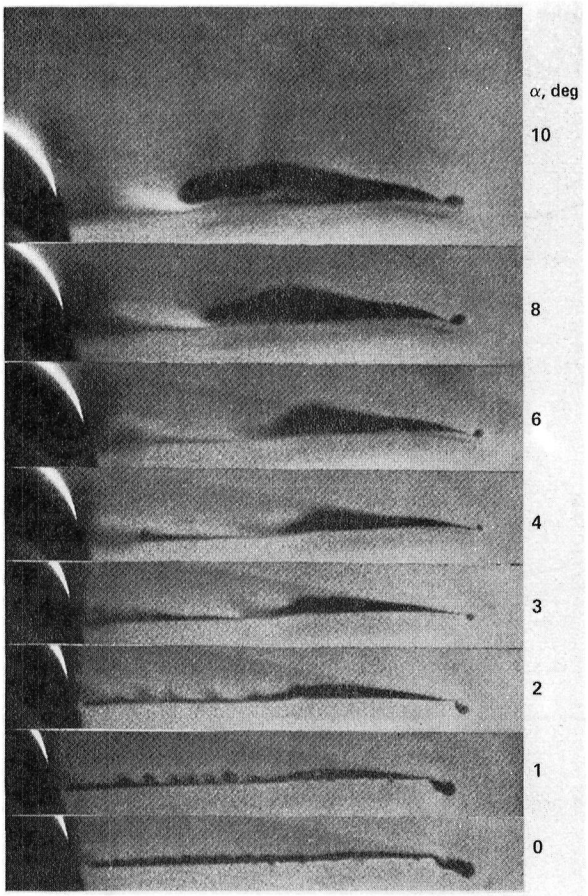

Fig. 11. Vapor-screen photographs of flow behind cambered delta wing at M_∞ = 1.88 (Maltby, Ref. 15).

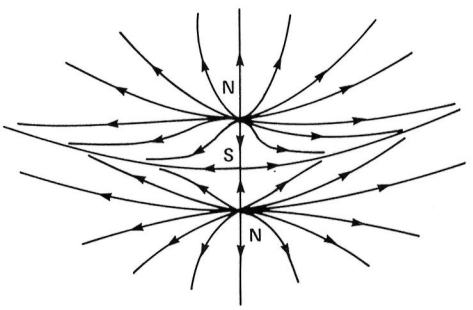

LIGHTHILL 1963

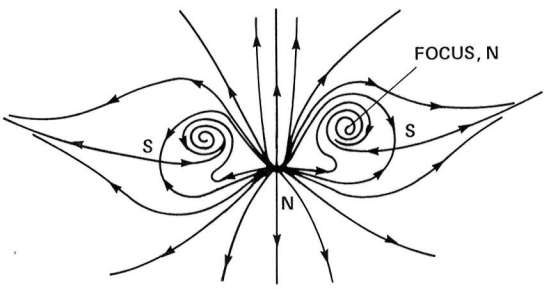

LEGENDRE 1972

Fig. 12. Postulated patterns of skin-friction lines at rounded apex of delta wing.

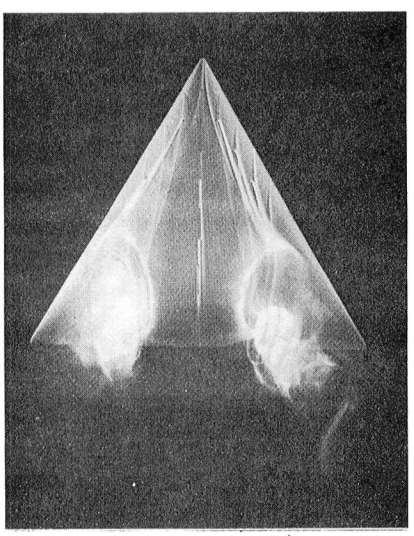

IN WATER TUNNEL (WERLÉ 1974)

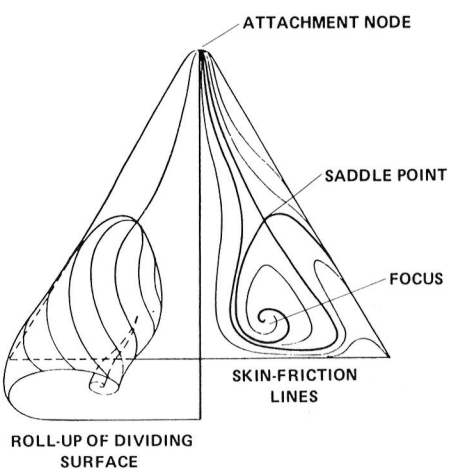

POSTULATED PATTERNS OF LEGENDRE 1965

Fig. 13. Laminar flow on slender delta wing at high angle of attack (Legendre, Ref. 17).

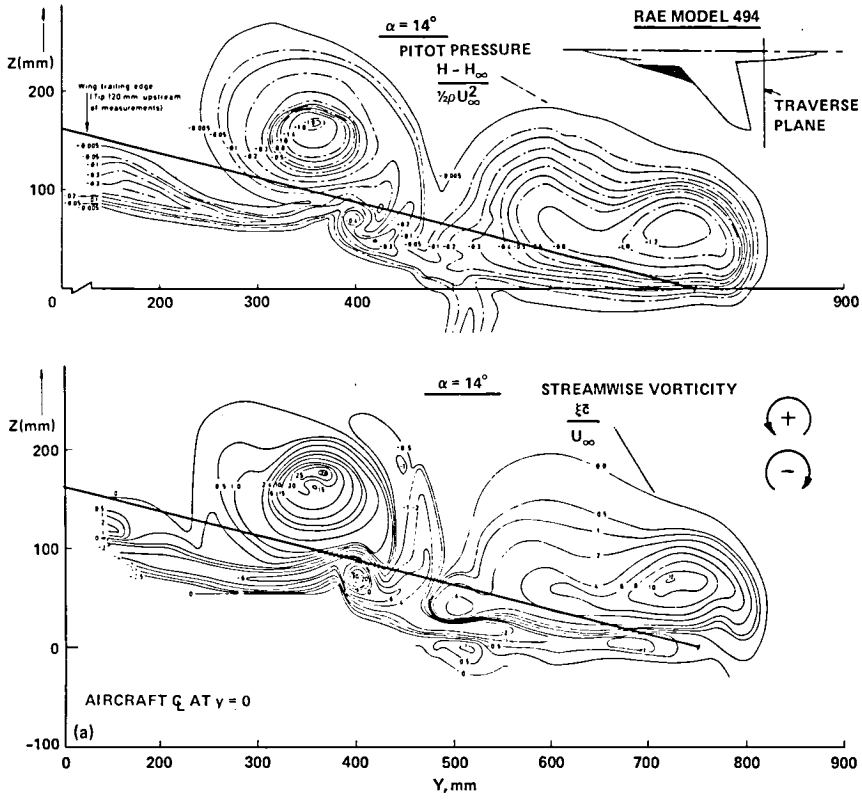

(a) Contours of constant pitot pressure and vorticity.

NOTE: TOPOLOGY LAW IS $\Sigma_N - \Sigma_S = 2$
ASSUMING NODES OF ATTACHMENT AND SEPARATION AT THE NOSE AND TAIL, FOR BOTH L.H. AND R. H. SIDES, $\Sigma_N = 2 \times 8 + 2 = 18$, $\Sigma_S = 2 \times 8 = 16$ $\Big\}$ $\therefore \Sigma = 2$

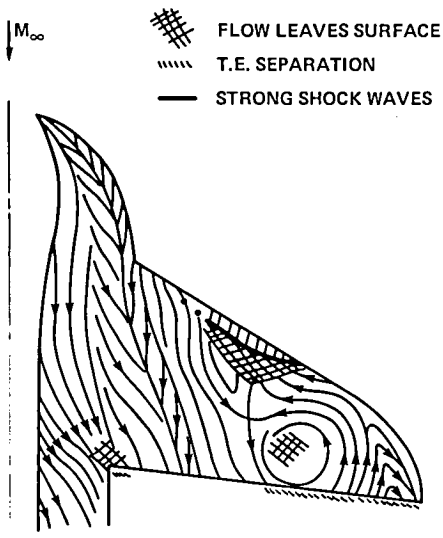

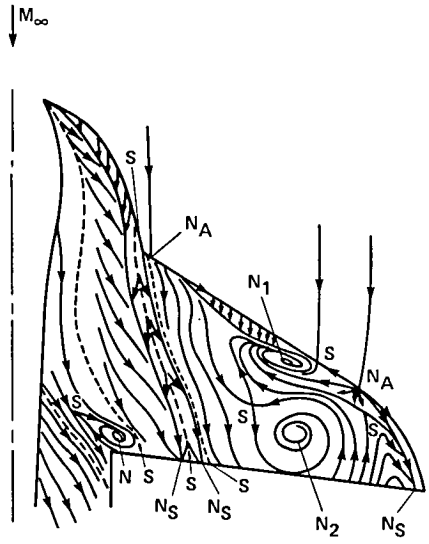

NOTE: TOPOLOGY LAW IS $\Sigma_N - (\Sigma_S + \frac{1}{2}\Sigma_{S'}) = -1$ FOR STREAMLINES IN A 2-D PLANE CUTTING A 3-D BODY

HERE, FOR L.H. AND R.H. SIDES, $\Sigma_N = 2 \times 5 = 10$, $\Sigma_S = (2 \times 2) + 1 = 5$, $\Sigma_{S'} = (2 \times 7) + 2 = 16$ $\therefore \Sigma = -1$

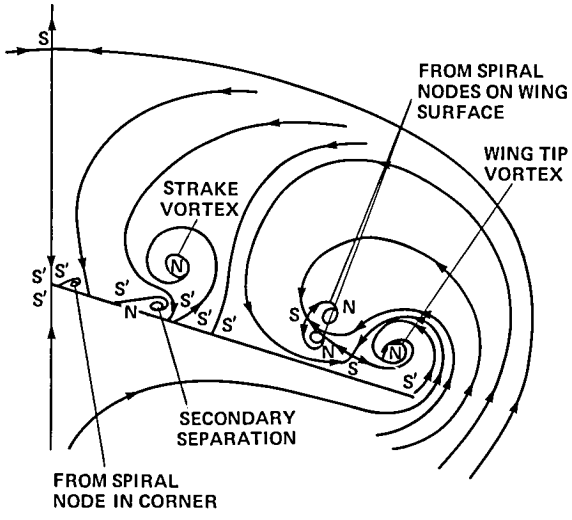

(d) Conjectured external streamlines in plane close to wing trailing edge (starboard side only).

Fig. 14. Concluded.

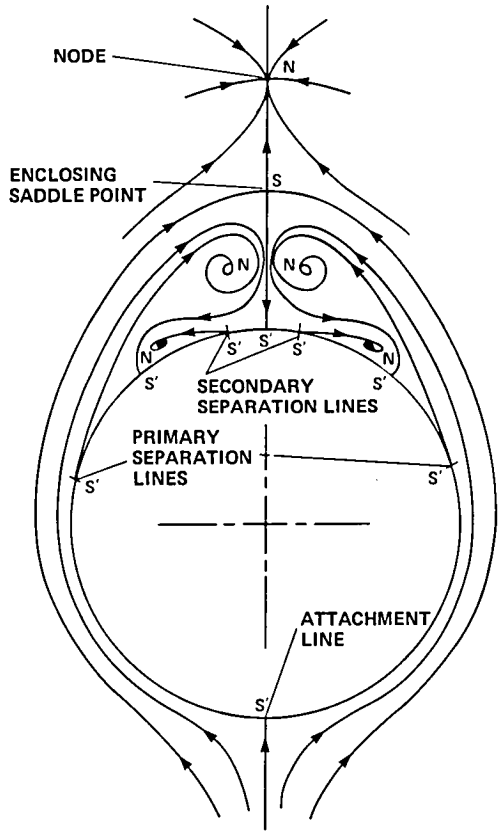

TOPOLOGY LAW FOR CONICAL FLOW PROJECTION IS:

$\Sigma_N - (\Sigma_S + \frac{1}{2}\Sigma_{S'}) = 0$. HERE, $\Sigma_N = 5$, $\Sigma_S = 1$, $\Sigma_{S'} = 8$; $\therefore \Sigma = 0$

Fig. 15. Flat projection of three-dimensional stream surfaces intersecting sphere centered on cone vertex with both primary and secondary separation. There are five nodes and spiral nodes (Σ_N), one saddle, and eight half-saddles.

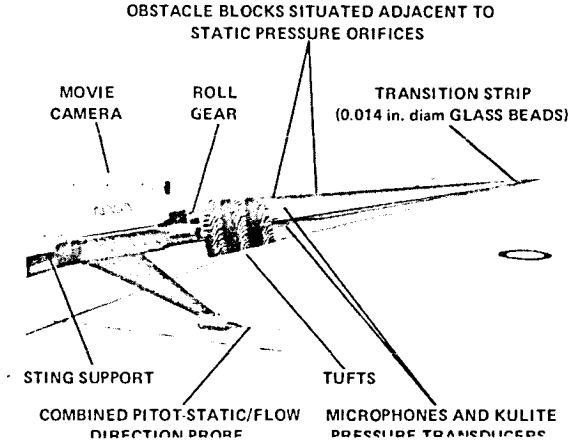

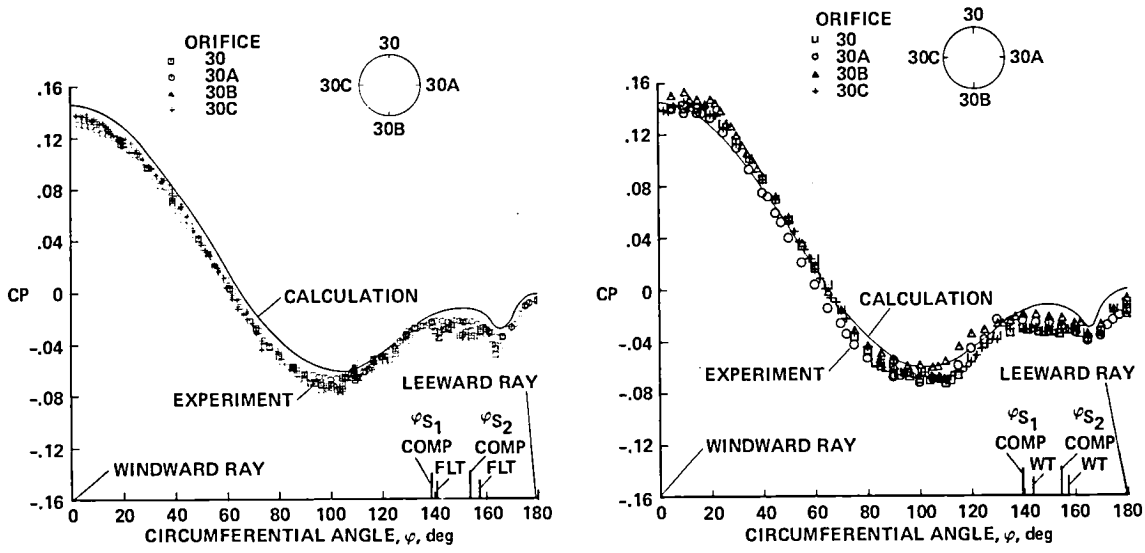

(a) Flight results.

(b) Wind-tunnel results.

Fig. 17. Five-degree semiapex angle cone flight and wind-tunnel results for Mach 1.8. Circumferential mean pressure distributions at one axial station, x = 30 in., α = 11°.

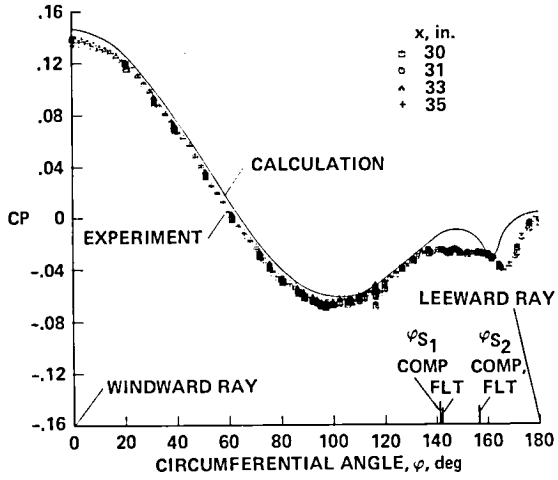

Fig. 18. Five-degree semiapex angle cone flight results at Mach 1.5. Circumferential mean pressure distributions at several axial stations, x = 30 to 35 in., α = 11°.

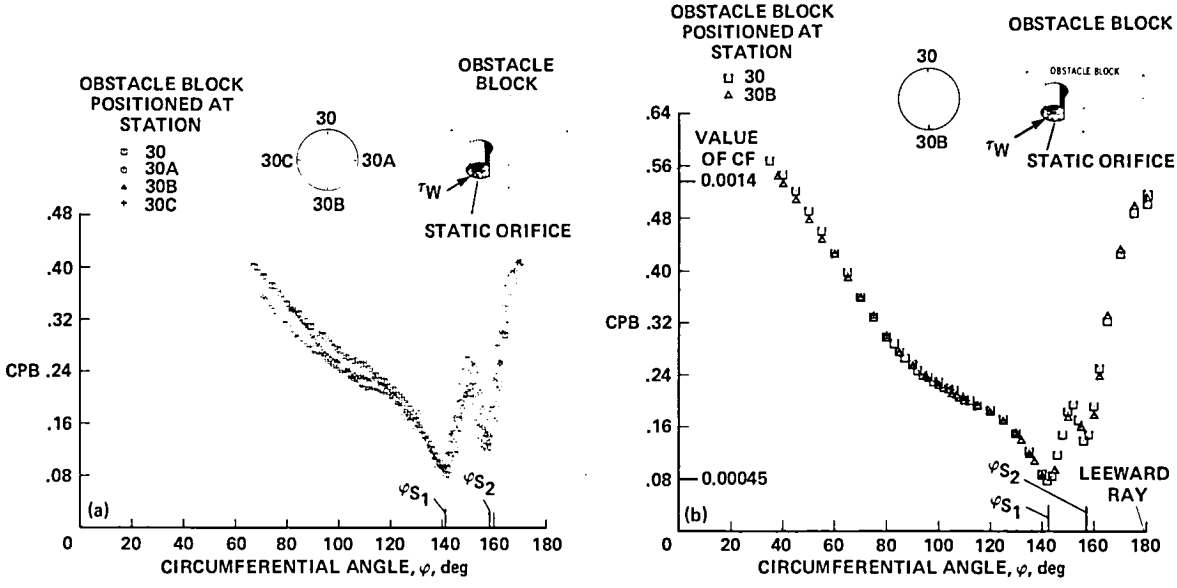

(a) Flight results

(b) Wind-tunnel results

Fig 19. Five-degree semiapex angle cone flight and wind-tunnel skin-friction results at Mach 1.8, x = 30 in., α = 11°.

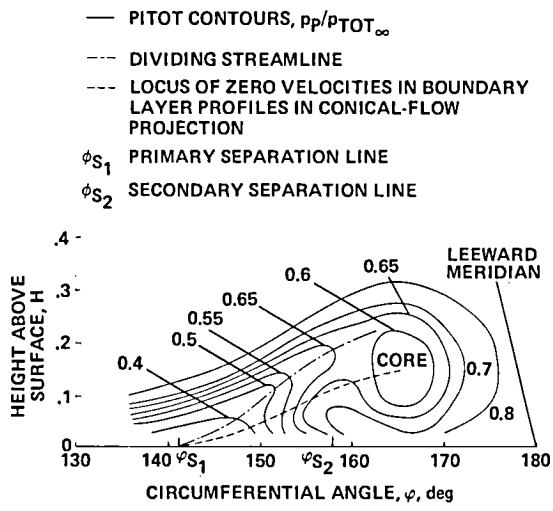

Fig. 20. Computed contours of constant pitot pressure on leeward of 5° semiapex angle cone, M_∞ = 1.8, α = 11°, R_{x_∞} = 9.8 × 10^6.

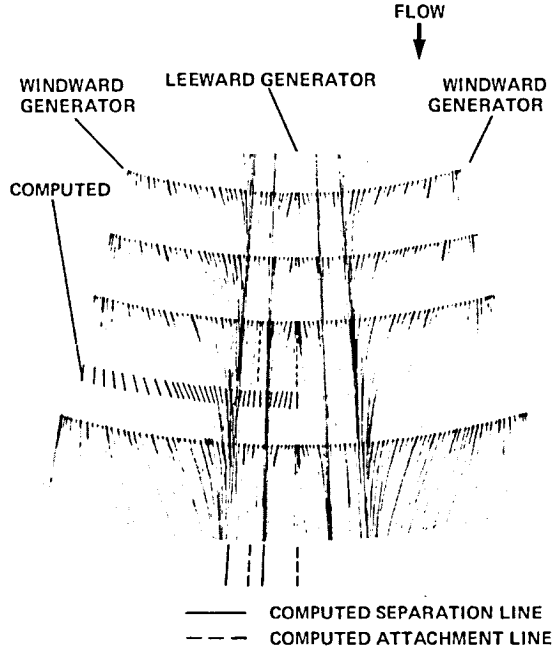

Fig. 21. Unwrapped pattern of experimental skin-friction lines on 5° semiapex angle cone, compared with computed limiting streamline directions at Mach 1.8, α = 12.5°.

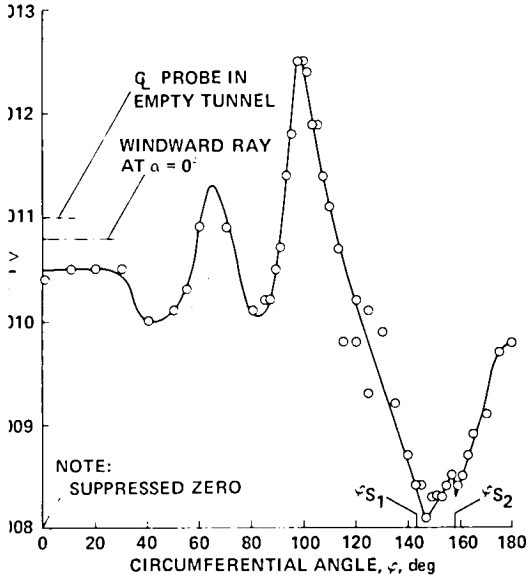

ig. 22. Wind-tunnel measurements on 5° semi-pex angle cone of root-mean-square microphone utput at one axial station, x = 34 in., α = 11°, M_∞ = 1.5, RN = 2.9 × 10^6/ft.

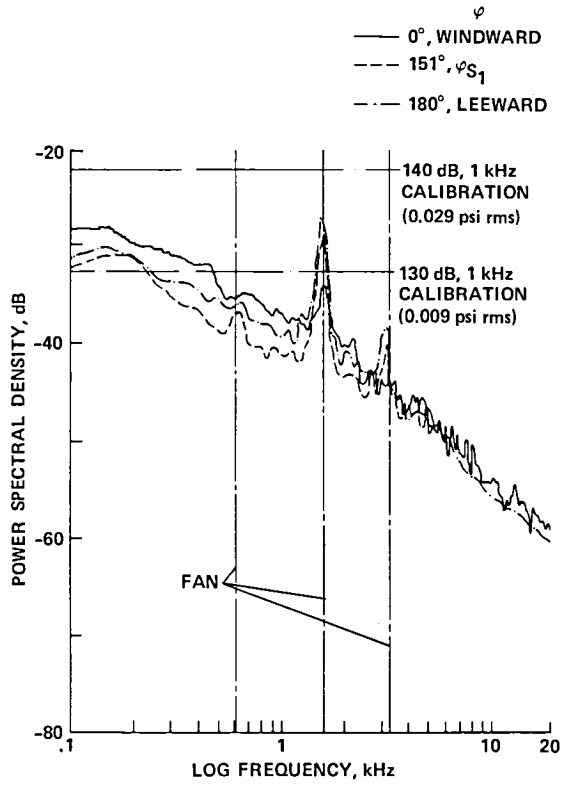

Fig. 23. Mach 1.5 wind-tunnel results of selected spectra from microphone at x = 34 in. in surface of 5° semiapex angle cone. RN = 2.9 × 10^6/ft., α = 11°.

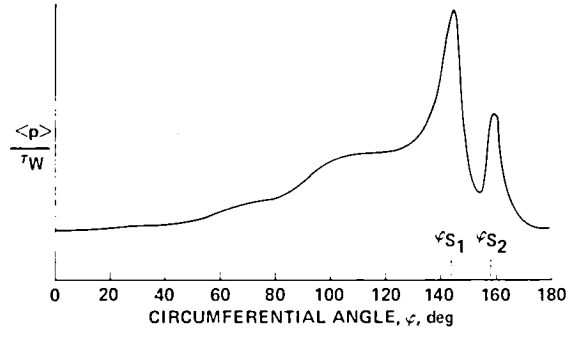

Fig. 24. Mach 1.5 wind-tunnel results of root-mean-square pressure fluctuation at x = 34 in. along surface of 5° semiapex angle cone, normalized by local wall shear-stress, α = 11°, RN = 2.9 × 10^6/ft.

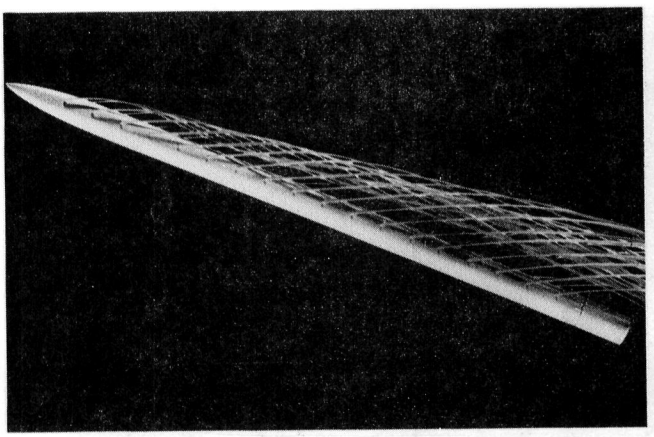

(a) $\alpha \sim 25°$, symmetric.

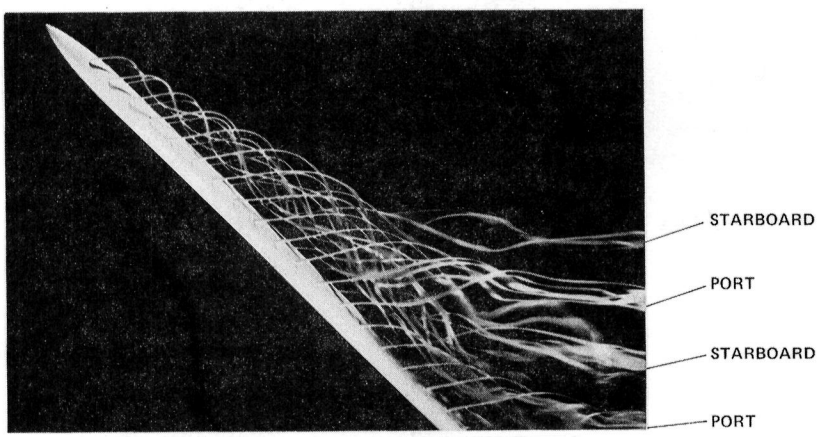

(b) $\alpha \sim 48°$, asymmetric and relatively steady.

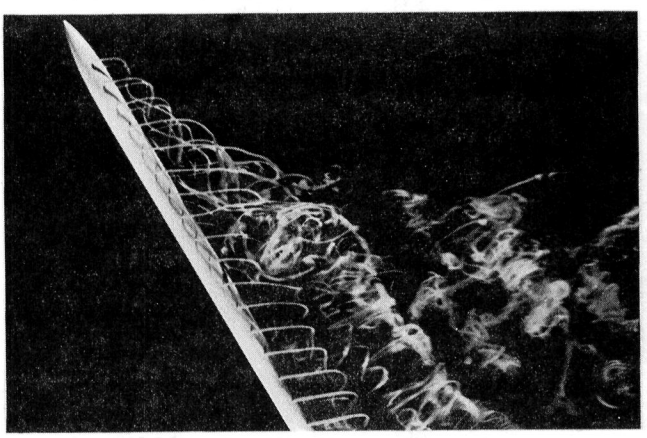

(c) $\alpha \sim 60°$, asymmetric and unsteady.

Fig. 25. Lee vortex wake about 18° semiapex angle tangent-ogive-cylinder at angle of attack in water tunnel (Fiechter, Ref. 32).

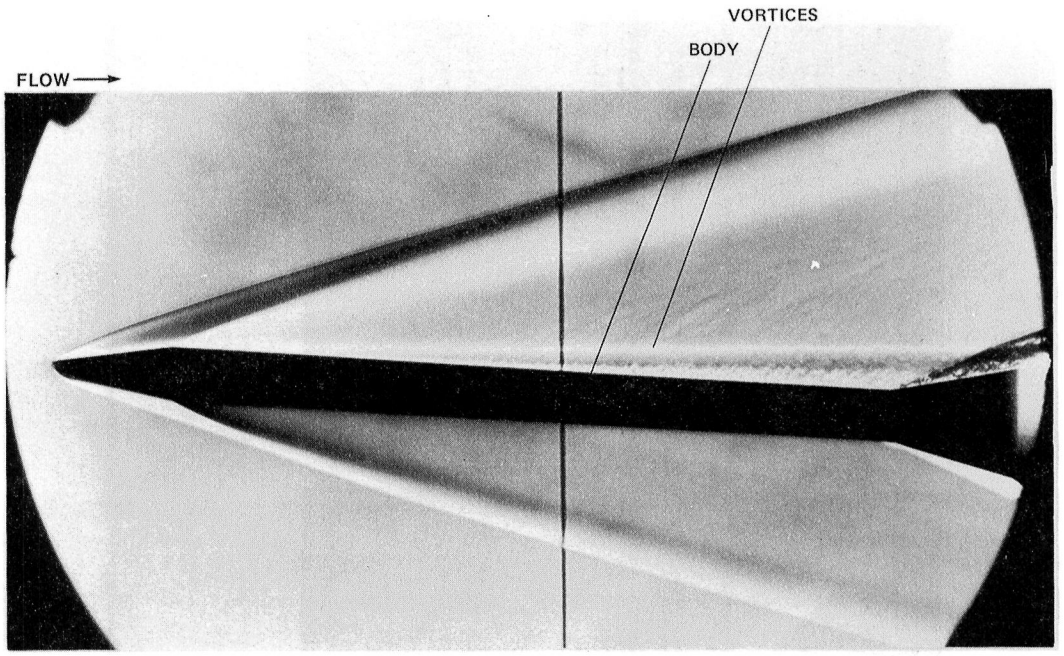

Fig. 26. Body separations on 10° semiapex angle blunted cone-cylinder-flare at $M_\infty = 4$, and $\alpha = 5°$.

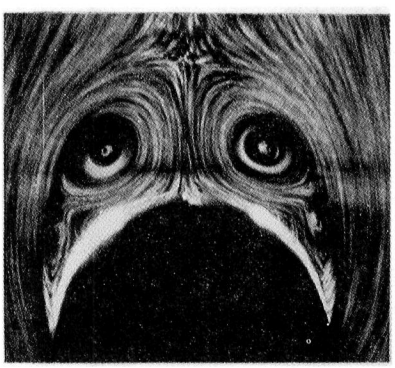

(a) Symmetric cross flow, water tunnel, $M_\infty \sim 0$, $\alpha = 20°$ (Werlé 1974).

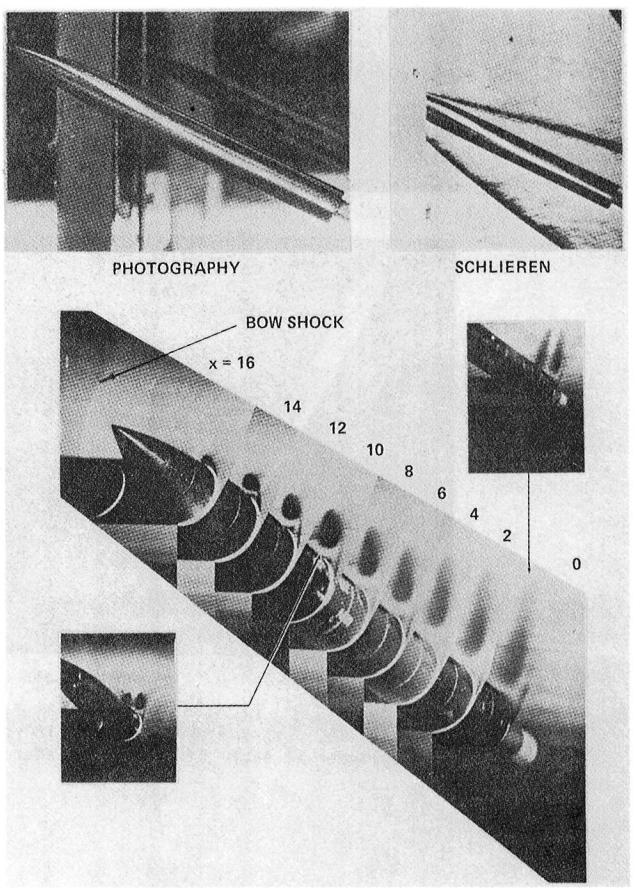

(b) Laser vapor screen, oil flow and Schlieren flow visualization, $M_\infty = 2$, $\alpha = 26°$ (O'Hare and Jones, 1973).

Fig. 27. Views of the symmetric vortex wake in the crossflow plane about tangent-ogive cylinders at angle of attack.

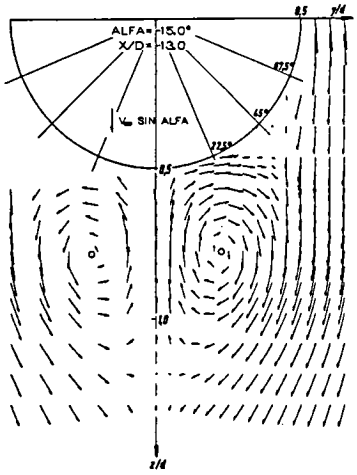

(a) Cross flow velocities

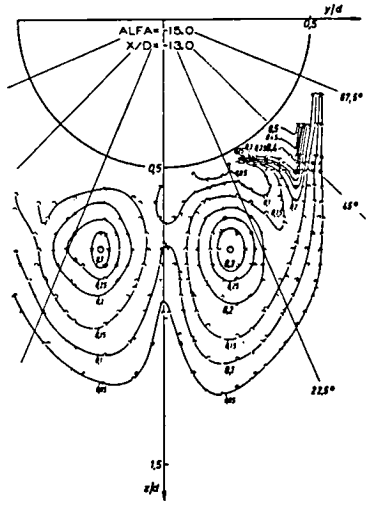

(b) Isobars of total pressure loss $(p_{t_\infty} - p_t)/q_\infty$ = const

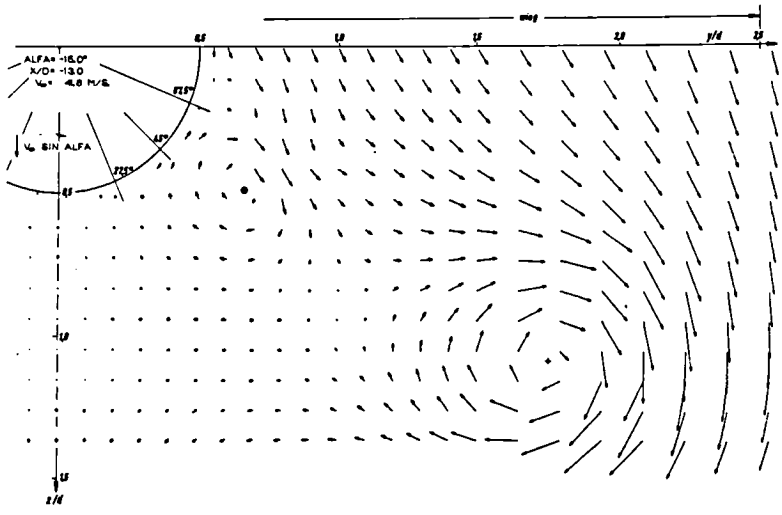

(c) Cross flow velocities at the plane X/D = 13; angle of attack α = -15°; with delta wing

Fig. 28. Body vortices about 18° semiapex angle tangent-ogive cylinder in low-speed turbulent flow at α =-15° (Grosche, Ref. 35).

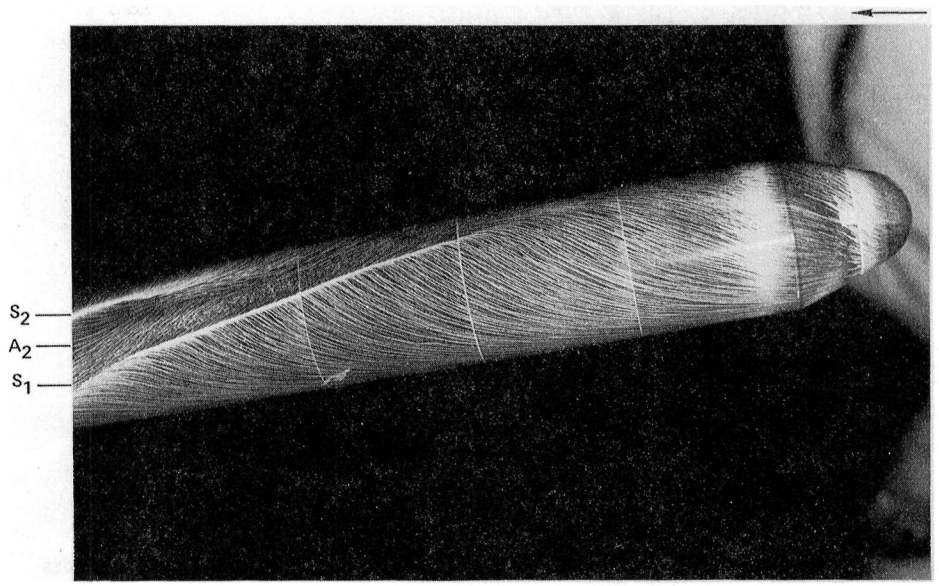

(a) Side elevation, $R_{L_\infty} \sim 10 \times 10^6$, $R_D = 1.3 \times 10^6$
length, L = 38.2 cm (15 in); D = 5.0 cm (1.97 in.).

(b) Unwrapped surface of clindrical afterbody,
$R_{L_\infty} \sim 10 \times 10^6$, $R_D = 1.3 \times 10^6$.

Fig. 29. Surface oil-flow patterns on 20° semiapex angle blunted cone-cylinder at $\alpha = 12°$, $M_\infty = 2.4$, with turbulent boundary layers (Boersen, Ref. 36).

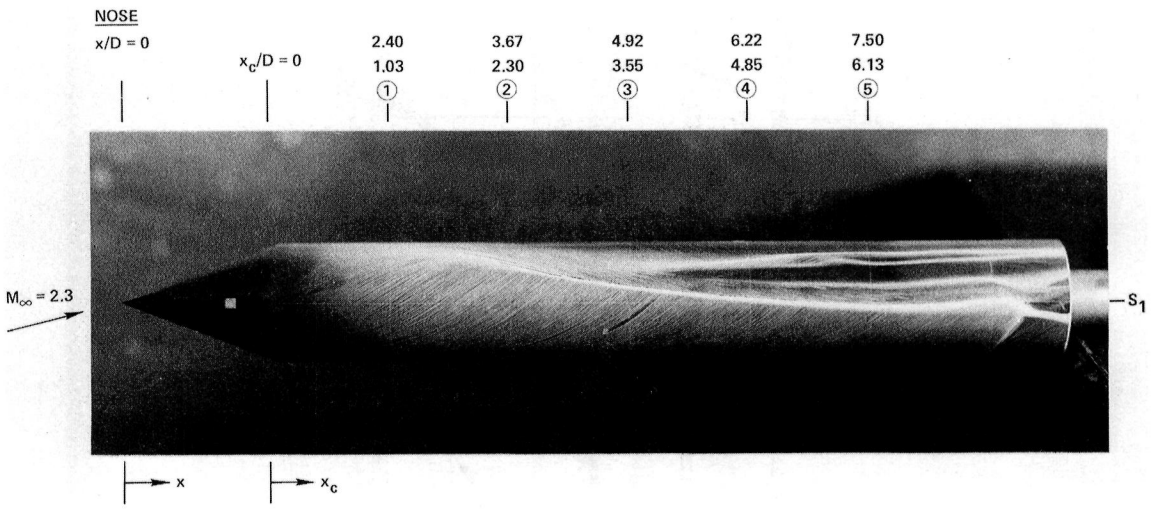

(a) Side elevation, $R_{L_\infty} \sim 32 \times 10^6$ ($R_D = 4 \times 10^6$)
length, L = 40 cm (15.75 in.); D = 5.0 cm (1.97 in.)

Fig. 30. Surface oil-flow patterns and circumferential pressures on 20° semiapex angle pointed cone-cylinder at α = 12°, M_∞ = 2.3, with turbulent boundary layers (Boersen, Ref. 36).

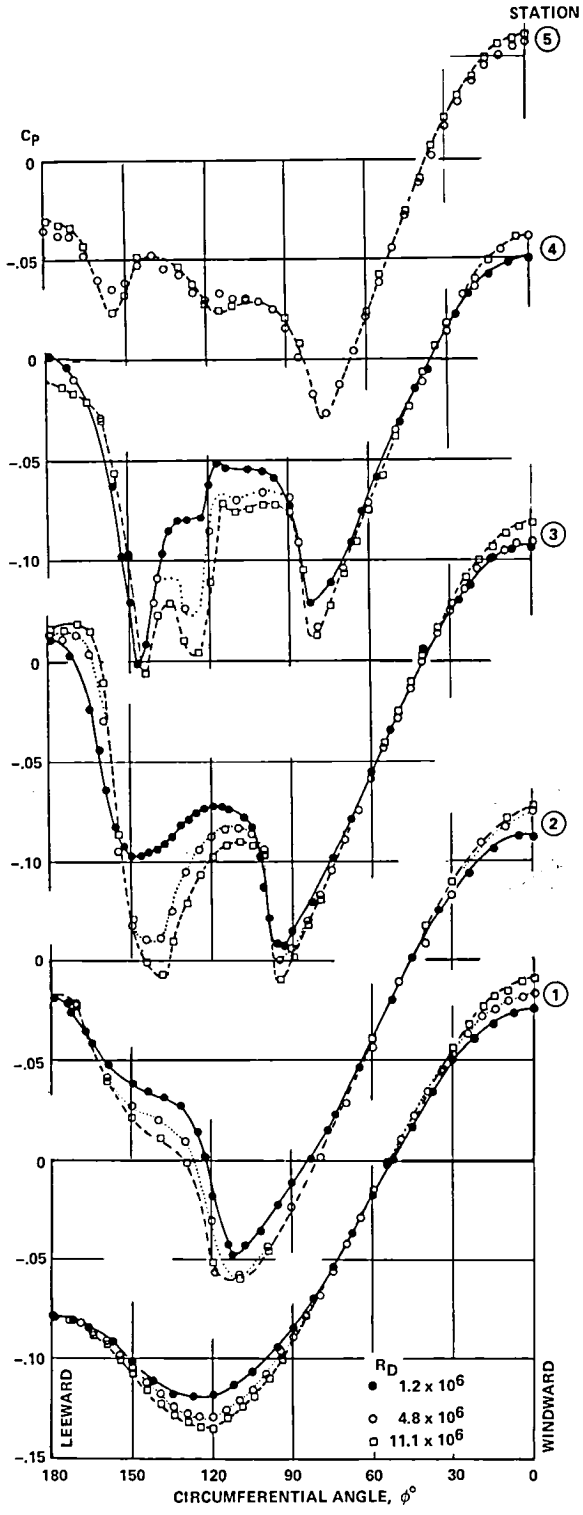

(b) Circumferential pressure distributions on afterbody of cone-cylinder

Fig. 30. Continued.

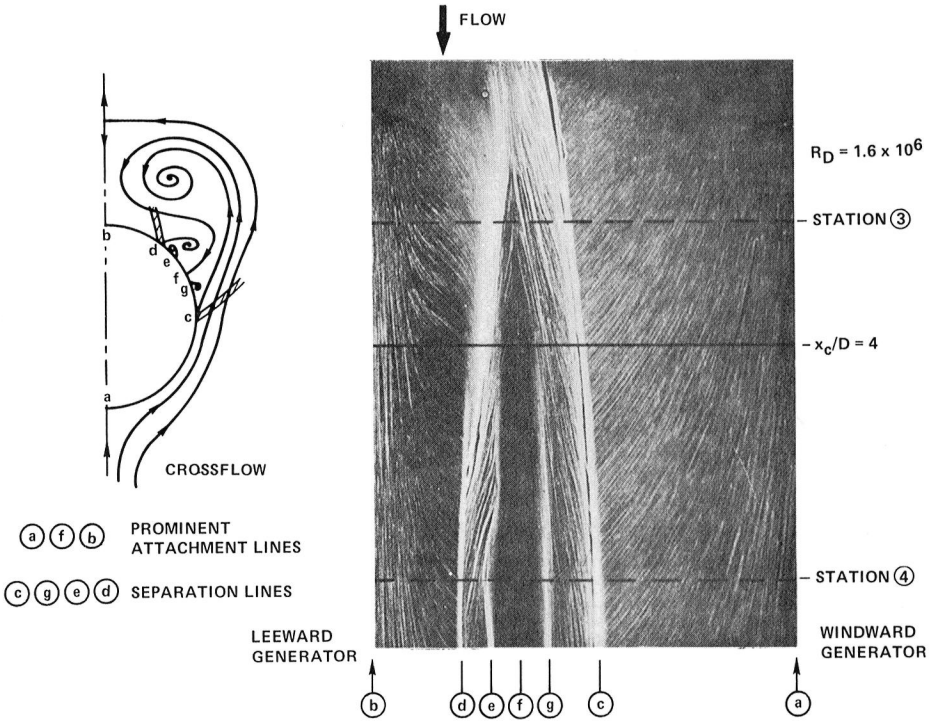

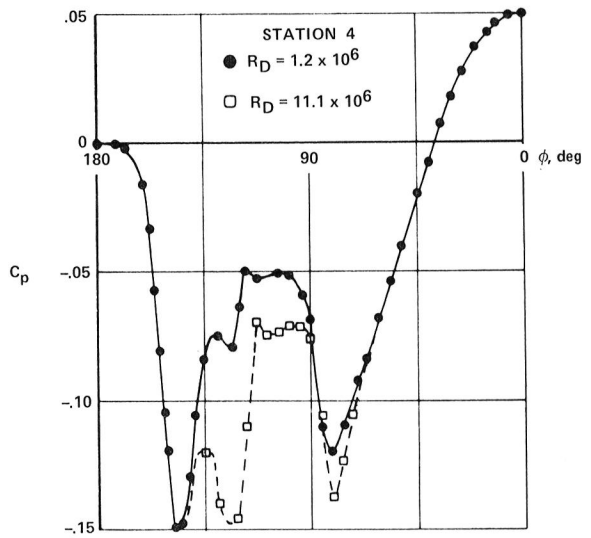

(c) Oil flow and surface pressures on downstream part of afterbody

Fig. 30. Concluded.

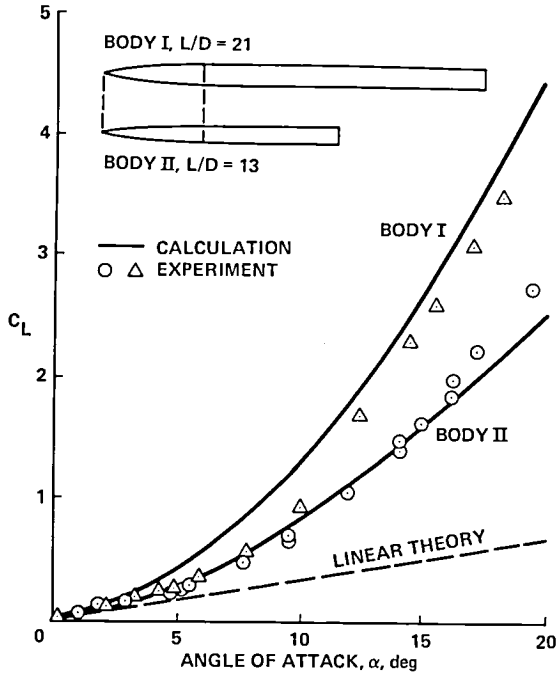

Fig. 31. Overall lift of two bodies of revolution (see Küchemann, Ref. 41).

CONFIGURATION	SEMI-APEX ANGLE θ_c	NOSE LENGTH $\frac{L_N}{D}$	AFTERBODY LENGTH $\frac{L-L_N}{D}$	m
C5 - 12D	5° 43′	5	12	1
O7 - 12D	7° 36′	5	12	4/3
O9 - 12D	9° 28′	5	12	5/3
O11 - 12D	11° 19′	5	12	2
C9 - 12D	9° 28′	3	12	1
O12 - 12D	12° 31′	3	12	4/3
O15 - 12D	15° 31′	3	12	5/3
O18 - 12D	18° 26′	3	12	2
C5 - 6D	5° 43′	5	6	1
O7 - 6D	7° 36′	5	6	4/3
O9 - 6D	9° 28′	5	6	5/3
O11 - 6D	11° 19′	5	6	2
C9 - 6D	9° 28′	3	6	1
O12 - 6D	12° 31′	3	6	4/3
O15 - 6D	15° 31′	3	6	5/3
O18 - 6D	18° 26′	3	6	2

C = CONE, O = OGIVE

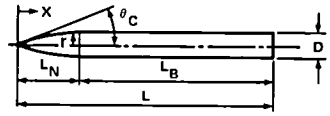

NOSE CONTOUR: $\frac{r}{D} = \frac{1}{2}\left[1-(1-\frac{X}{L_N})^m\right]$

Fig. 32. Details of long, pointed slender bodies tested at NAE, Canada (Peake et al., Ref. 42).

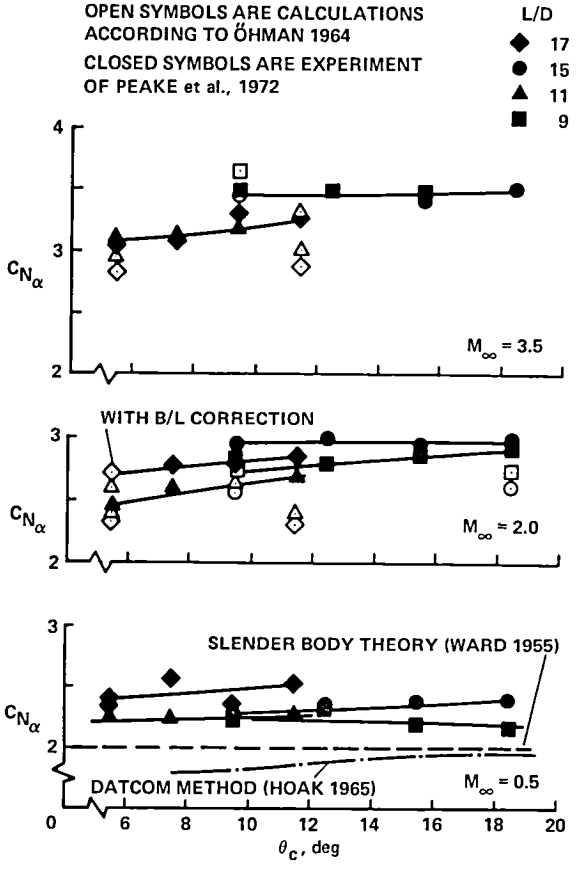

Fig. 33. Low angle-of-attack performance of long, pointed slender bodies in terms of normal force slope versus semi-nose angle at M_∞ = 0.5, 2.0, and 3.5, at $R_D = 1 \times 10^6$ to 4×10^6 (Peake et al., Ref. 42).

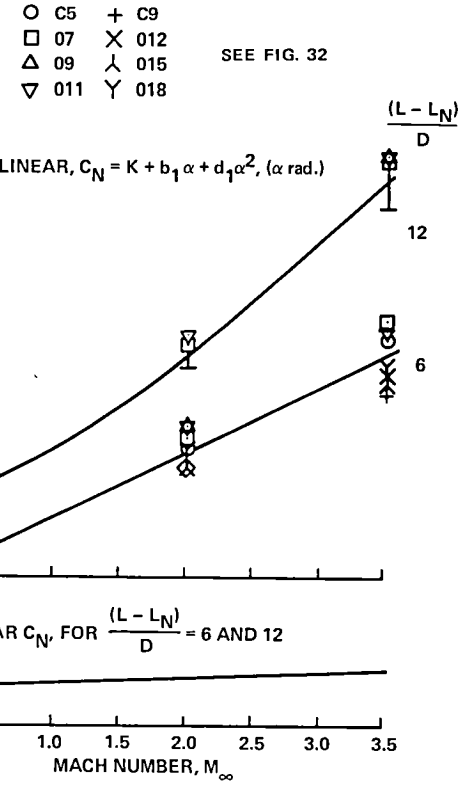

Fig. 34. Linear and nonlinear lift on long, pointed slender bodies at $R_D = 1 \times 10^6$ to 4×10^6 (Peake et al., Ref. 42).

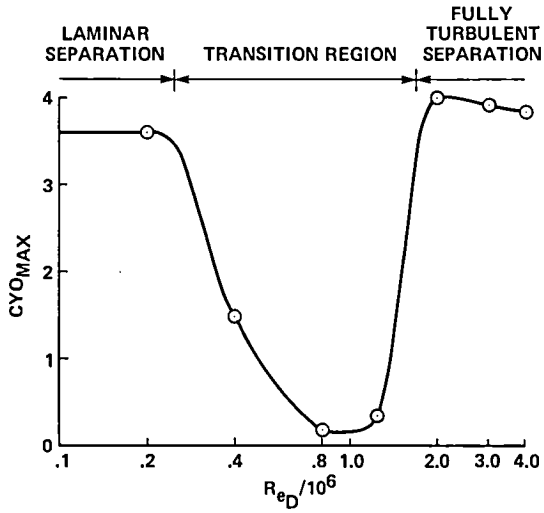

Fig. 35. Effect of Reynolds number on maximum side force at α = 55° on ogive/cylinder (2D/13D in length), M_∞ = 0.3 (Lamont, Ref. 48).

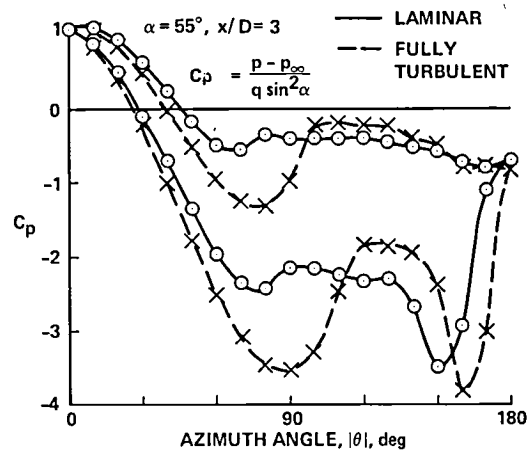

Fig. 36. Typical asymmetric pressure distributions for laminar and turbulent flow at α = 55° on ogive/cylinder (2D/13D in length, M_∞ = 0.3 (Lamont, Ref. 48).

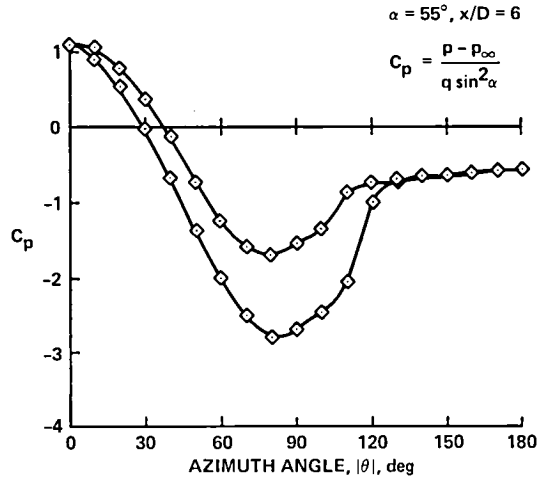

Fig. 37. Asymmetric pressure distributions in transitional flow at α = 55° on ogive/cylinder (2D/13D in length), M_∞ = 0.3 (Lamont, Ref. 48).

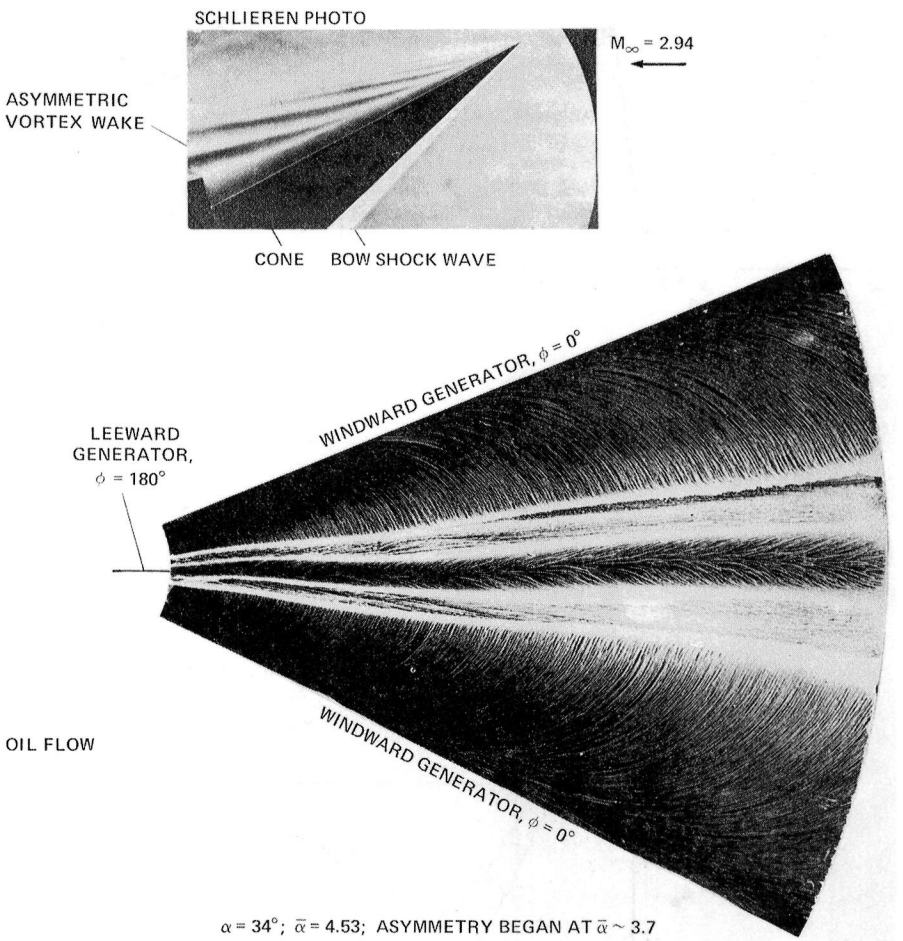

Fig. 38. Asymmetric oil-flow pattern on unwrapped surface, and Schlieren photograph of a 7.5° semiapex angle cone at $M_\infty = 2.94$, turbulent, $R_{L_\infty} = 7 \times 10^6$ (Bannink and Nebbeling, Ref. 51).

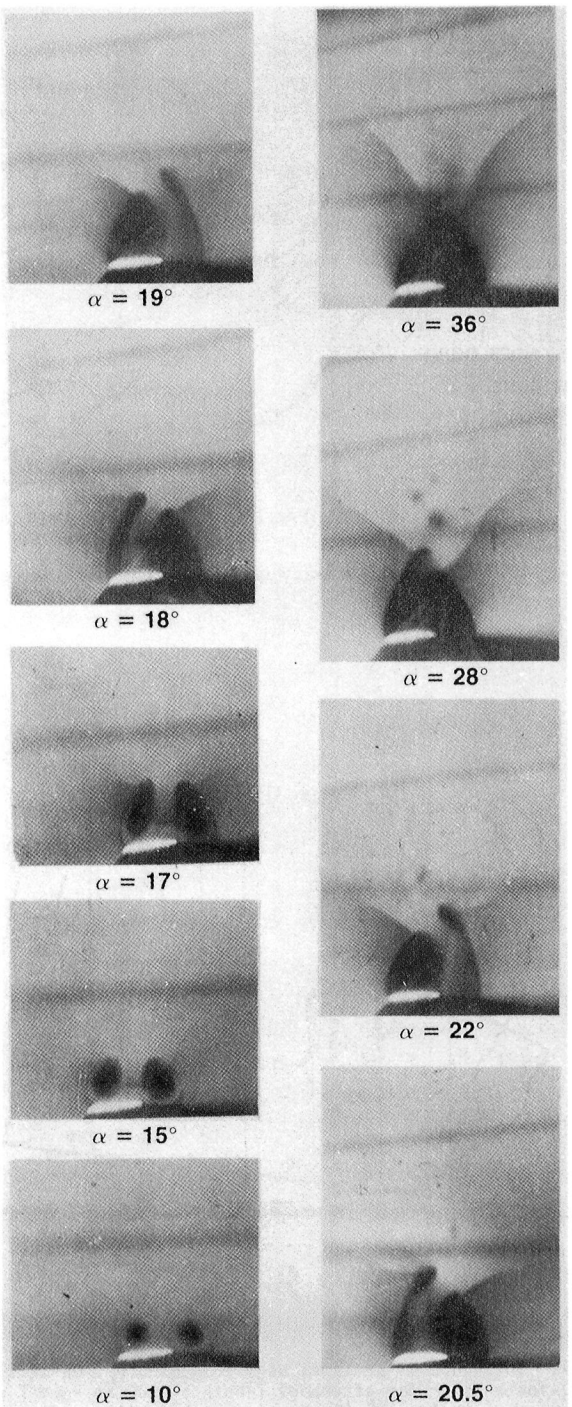

Fig. 39. Asymmetric flow over slender delta wing at angle of attack at M_∞ = 2.8 (Fellows and Carter, Ref. 54).

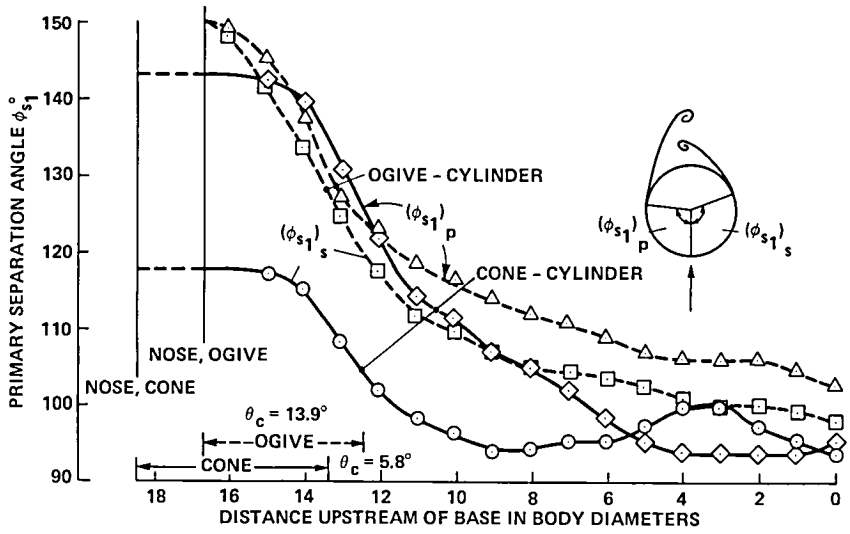

Fig. 40. Asymmetric primary separation on cone and ogive-cylinders, α = 18°, M_∞ = 0.6, R_{L_∞} = 3.5 × 10^7 (Rainbird et al., Ref. 50).

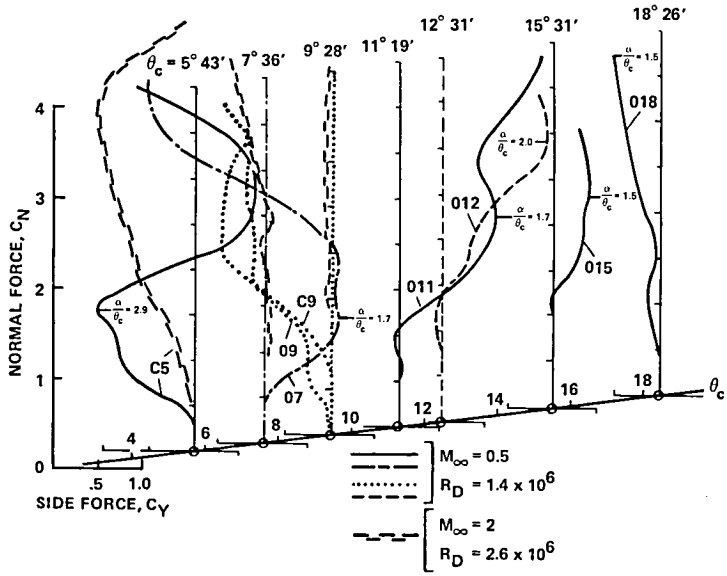

Fig. 41. Influence of semiapex angle of nose, θ_c, on side-force/normal-force polar for afterbody length of 12D at R_D = 1 × 10^6 to 4 × 10^6 (Peake et al., Ref. 42).

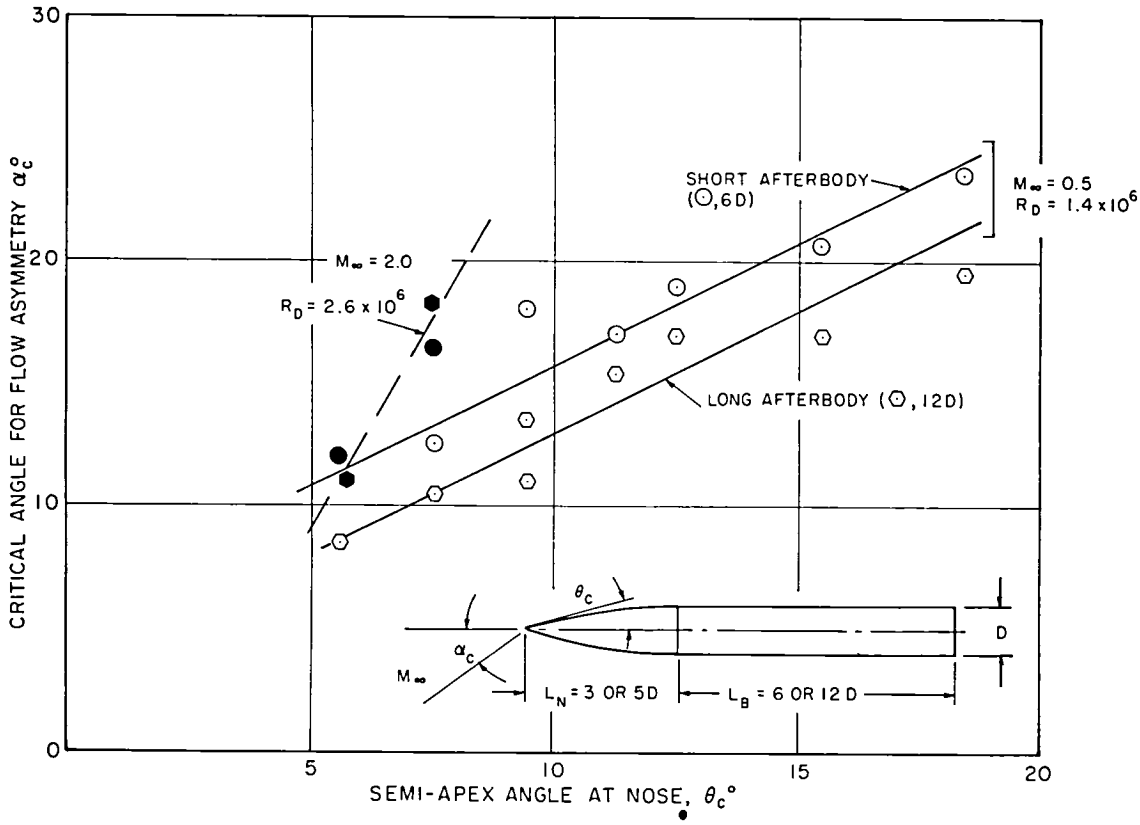

Fig. 42. Critical angle of attack for onset of flow asymmetry (Peake et al., Ref. 42).

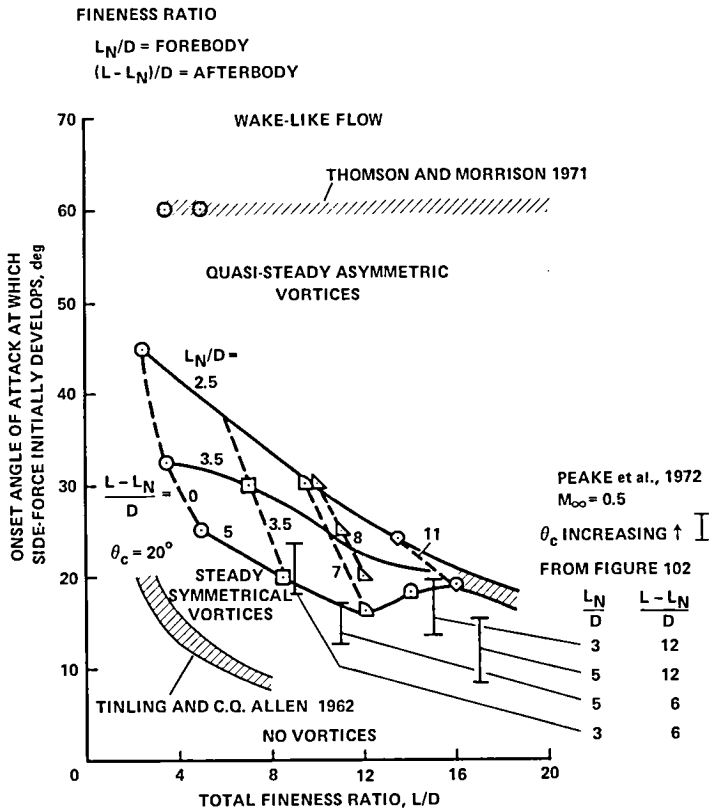

Fig. 43. Boundaries for various types of leeward flow separation about tangent-ogive/cylinders at M_∞ = 0.6 (Keener et al., Ref. 56; Tinling and Allen, Ref. 62; Thomson and Morrison, Ref. 63).

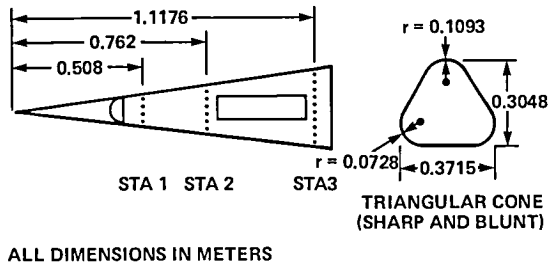

Fig. 44. Blunt and sharp-nose triangular cone models.

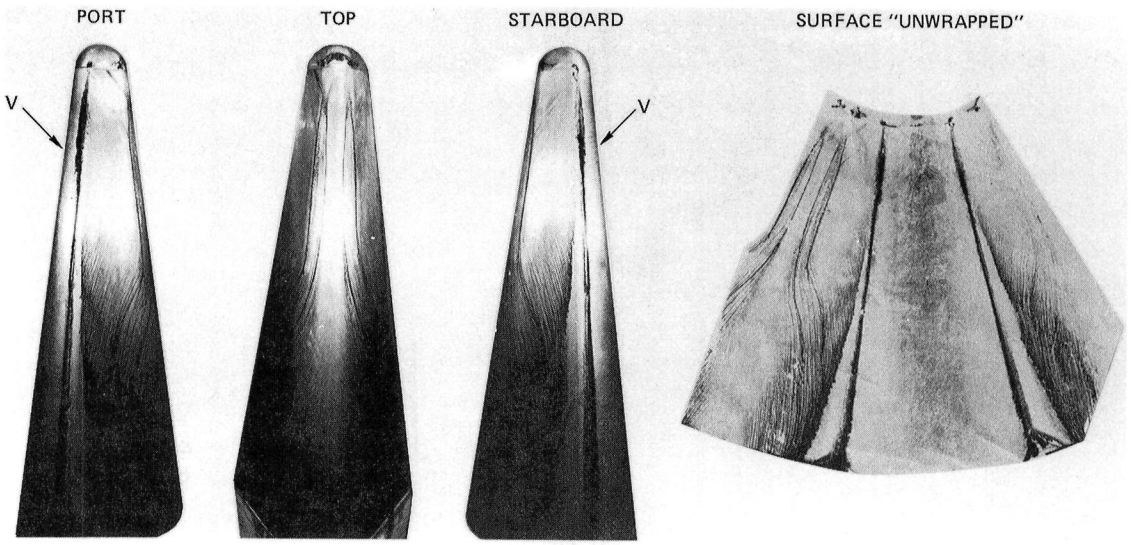

(a) Blunt-nose cone, $\sigma = 45°$, $Re_h = 1.1 \times 10^6$.

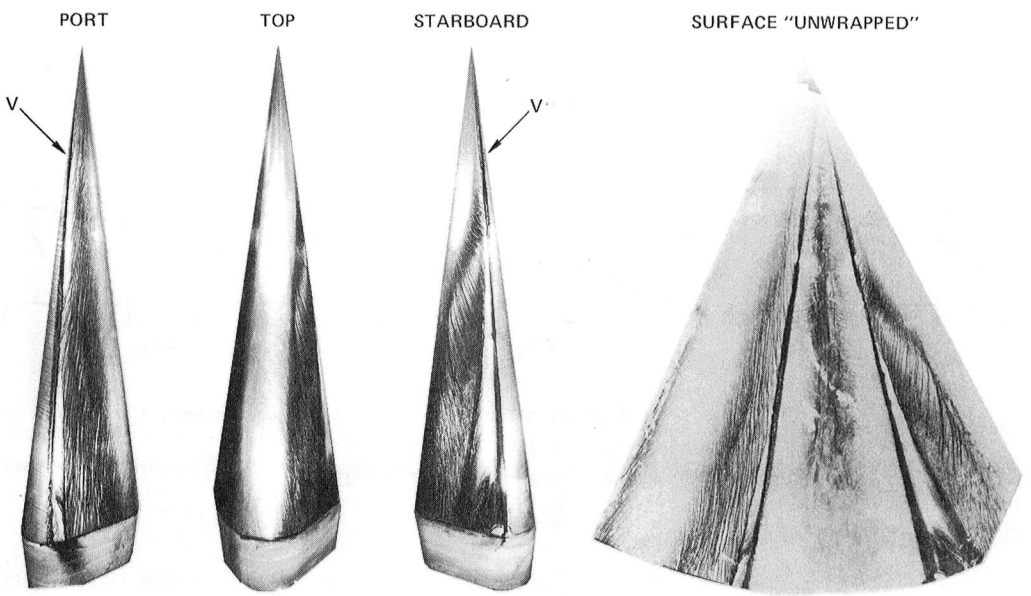

(b) Sharp-nose cone, $\sigma = 45°$, $Re_h = 1.2 \times 10^6$.

Fig. 45. Surface oil-flow patterns on blunt and sharp-nose triangular cones.

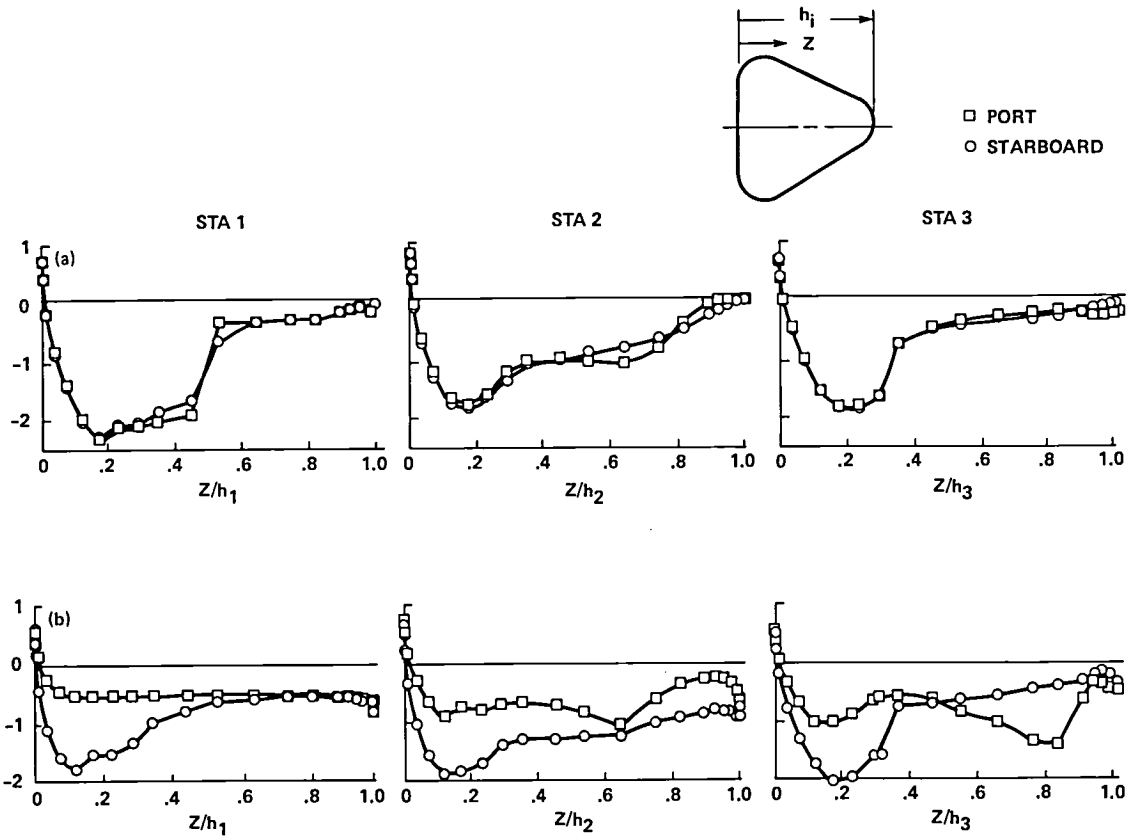

Fig. 46. Pressure distributions on blunt and sharp-nose triangular cones.
(a) Blunt-nose cone, $\sigma = 45°$, $R_{e_h} = 1.1 \times 10^6$.
(b) Sharp-nose cone, $\sigma = 45°$, $R_{e_h} = 1.2 \times 10^6$.

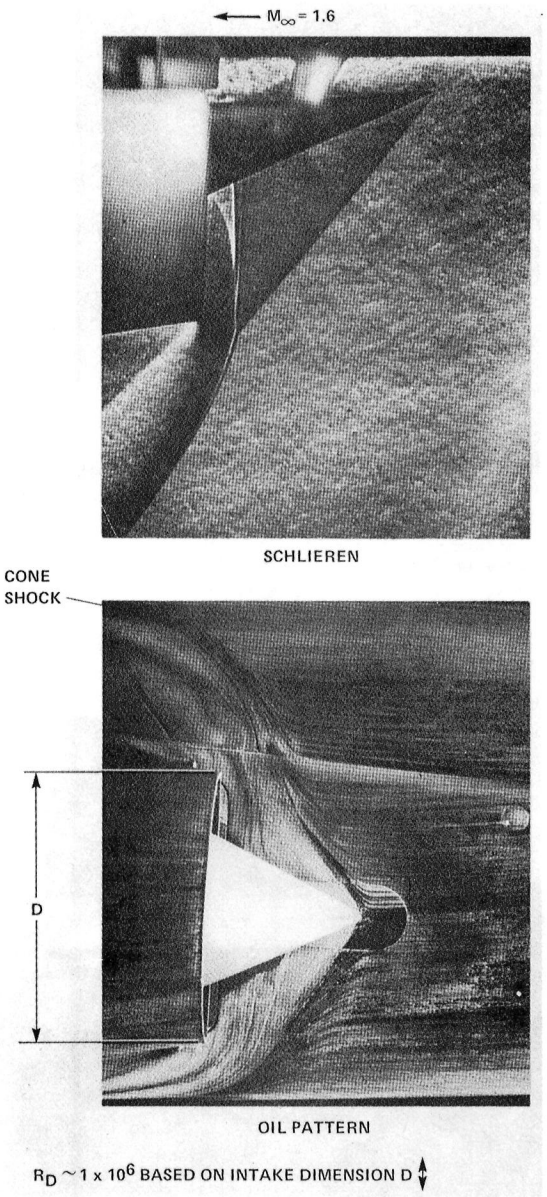

Fig. 47. Oil-flow pattern due to swept-shock-induced 3-D separation about half cone intake $M_\infty = 1.6$ (Culley, Refs. 67, 68).

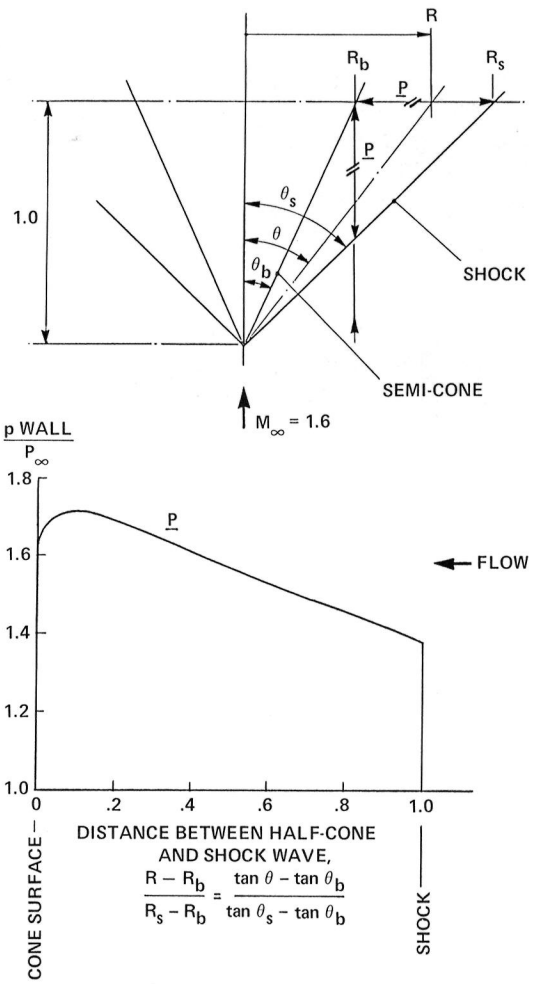

Fig. 48. Calculated pressure field between shock wave and Fourier half-cone at $M_\infty = 1.6$ (Peake, et al., Ref. 69).

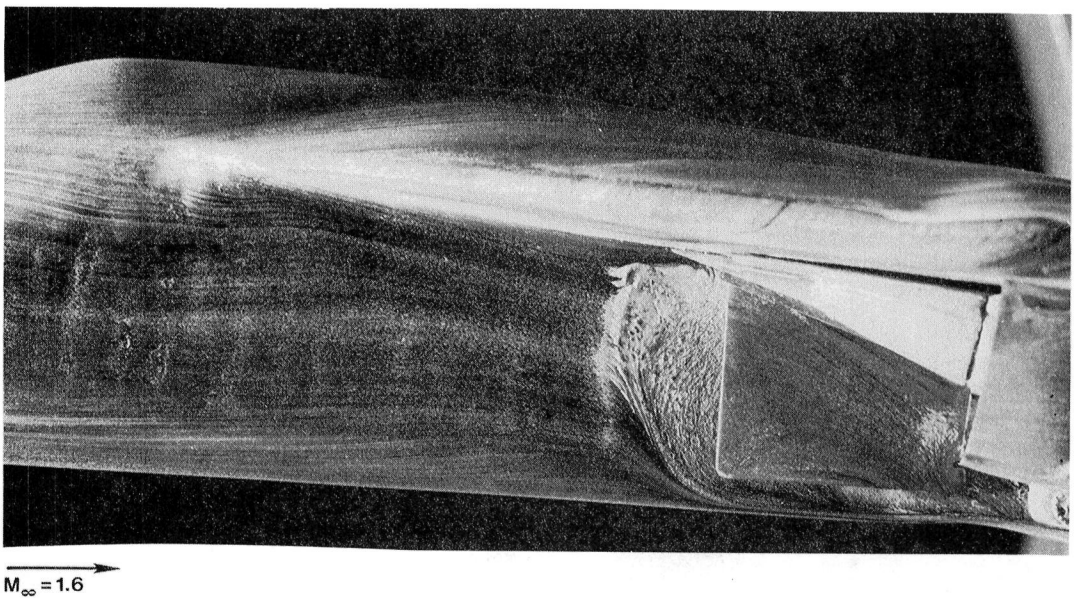

Fig. 49. Side view of 3-D separation of fuselage boundary layer induced by boundary-layer splitter-plate quarter-cone inlet; model angle of attack = 4.5°, M_∞ = 1.6 (Culley, Refs. 68, 70).

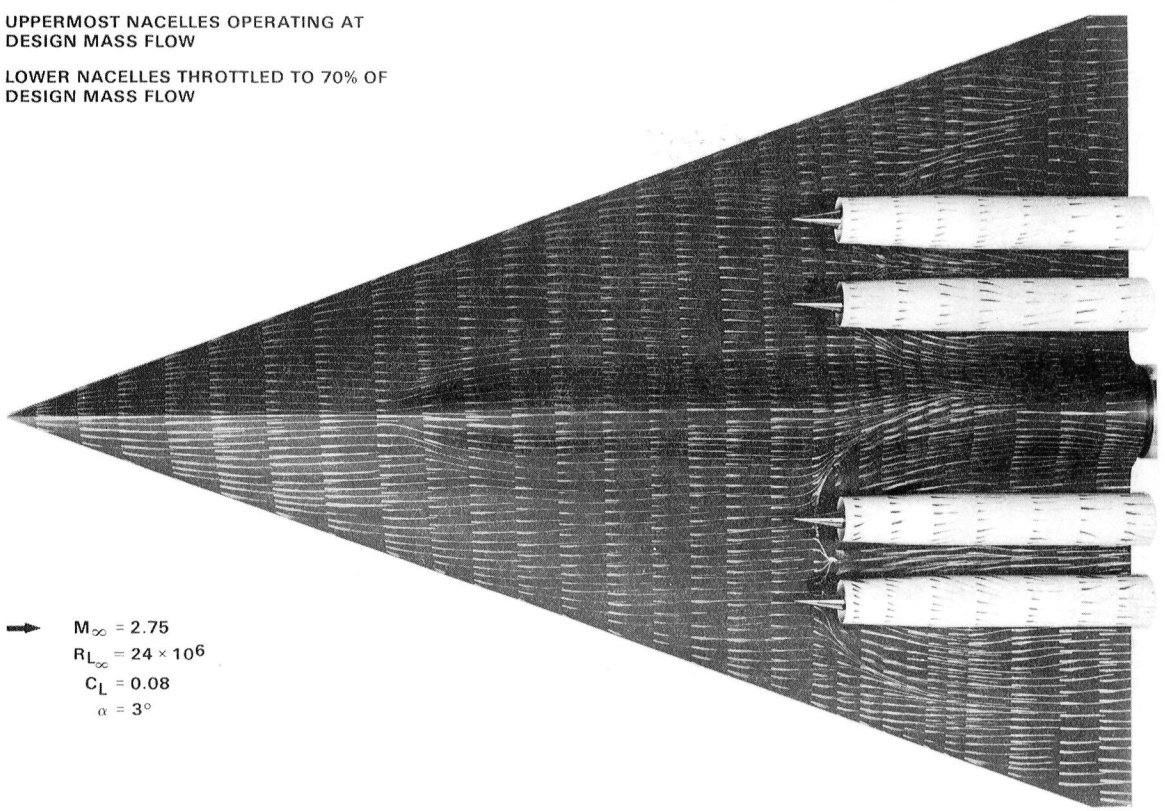

(a) Nacelles on.

Fig. 50. Oil-dot flow visualization on lower surface of 70° delta wing showing swept-back turbulent boundary-layer interactions associated with propulsion nacelles (Peake and Rainbird, Ref. 73).

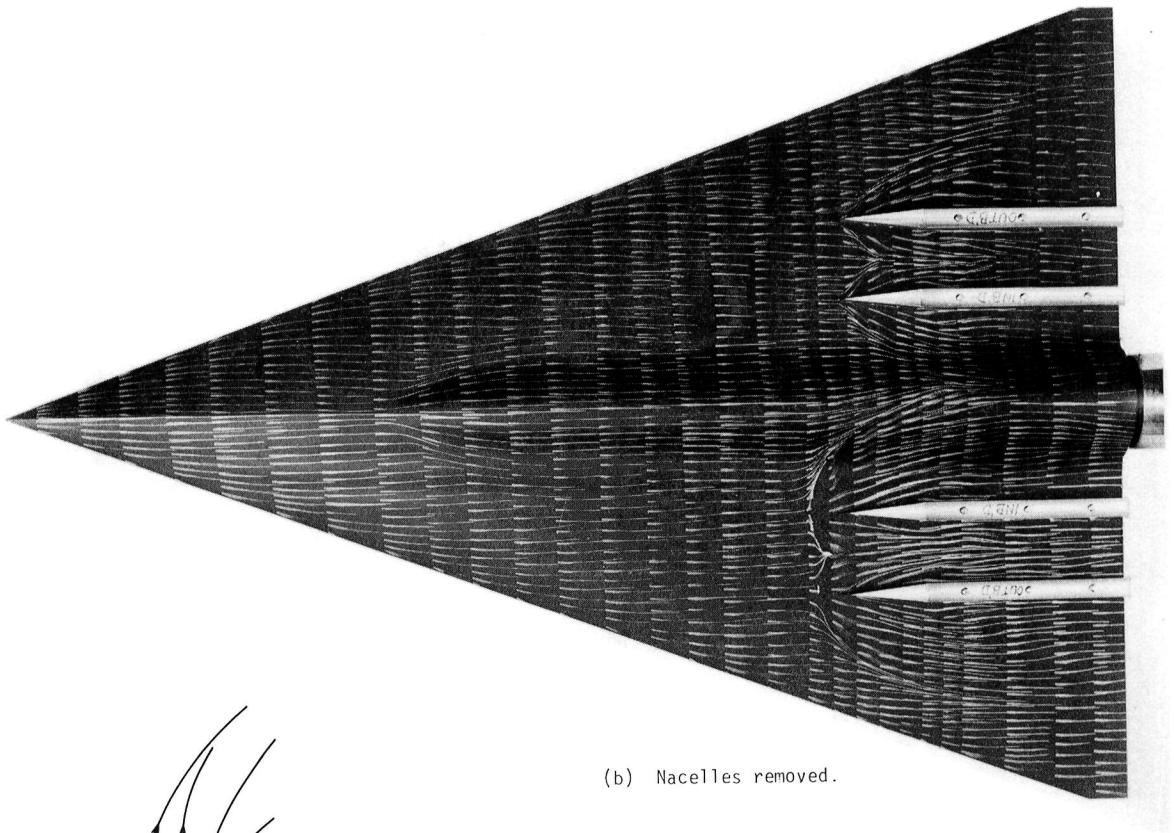

(b) Nacelles removed.

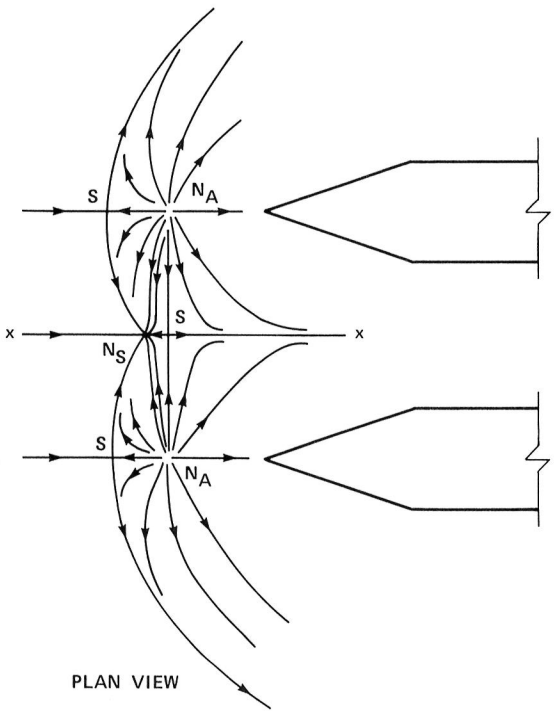

N_A = NODAL POINT OF REATTACHMENT
N_S = NODAL POINT OF SEPARATION
S = SADDLE POINT OF SEPARATION

Fig. 50. Concluded.

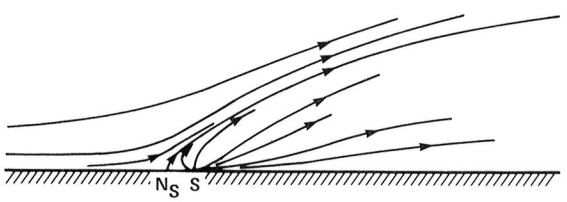

SECTION ALONG x-x

(c) Postulated patterns of skin-friction lines and external flow streamlines.

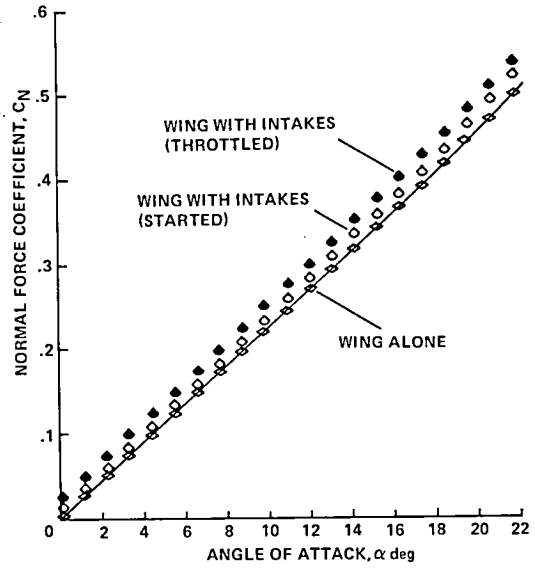

Fig. 51. "Favorable interference" effect on lift of 70° delta wing at $M_\infty = 2.75$, $R_{L_\infty} = 24 \times 10^6$ (Peake and Rainbird (Ref. 73).

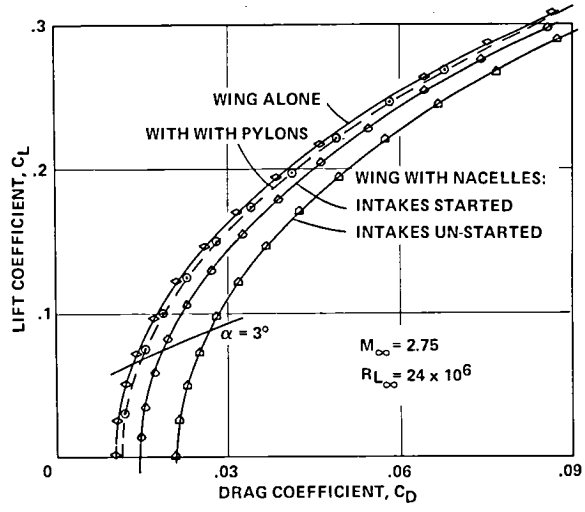

Fig. 52. Lift-drag polars: 70° delta wing with four nacelles supported on pylons at design Mach number, $M_\infty = 2.75$ (Peake and Rainbird, Ref. 73).

1. Report No.	2. Government Accession No.	3. Recipient's Catalog No.
NASA TM-84226		

4. Title and Subtitle	5. Report Date
THREE-DIMENSIONAL FLOWS ABOUT SIMPLE COMPONENTS AT ANGLE OF ATTACK	April 1982
	6. Performing Organization Code
7. Author(s)	8. Performing Organization Report No.
David J. Peake and Murray Tobak	A-8859
	10. Work Unit No.
9. Performing Organization Name and Address	T-4033Y
NASA Ames Research Center Moffett Field, Calif. 94035	11. Contract or Grant No.
	13. Type of Report and Period Covered
12. Sponsoring Agency Name and Address	Technical Memorandum
National Aeronautics and Space Administration Washington, D.C. 20546	14. Sponsoring Agency Code 505-31-21

15. Supplementary Notes
Presented as Paper No. 2 at AGARD Lecture Series No. 121 on High Angle-of-Attack Aerodynamics held at: NASA Langley Research Center, Hampton, Virginia 3/10-11/82; von Karman Institute for Fluid Dynamics, Brussels, Belgium 3/15-19/82; and DFVLR Gottingen, Gottingen, Germany 3/22-23/82.

Point of Contact: Murray Tobak, Ames Research Center, 234-1, Moffett Field, CA 94035, (415)965-5398/FTS 448-5398

16. Abstract

The structures of three-dimensional separated flows about some chosen aerodynamic components at angle of attack are synthesized, holding strictly to the notion that streamlines in the external flow (viscous plus inviscid) and skin-friction lines on the body surface may be considered as trajectories having properties consistent with those of continuous vector fields. Singular points in the fields are of limited number and are classified as simple nodes and saddles. Analogous flow structures at high angles of attack about blunt and pointed bodies, straight and swept wings, etc,, are discussed, highlighting the formation of spiral nodes (foci) in the pattern of skin-friction lines. How local and global three-dimensional separation lines originate and form is addressed, and the characteristics of both symmetric and asymmetric leeward wakes are described.

17. Key Words (Suggested by Author(s))	18. Distribution Statement
Three-dimensional flow separation Vortices Aircraft and missiles Aerodynamic components	Unlimited Subject Category - 02

19. Security Classif. (of this report)	20. Security Classif. (of this page)	21. No. of Pages	22. Price*
Unclassified	Unclassified	59	A03

*For sale by the National Technical Information Service, Springfield, Virginia 22161